Preface

The year 2003 has passed very quickly, so it is time again to present to you the new Annual Report of the Walter Schottky Institut. As usual, the extended abstracts about ongoing scientific work have been written by PhD students and members of the Scientific Staff and are grouped in the four sections Basic Semiconductor Physics, Materials Science and Technology, Biochemical Applications, and Devices. At the end of the report, we have compiled relevant information for the year 2003 concerning funding, publications, teaching, and the people who make the Walter Schottky Institut a very pleasant and stimulating place to do research. Please also have a look at the series "Selected Topics of Semiconductor Physics and Technology", which by now contains 60 PhD theses published since the start of this book series in 1997. Do not hesitate to contact us if you are interested in a particular volume or two.

Actually, the present Annual Report 2003 is the 10th in the series of reports started in 1994. Therefore, I would like to use this opportunity for a brief glimpse at the development which the Walter Schottky Institut has enjoyed during the last decade. On the input side, the large number of national and international research projects which have been successfully acquired by the senior members of the research staff has allowed us to maintain a high level of

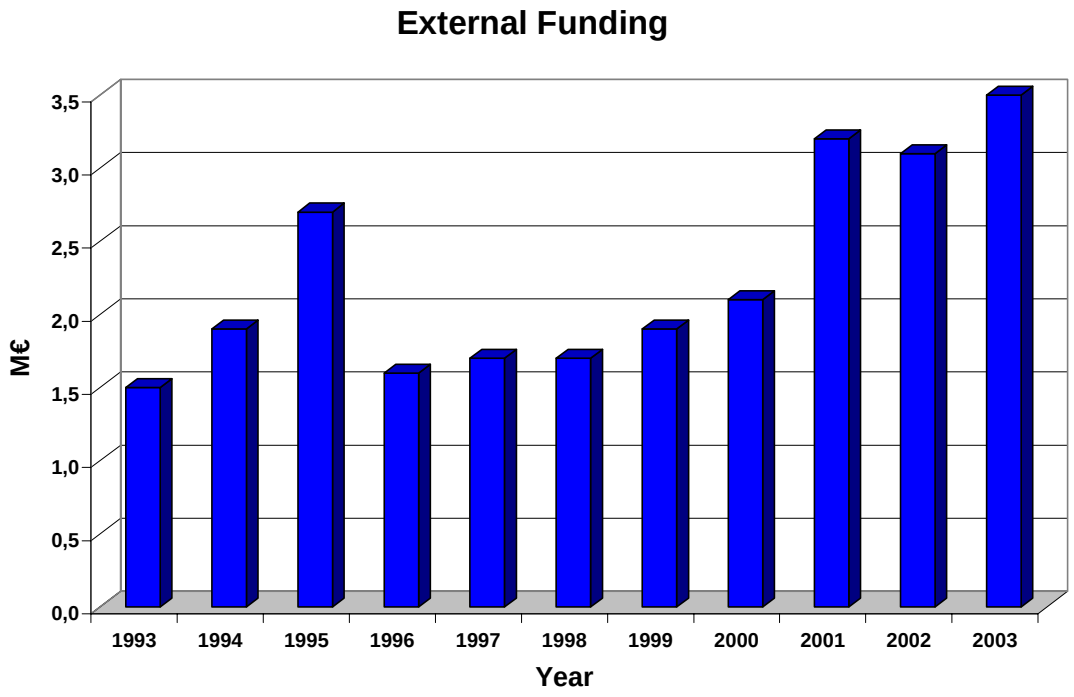

scientific activity in a very cost-intensive environment. As can be seen from the above diagram, the amount of external funding for the Walter Schottky Institute has increased by about a factor of two in the last decade, from about € 1.5 Mill. to more than € 3 Mill. per year recently. A considerable part of this external support comes from the participation of the Institute in various Collaborative Research Centers ("Sonderforschungsbereiche") funded by the Deutsche Forschungsgemeinschaft:

- SFB 348 ("Nanometer Semiconductor Devices"), which was concluded at the end of 2003 after more than a decade of very successful research,

- SFB 563 ("Bioorganic Functional Systems on Solids"), which currently supports most of the research activities of the Institute related to the area of bioelectronics, and
- SFB 631 ("Solid State based Quantum Information Processing"), which started in 2003 and allows us to perform fundamental research in an exciting new area of basic semiconductor physics.

Also on the input side are about 30 young physicists each year who decide to do their diploma or doctorate studies in our Institute. Their enthusiasm and spontaneity ensure that life at the Institute never gets boring. Among other things, these students are attracted by the dedicated teaching activities of the senior Institute members, which quite regularly have been recognized by excellence in teaching awards. Our students also profit from a large number of external guests, who give the all important international contacts real names and faces. In 2003, we were particularly pleased that Prof. M. Shur (Rensselaer Polytechnic Institute, New York) came and shared his scientific experience with us as a Senior Humboldt Fellow.

On the output side of an Institute like ours are mainly scientific papers and qualified scientists. As is evident from the figure below, the average "scientific production" of the Walter Schottky Institute has been about 100 articles per year (or two articles per week) for the last ten years. Of course, the number of articles published per year alone is no guarantee for scientific quality, even if most of these articles were published in journals with the highest international reputation. A closer look at the citation statistics of articles coming from our Institute, however, is similarly positive. According to the Web of Science, each article published by scientists of the Walter Schottky Institute in the last ten years has been cited on the average more than 13 times. This is far above the average citation rate per article in solid state physics and shows that the research money given to the Institute by external sources indeed has been very well invested.

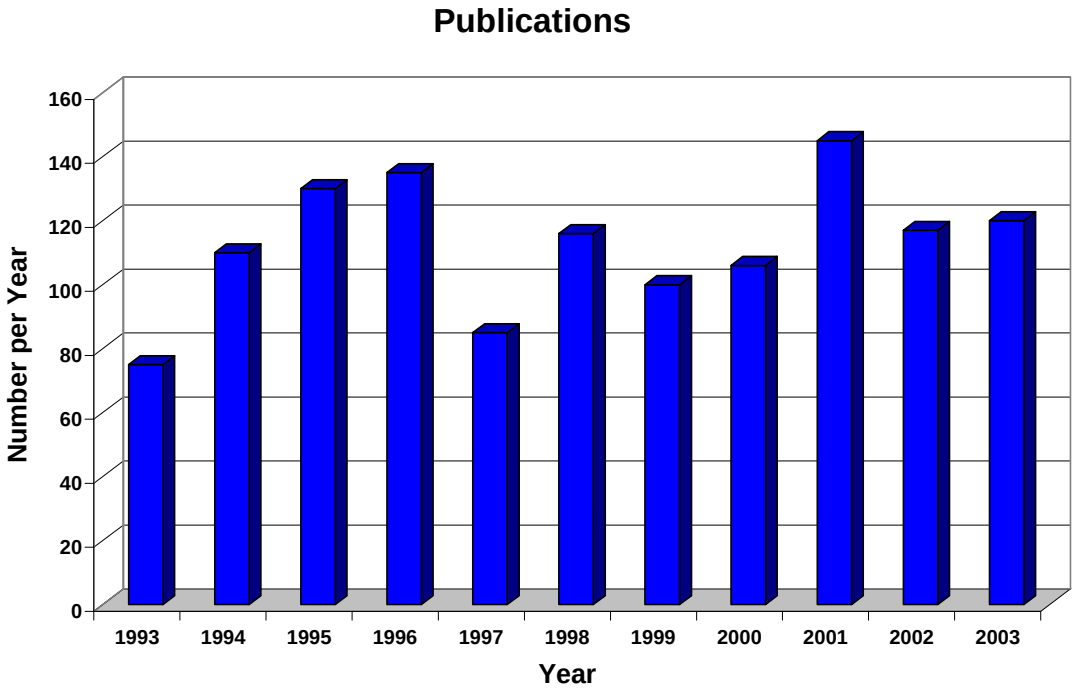

Equally positive is the increasing number of our alumni, who have worked at the Walter Schottky Institut to obtain their Diploma or PhD, or as a Postdoc. Since 1994, 220 Diploma theses and 110 PhD theses were completed successfully, and you can have a closer look at the PhDs of 2003 on the next pages. The large majority of our PhD candidates already performed

their diploma work at the Walter Schottky Institut and then decided to stay. All of our alumni have found good jobs in Bavaria and the rest of the world. To be more precise, about 40% of the PhD students went on to take a position at Infineon or Siemens. Another 40% found similar jobs in other high tech companies (BMW, Bosch, Epcos, Heidenhain, Osram, Texas Instruments, Uniphase, Wacker, etc). Approximately 10% remained in academia or took positions in public research institutes, and another 10% more or less left physics and now work as consultants, patent lawyers, or in software companies. In addition, among the non-permanent members of our research staff, since 1997 seven have completed their Habilitation, and five were offered a position as full professor at other universities.

Many of our alumni regularly join us once a year for our traditional Sommerfest at the end of July, or support the Walter Schottky Institut as members of our “Förderverein”. It is my pleasure to thank all of them for staying in contact and for their help! Those who want to join us in the future are cordially invited, too!

Finally, I would like to thank all colleagues, coworkers, and partners for their support and help during the last year. I am looking forward to hopefully many more years of successful research and cooperations!

Garching, April 2004 Martin Stutzmann

PhD's of 2003

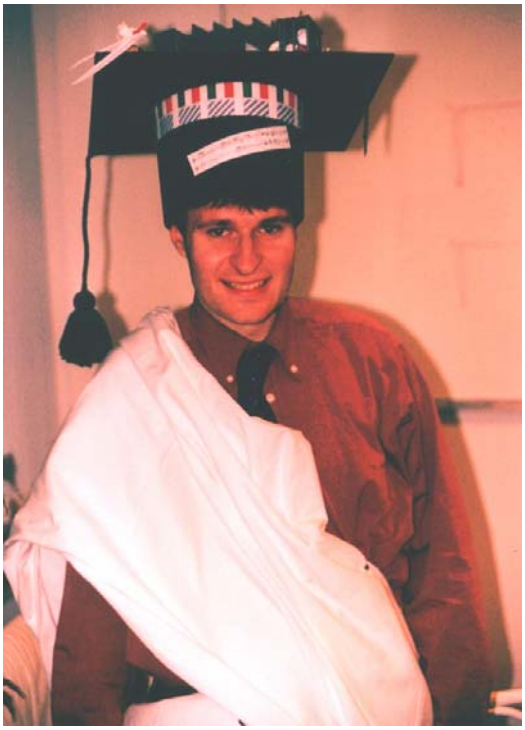

Giuseppe Scarpa

Doris Heinrich

Nicolaus Ulbrich

Sebastian Gönnenwein

Andreas Janotta

Evelin Beham

Tobias Graf

Stefan Klein

Ralph Neuberger

1. The Walter Schottky Institut

History

The Walter Schottky Institut (WSI) is a Central Institute of the Technical University of Munich (TUM). It was founded in order to strengthen the interaction between basic physics and semiconductor electronics research and development. After the decision was made to create such an interdisciplinary research institute in early 1986 it took about two years until the new laboratories became operational in May 1988. This exceptionally short time for planning and construction of a modern institute building was made possible by the excellent cooperation between the Siemens AG, the Bavarian ministries and the TUM.

Resources

The WSI building contains laboratories and offices with a total area of about 2400 m². It is well equipped with state-of-the-art facilities for semiconductor preparation, characterization, and device technology. The main resources are listed in the following:

Materials preparation and semiconductor technology
Epitaxy systems for GaAs, InP, GaSb, GaN/AlGaN, and SiGe based heterostructures (MBE, CBE, plasma-induced MBE)
Ultrahigh purity GaAs MBE machine (electron mobilities > 10 Mio cm2/Vs)
UHV evaporation equipment for SiGe on glass
Plasma-enhanced Si-CVD
Pulsed laser processing
Laboratory for surface modification / biofunctionalization
250 m^2 class 100 clean room facility with photolithography, e-beam lithography, reactive ion etching, metallization

Characterization and spectroscopy tools
High resolution X-ray diffraction
Atomic force microscopy
Electron microscopy and EDX equipment
Photoluminescence and Raman spectroscopy (from IR to UV)
DLTS, Optical DLTS, CV-profiling
Hall measurements and magneto-transport
FTIR spectroscopy
X-ray photoelectron spectroscopy
High frequency parameter analyzers
Electron spin resonance (ODMR, EDMR)
He^3 cryostats with magnetic fields up to 15 and 17 Tesla
Special characterization facility for laser diodes

Computational facilities
High end workstations

Research groups

The WSI accommodates four research groups headed by **Gerhard Abstreiter, Markus-Christian Amann**, **Martin Stutzmann,** and **Peter Vogl**, with a total headcount of about 90 including scientific and technical staff, secretaries, and doctorate as well as diploma (master) students. Out of these, about 25 permanent positions are authorized by TUM, while basically all the doctorate positions are financed via research projects with external funding. The main research interests are:

- fabrication and characterization of new semiconductor materials, material combinations, as well as hetero- and nanostructures
- basic physics with emphasis on electronic and optical properties of low dimensional systems
- realization of new semiconductor devices for application in ultrafast electronics, optoelectronics and sensors
- theory and simulation of modern semiconductor materials and devices

Experimental Semiconductor Physics I (Gerhard Abstreiter):

Research projects of this group deal with various aspects of electronic and optical properties of low-dimensional, mesoscopic semiconductor structures, the heteroepitaxy of group IV and III-V semiconductors, the development of novel methods for lateral patterning and of analytical tools for the characterization of nanometer-size structures, as well as the fabrication and test of new, unconventional electronic and optoelectronic devices. Examples for basic research are optical spectroscopy of single quantum dots, cleaved edge overgrowth on GaAs, magnetotransport in ultrahigh mobility GaAs heterostructures as well as electronic transport and tunneling in edge channels and one-dimensional systems. Device and technology oriented work aims at novel concepts for charge and spin storage in quantum dots, coherent devices based on quantum dots for future quantum information technology, and the test of semiconductor nanaostructures for chemical/biological sensors. A new area of research is the controlled manipulation of oligonucleotides on gold surface for possible protein detection and the development of SOI based lab-on-a-chip systems.

Semiconductor Technology (Markus-Christian Amann):

The research activities in this group are concentrated on modern technologies for III-V compound semiconductors and their use for developing advanced electronic and optoelectronic devices. This comprises the development of epitaxial, patterning, microstructuring, etching and coating techniques as well as the design and fabrication of semiconductor laser diodes and other photonic components. The applied material systems are GaAs-AlGaAs, InGaAsP-InP and antimonide based compounds that are grown with molecular beam epitaxy (MBE) and chemical beam epitaxy (CBE) with an accuracy in the nanometer regime. Device structuring in the 100-nm-range is obtained by using electron-beam lithography. Reactive ion etching enables the well-defined processing of the various devices with a high material selectivity of the etching rate. The group is also well equipped with evaporation and sputtering techniques for passivation and contacting of the devices. Among the key devices are single-mode and wavelength-tunable laser diodes for the wavelength range between 1300 and 2200 nm using lattice-matched and strained InGaAsP layers on InP substrates, InGaAsP and AlInGaAs vertical cavity surface-emitting laser diodes in the 1300-2000 nm wavelength range. Recent work

also covers the development of wavelength-tunable laser diodes for wavelengths above 2 µm using antimonide based compounds and quantum cascade lasers in the range of 5 to 15 µm for gas sensing. In the field of high-frequency electronic devices, the generation of rf-output power at millimeter-wave frequencies up to 300 GHz is aspired. Active transit-time diodes as well as passive varactor structures for multipliers are investigated.

Experimental Semiconductor Physics II (Martin Stutzmann):

The work of this semiconductor physics group deals with various aspects of new and nonconventional semiconductor materials and material combinations:

- semiconductors with a wide bandgap (GaN, InGaN, AlGaN, diamond, SiC),
- disordered semiconductors (amorphous, nanocrystalline, and polycrystalline),
- advanced thin film systems (silicon-based luminescent layers, thin film solar cells, organic/anorganic heterosystems, biofunctionalized semiconductors, semimagnetic semiconductors)

Most of these material systems are prepared by suitable deposition techniques (MBE, Plasma-enhanced CVD, e-beam evaporation, sputtering). Their efficient optimization is based on the large pool of structural, optical, and electrical characterization techniques available in our institute. Complementary to the usual spectroscopic techniques we have developed and employ a variety of highly sensitive methods which enable us to study in particular the influence of defects on the electronic perfomance of materials and devices. Such techniques include subgap absorption spectroscopy, optically induced capacitance spectroscopy and, in particular, modern spin resonance techniques which are applied to various materials systems and devices for spintronics.

In addition to the preparation and characterization of new semiconductor materials we also work on the modification and processing of semiconductors with pulsed high power laser systems (laser-crystallization, holographic nanostructuring, laser-induced etching) and investigate the potential of new material systems for novel device structures. Recent examples include nanostructured thin film solar cells, high electron mobility transistors based on AlGaN/GaN heterostructures, as well as UV-detectors, sensors and biosensors.

Theoretical Semiconductor Physics (Peter Vogl):

The activity of this group focuses on the theoretical study of structural, electronic and optical properties of semiconductors. The work deals with mesoscopic structures, new materials, and novel devices, in the attempt to understand their basic physics and to predict their behavior. The research conducted in the group aims at the development of theoretical tools which can support present experimental activities and propose new ideas and solutions for the future, as indicated by the strong interaction with industrial laboratories and with engineering university departments. Sophisticated quantum mechanical calculations are used for determining the electronic structures and the optical properties of a variety of semiconductor materials and systems. The information from such fundamental studies constitute the basis for the analysis of the transport properties of such materials and for the development of reliable numerical tools for device modeling. Recent activities in this group include ab-initio studies of spin devices, prediction of novel magnetic field effects, development of multiscale methods for film growth, and the design and modeling of semiconductor based quantum information devices.

The research activity of the institute thus covers a wide spectrum from basic physics in low-dimensional semiconductor structures to the development of novel or improved electronic, optoelectronic and sensor devices based on semiconductor hetero- and nanostructures. The close collaboration between the different groups and the availability of various experimental techniques are the essential basis for the successful development of novel semiconductor devices. Close contacts with industrial partners have also proven to be very fruitful and stimulating in developing new ideas and in following new directions which may be relevant for future applications.

Apart from the extensive research activities all groups are involved in teaching within their respective departments. Besides the usual teaching responsibilities in undergraduate and graduate courses, special emphasis is put on the education of diploma and doctoral students in the physics and technology of present and future devices and of low dimensional semiconductor structures.

Contents

Tuning the piezoelectric fields in quantum dots: Electronic and optical properties of [*N*11] grown nanostructures

Stefan Birner[1], Michael Povolotskyi[2], Aldo Di Carlo[2], and Peter Vogl

Recent advances in growth techniques have made semiconducting quantum dots (QD) and quantum wires grown along [*N*11] directions a reality [1]. In contrast to the traditional (001) orientation, this geometry enables significant piezoelectric fields in the case of polar semiconductors crystallizing in the zincblende structure, such as GaAs, InAs and their alloys. These fields lead to a quantum confined Stark effect, which efficiently affects the optical properties of (*N*11) oriented devices. Consequently, an increasing number of experimental studies has been devoted to such promising systems. However, due to the complex geometry of (*N*11) oriented structures only few theoretical investigations have been performed in this domain.

We theoretically studied the elastic deformation and piezoelectric fields in InAs quantum dots grown on (*N*11) GaAs substrates within the continuum elasticity theory. Our model QD has the shape of a symmetric truncated tetrahedral pyramid, its height is 4 nm and it is located above a 1 nm InAs wetting layer. Particular attention was given to the influence of substrate orientation on both the volume deformation of the dot and the strain-induced piezoelectric field due to the non-zero shear strain. The influence of the piezoelectric fields on the electron and hole ground states for an (*N*11) QD was investigated within the envelope function approach using a position dependent effective mass tensor for the highest valence band obtained from the strain dependent Bir-Pikus 6×6 **k·p** Hamiltonian. All calculations were performed using the next**nano**[3] device simulator that has been developed at the Walter Schottky Institute [2].

Heterostructures made of materials with different lattice constants are subjected to elastic deformations. This volume deformation of the crystal is represented by the hydrostatic strain $\mathrm{Tr}(\boldsymbol{\varepsilon}_{ij})$ and depends strongly on the orientation of the substrate as shown in Fig. 1 for a pyramidal shaped InAs quantum dot embedded in a GaAs matrix. As these quantum dots differ with respect to their strain fields, different piezoelectric potentials act on them (see Fig. 2) that alter the conduction and valence band edges. We note that the piezoelectric field has the highest magnitude for the (111) growth direction. The field gets smaller with increasing *N* and finally vanishes for the case of [100] growth direction (not shown here). Due to the nature of the piezoelectric effect, the sign of the piezoelectric charge depends on the atomic composition of the

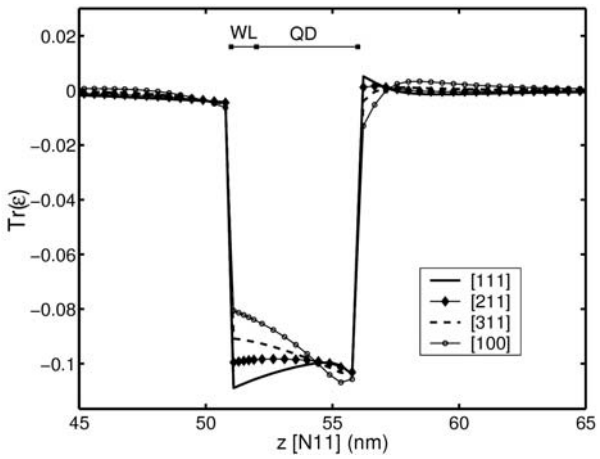

Fig. 1: *The hydrostatic strain along the fourfold QD symmetry axis for four different orientations of the substrate (111), (211), (311) and (100). The 1 nm InAs wetting layer (WL) and the InAs QD (height 4 nm) locations are indicated.*

[1] email: stefan.birner@nextnano.de
[2] Department of Electrical Engineering, University of Rome “Tor Vergata”, Italy

interface. We thus have to distinguish between the substrate's Ga planes, referred to as (*N*11)A, and the As planes, referred to as (*N*11)B. From a computational point of view, these two cases differ in the sign of the piezoelectric constant. There are two reasons for the piezoelectric charge existence, namely the discontinuity of the piezoelectric constant at the interface and the non-zero gradient of strain. We find that the piezo charge distribution in (*N*11) QDs has a dipole symmetry rather than a quadrupole symmetry as was found for (100) oriented dots [3].

Our study enables us to consider two effects on the electron and hole states, namely the effect of strain and the effect of piezoelectric charge. The effect of strain in our model does not depend on the substrate termination type but the piezo effect does. The electron and hole eigenstates were obtained as the solutions of the one-particle Schrödinger equation. In order to investigate the role of the piezoelectric field, we calculated the fundamental transition energy without any piezoelectric field and with the field, for both the A and B type substrate. We found that the fundamental transition energy can either be reduced or enlarged by the piezoelectric field. This is because the electric field can increase or decrease the spatial separation of the electron and hole wavefunctions that already exists due to the non-symmetric strain pattern. Its influence on the eigenfunctions is larger in the case of (*N*11)A substrate than in the case of (*N*11)B substrate (not shown here). The opposite is true for the eigenenergies, the corresponding energy shift is plotted in Fig. 3. We see that the effect has different sign depending on the substrate termination, and different magnitude which increases as the [*N*11] growth direction deviates from [100] towards [111] direction.
Our calculations demonstrate that by varying the growth direction and the substrate termination type, it is possible to tailor the built-in electric field, and thus the optical transition energy of these QD systems. [4]

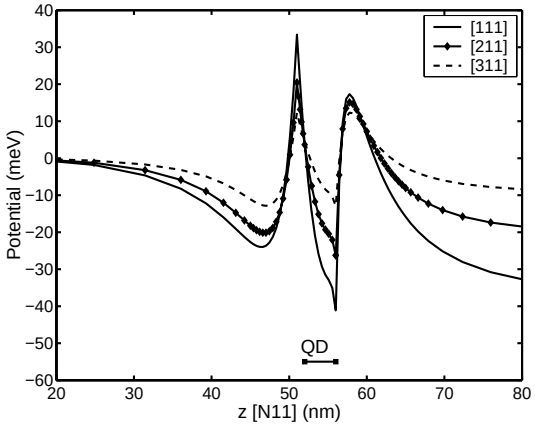

Fig. 2: *The piezoelectric potential along the QD symmetry axis calculated for three different orientations of the substrate; (111)A, (211)A and (311)A. The QD location is shown.*

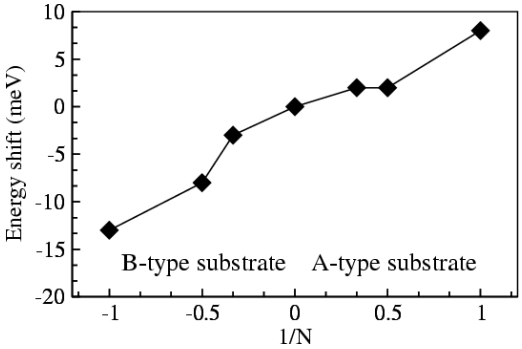

Fig. 3: *The fundamental transition energy shift due to the piezoelectric effect with respect to the case of no piezo effect. The axis of abscissae indicates the substrate orientation. Positive numbers correspond to (N11)A substrate, negative numbers to (N11)B.*

[1] P. Gonzales-Borrero et al., J. Cryst. Growth **169**, 424 (1996)
[2] next**nano**³ - next generation 3D nanodevice simulator
The software is available from www.wsi.tum.de/nextnano3 and www.nextnano.de.
[3] O. Stier et al., Phys. Rev. B **59**, 5688 (1998)
[4] M. Povolotskyi et al., IEEE Transactions on Nanotechnology **3**, 124 (2004)

supported by DFG (SFB 348), Office of Naval Research and the PAIS-PIE fund of INFM (Italy)

Dynamics of optically generated charges in InGaAs/GaAs quantum dots

Miro Kroutvar[1], Yann Ducommun, Jonathan Finley, Max Bichler, Dieter Schuh, and Gerhard Abstreiter

Recently, various proposals have appeared for the use of charge excitations (excitons) in semiconductor quantum dots (QDs) as fundamental hardware for quantum information processing (QIP). This interest has been partly stimulated by predictions and experimental observations of long excitonic coherence times, the origins of which can be traced to the fully quantized electronic structure. In this context, progressing beyond the exciton lifetime by eliminating exciton recombination is an interesting challenge requiring the development of schemes for selective optical charging of QDs. In this report, we present a study of the dynamics of resonantly photogenerated charges in a QD-based charge storage device as a function of lattice temperature and excitation energy relative to two-dimensional continuum states in the underlying wetting layer.

The charge (electron or hole) storage mechanism is based on selective ionization of excitons generated within the QD ensemble following resonant optical excitation at energy $\hbar\omega_w$. Exciton ionization in the intrinsic electric field of the photodiode leads to selective QD charging by virtue of an $Al_{0.4}Ga_{0.6}As$ barrier grown adjacent to the QD layer and inhibiting the escape of the minority carriers (fig. 1a, example for a hole storage device). The spectral distribution of stored charges and its temporal dynamics can then be directly probed by electrically neutralizing the stored charge after a delay time Δt by forward biasing the Schottky contact. This results in injection of majority carriers into the charged dots followed by a delayed luminescence signal $\hbar\omega_r$, hereafter termed the *storage* spectrum to distinguish it from conventional photoluminescence (fig. 1b).

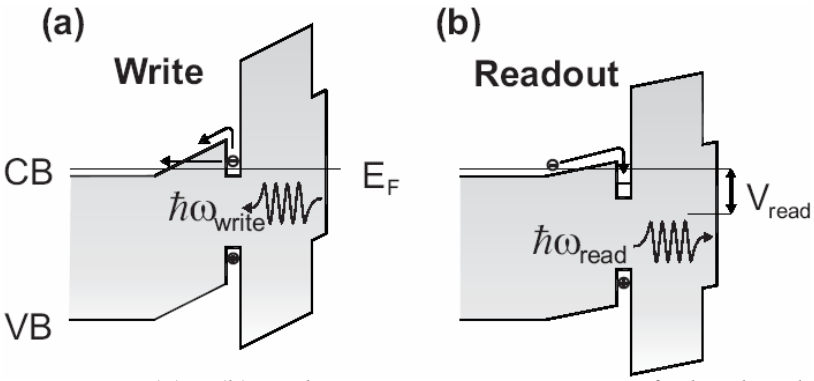

Fig. 1: *(a), (b) Schematic representation of the band structure of the hole storage device with a top-gate bias corresponding to write (a) and readout (b) modes.*

Fig. 2a,b shows two series of hole storage spectra with increasing storage times Δt = 200 ns, 1µs and 5 µs (from top to bottom). The spectra were recorded with $\hbar\omega_w$ = 1.298 eV at lattice temperatures of 50 and 60 K in figs 2a and 2b respectively. At the shortest storage times investigated (Δt = 200 ns), the spectra consist of two main peaks. The sharp peak close to $\hbar\omega_w$ (labeled **R** in fig. 2) corresponds to the direct, selective charging of QD ground states addressed by the excitation laser, while the lower energy, broad sideband **S** arises mainly from dots that are non-resonantly excited via their excited states, with a possible contribution from LO-phonon assisted absorption.

[1]phone:+49-89-289-12736, fax:+49-89-320-6620, email: kroutvar@wsi.tum.de

Increasing the storage time Δt allows investigation of the post-absorption dynamics of the photogenerated charge distribution: at elevated temperatures, redistribution of resonantly stored charges among the QD ensemble may take place within the storage time. The data presented in fig 2 show that the intensity of the spectra recorded at T = 50 K are time independent: no loss of spectral information, such as a transfer of intensity from the resonant peak **R** to a broad background**,** is observed, confirming that thermally driven carrier redistribution does not occur for this particular combination of temperature and excitation energy, over the investigated time window. In contrast, the series of spectra recorded at T = 60 K evolve markedly with time. The resonant peak is found to quench over a microsecond timescale, whilst the background simultaneously gains intensity in an anti-correlated manner. Furthermore, we observe that the total intensity of the storage spectra remains constant, excluding the loss of stored charges. We remark that the electron and hole storage devices exhibit comparable behavior, but over a different timescale. When considered together, these observations can be explained by dot-dot charge redistribution, whereby resonantly stored charges escape from the QDs where they were generated (reducing the intensity of **R)** and are subsequently randomly recaptured into other QDs within the ensemble (enhancing the background).

In order to identify the dominant charge redistribution channel, we performed an Arrhenius analysis of the fitted temperature-dependent carrier redistribution rate for both electron and hole storage devices for three different excitation energies. Remarkably, the energy of the redistribution channel was found to be constant for all three excitation energies investigated, confirming that redistribution occurs via a channel at fixed energy. Altogether, our findings strongly suggest that carrier inter-dot thermal redistribution via 2D wetting layer states provides a mechanism for loss of spectral selectivity over time for our devices.

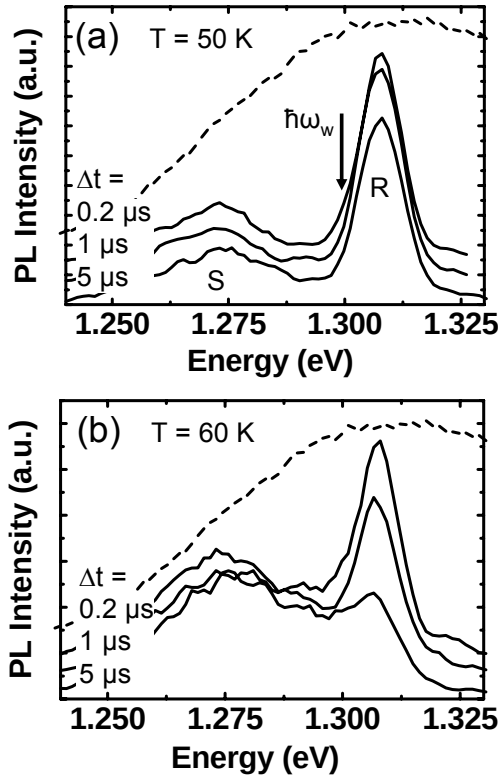

In summary, our field-effect device allows selective optical charging of sub-ensembles of self-assembled InGaAs/GaAs QDs using resonant optical stimulation. Post-absorption redistribution of resonantly generated charge amongst the QD ensemble was shown to occur over microsecond timescale at elevated (T ~ 100 K) temperatures.

Fig. 2: *(a) and (b) Series of hole storage spectra taken at T = 50 K (a) and T = 60 K (b) for increasing charge storage time Δt = 200 ns, 1 µs and 5 µs. The excitation energy was* $\hbar\omega_w = 1.298$ *eV.*

supported by DFG 348, Teilprojekt B1

The nature of the excitonic ground state in quantum dot molecules

H. J. Krenner[1], M. Reimer, W. Prestel, M. Sabathil, M. Bichler, D. Schuh, J. J. Finley, and G. Abstreiter

Due to their discrete electronic structure and ultra-long dephasing times, semiconductor quantum dots (QDs) are often considered to be the solid-state analogue of atomic systems. As such, they are widely regarded as a promising nanostructure for solid-state implementations of quantum information processing, the single exciton transition representing a potential qBIT. In order to explore the potential these systems provide for scalability and ultimately demonstrate quantum conditional logic, a fundamental prerequisite is the controllable *coupling* of individual qBITs (QDs). Coupled QD molecules (QDMs) are furthermore proposed as an efficient source of entangled photons or electron spins.

In this report, we present first studies on the nature of the excitonic ground state of QDMs. Recent theoretical investigations predict a strong characteristic dependence of the excitonic states in QDMs on static electric fields. In stacked QD structures between two species of excitons can be distinguished: direct and indirect excitons where e and h are localised in the same or in different QDs respectively. These two species are expected to be much different with respect to their electro-optical properties. Direct (indirect) excitons exhibit a small (large) excitonic dipole and a high (weak) e-h overlap. Under electric field perturbations the excitonic ground state in QDMs undergoes a transition from a direct to an indirect state. The Stark shift is expected to be anomalous since it reflects the properties of both the direct and the indirect exciton.

To experimentally test these predictions two layers of stacked self-assembled $In_{0.5}Ga_{0.5}As$ QDs separated by nominal spacer layers ranging from 7 to 13nm are embedded in field-tuneable *n-i*-Schottky junctions as depicted in Fig. 1. The samples are processed as photodiodes. By applying a bias voltage (V_B) on the semitransparent gate with respect to the n-contact the electric field F across the intrinsic layer can be tuned over a range of $0 - 250\,\frac{kV}{cm}$. Experiments focussed on *ensembles* of QDMs in order to get information of the general properties of QDMs.

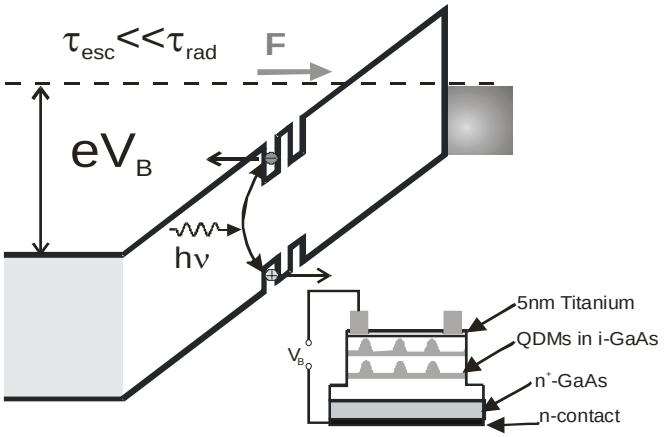

Fig. 1: *Sketch of bandstructure in photocurrent regime and the fabricated device*

Light from a halogen lamp was dispersed by a 0.64m grating monochromator and focussed on the sample. The resulting photocurrent was detected by a lock-in technique. Photocurrent spectra were taken as a function of the electric field. A room temperature (300K) photocurrent sweep of a sample with a QD layer separation of 7nm (effective QD separation ~2-3nm) is presented in Fig. 2. The clearly resolved ground state (E_0) exhibits an increasing redshift. This redshift is accompanied by a progressive reduction of the PC

[1]phone:+49-89-289-12736, fax:+49-89-3206-620, email: krenner@wsi.tum.de

amplitude. At low fields an excited state with comparable Stark shift is resolved. The behaviour described is completely different from observations on samples containing only one layer of QDs where all states show similar Stark shifts and the PC amplitude is merely independent on the electric field. In addition the Stark shift for single QD layers is much weaker than the one observed for the ground state of the QDMs. We attribute the observations to a field-driven anti-crossing of optically active (direct) excitons where electron and hole are localised in the same QD and optically inactive (indirect) excitons where electron and hole are localised in the two different QDs. For strong tunnelling coupling the transformation of the ground state to an optically inactive state is taking place over a wide field range due to the initially strong hybridisation of the electron state. Therefore higher fields are necessary to localise the electron fully in one of the two QDs. This leads also to a progressive quenching of the ground state oscillator strength.

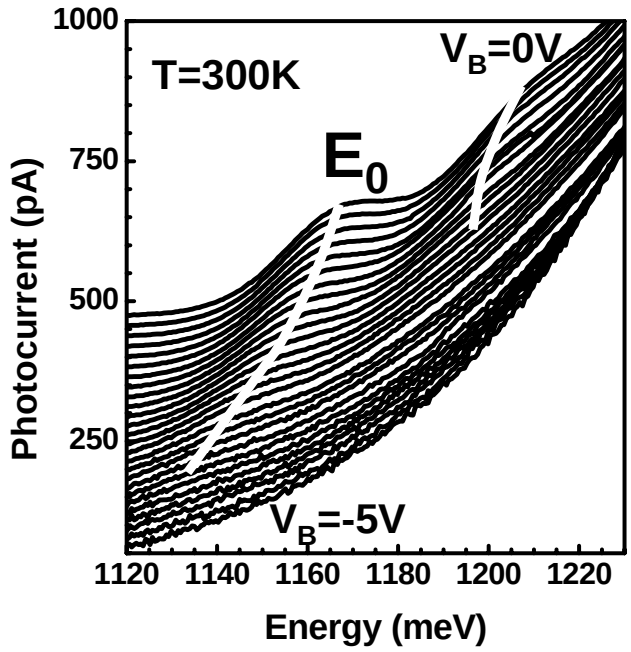

Fig. 2: *Bias-dependent direct photocurrent spectra*

The theoretically expected anomalous Stark shift and e-h overlap of the ground state are in good qualitative agreement with the transition energy and normalised amplitude of the PC obtained experimentally as depicted in Fig. 3.

In summary we have evidence of an electric *field-driven anti-crossing of direct and indirect excitons* in QDMs. This behaviour reflects a *general property* of QDMs since the presented experiment was performed on an ensemble of QDMs.

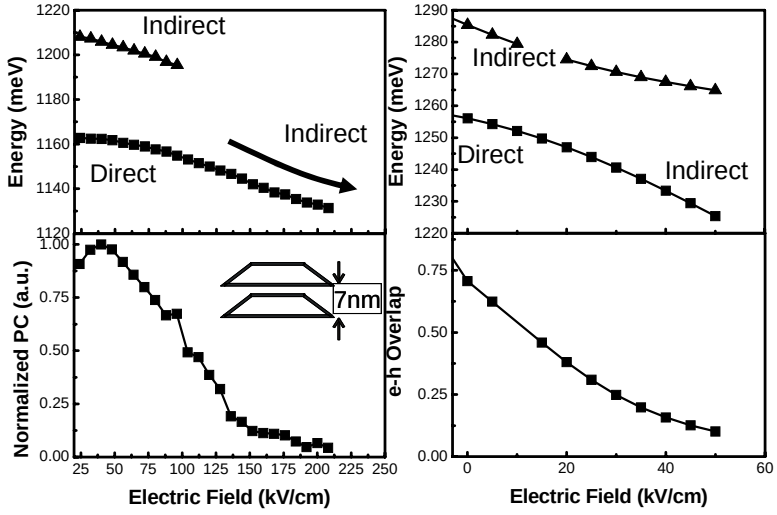

Fig. 3: *Comparison between experimentally obtained (left panel) transition energies and PC amplitude and theoretical expected behaviour (right panel)*

Supported by DFG via SFB 631, Teilprojekt B5

Integration and coupling of quantum dots in microresonators

A. Kress[1], F. Hofbauer, J. J. Finley, M. Bichler, D. Schuh, R. Meyer, and G. Abstreiter

In the annual report 2002 we presented the principal aims of this project, which are the investigation and control of the light-matter interaction between fully localised (0D) electronic states, in semiconductor quantum dots (QDs), and quasi 0D-photonic states using photonic crystal microresonators. The discrete electronic structure of such QDs is by now well established and has led to a number of proposals for their implementation as non-classical (single photon) light sources as well as numerous applications in quantum information processing. Photon anti-bunching has recently been demonstrated in the temporal emission characteristics from individual quantum dots, but the realisation of a *high efficiency* single photon source is crucial for the successful future implementation of both quantum cryptography and photon based quantum information processing architectures. One promising approach to realise this challenging goal is to utilise defect microresonators incorporated into *active* 2D photonic crystals (PCs) containing quantum dots. Via this approach we want to realise an electrically driven efficient single photon source.

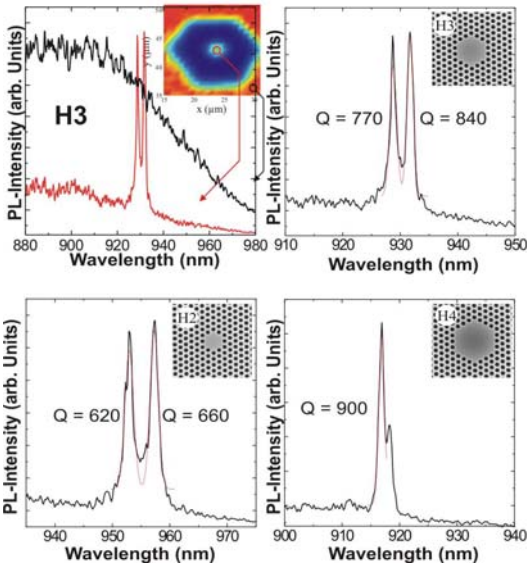

Fig. 1: *PL form different PCµC*

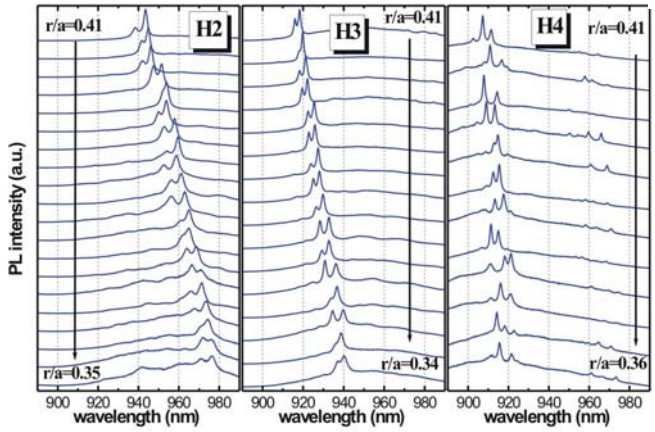

Fig. 2: *PCµC-modes for varying air-fill factor*

This time we present some important progress in the fabrication of 2D PCs, especially in terms of quality and control, investigations of the coupling of InGaAs self-assembled quantum dots (QD) to localised optical modes in 2D photonic crystal defect microcavities (PCµC). Our results enable us to probe the nature of individual cavity modes using spatially resolved micro-photoluminescence (µPL) spectroscopy and directly investigate cavity QED phenomena. We have measured a clear enhancement of the light-matter interaction in the weak coupling regime for QDs on-resonance with the cavity modes.

For future single photon devices implemented by combination of single QDs and PCµC the precise control of the cavity properties quality and resonance frequencies is essential. Figure 1 presents exemplarily the Q-factors obtained for different cavity sizes ranging from ~600 for a H2 defect (hexagonal defect with an edge of 2 missing holes, see inset) up to ~900 for a H4 defect (edge of 4 missing holes). Figure 2 shows measurements performed on a series of H4, H3 and H2 cavities for different ratios of radius over periodicity

[1] A. Kreß, Room S107, Phone +49 89 289-12784, email: kress@wsi.tum.de

(a=300nm) r/a = 0.34-0.41 (equal to air fill-factors *A*=0.33-0.64) and demonstrates control of the wavelength of the cavity modes (in the range ~910-990nm) with a precision better than $\Delta\lambda$~2nm. This precision in combination with Q-factors in excess of ~1000 allows the spectral selection between the exciton and bi-exciton state in a QD and therefore the potential application for an efficient deterministic single photon source.

Using spectrally resolved scanning µPL measurements, we have directly probed the symmetry and far-field emission pattern of *individual* localised optical modes in PCµC introduced into a 2D hexagonal lattice. A PL spectrum from the centre of a H4 cavity is shown in figure 3, where 5 modes are highlighted in blue. The spatial intensity distribution of the PL for highlighted modes is presented in the following 3-colour-plots. The plot for the integrated total intensity (simply achieved by integration over all slots of the CCD detector) represents the shape of the sketched defect (black line) whereas all other mappings show pattern of more or strong localised optical modes. Dipole and whispering gallery-like modes are identified for cavities with sizes ranging from H3 to H5. The maximum Q-factors have been measured for whispering gallery like modes, for example from the mode M5 of the H4 cavity in figure in excess of ~1000. This indicates that the Q-factor of the probed optical modes is limited by vertical radiation losses from the slab waveguide and not by fabrication imperfections.

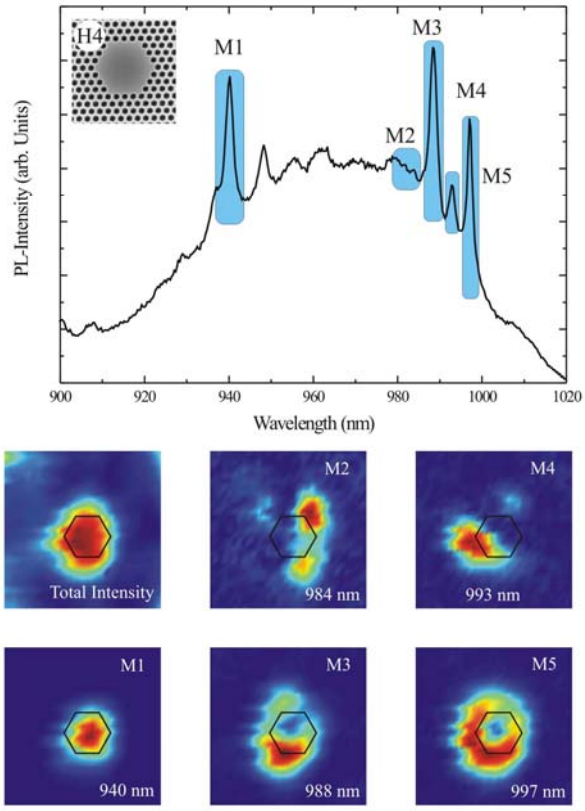

***Fig. 3**: Far-field emission patterns for different cavity-modes in a H4 PCµC*

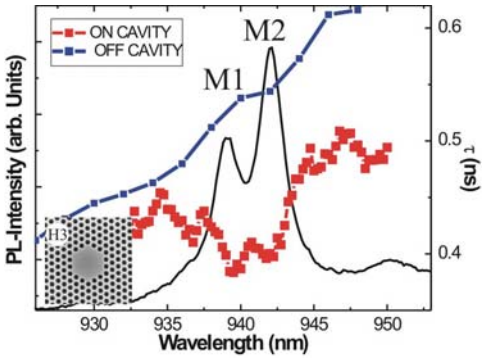

***Fig. 4:** Excitonic decaytime on a H3 PCµC and outside the cavity*

Up to an eightfold enhancement of the emission intensity is observed for QDs on-resonance with the cavity modes suggesting the presence of significant cavity QED phenomena (see fig.1). To clarify this observation, we performed time resolved luminescence measurements. The results reveal a 1.4 times enhancement of the spontaneous emission lifetime, called Purcell factor $F_p \sim Q/V_{mode}$, for a H3 mode shown in figure 4. The obtained Q-factors for the different hexagonal designs enable theoretical shortening of the emission lifetime of excitonic transitions in the embedded QDs from a factor ~2 for the H3 defect, ~4 for the H2 and up to ~8 for the H1 defect with Q~300.

Financial support by the DFG via SFB 631 “Festkörperbasierte Quanten-informationsverarbeitung: Physikalische Konzepte und Materialaspekte“ project B3.

Raman scattering of folded acoustic phonons in Si/Ge dot supperlattices

Dominique Bougeard[1], PingHeng Tan, Hubert Riedl, Karl Brunner, and Gerhard Abstreiter

Due to the lattice mismatch of 4% between Ge and Si, self-organized Ge quantum dots (QDs) can be fabricated by self-assembly using the Stranski–Krastanov growth mode. Such Si/Ge dots are very promising, for example, for light detection in the midinfrared range. The response of such optoelectronic structures is often increased by deposition of superlattices (SLs) with many Ge dot layers separated by Si. Raman scattering has proven to be a versatile technique to characterize Si/Ge layer and dot SLs. We studied high-order folded acoustic phonon Raman modes to characterize the structural properties of self-organized Si/Ge dot SLs, such as the effective thickness of dot layers and the degree of thermal Si/Ge intermixing during annealing. Si/Ge dot samples were grown by self-assembly in a solid source MBE system on (001)-Si substrates at 510°C. The presented structures contain 80 periods of 8 ML Ge separated by 25 nm Si layers. Atomic force microscopy (AFM) of an uncapped reference sample reveals a lateral dot size of about 20 nm, a height of about 2 nm and a sheet QD density of $1.5 \cdot 10^{-11}$ cm^{-2}.

Figure 1 shows the Raman spectra of the Si/Ge dot SL measured in two scattering configurations after subtraction of the reference spectra from a Si substrate. The two strong peaks at high frequency are identified as Ge-Ge (307.5 cm^{-1}) and Ge-Si (421.5 cm^{-1}) longitudinal optical (LO) phonon modes. In the low frequency region, distinct sharp peaks up to 120 cm^{-1} and some weak features up to 180 cm^{-1} are observed. These peaks are assigned to the folded longitudinal acoustic (FLA) phonons in the Si/Ge dot SL. The doublets of the folded phonons are not resolved here because of the small frequency splitting of less than 1 cm^{-1} for 514.5nm excitation. A larger doublet splitting of 4.0 cm^{-1} is observed up to the eighth-order FLA modes when excited by a 647 nm laser, as shown in the inset of Fig. 1. The frequencies of the FLA modes in $Si/Si_{1-x}Ge_x$ layer SLs have been shown to be well described by the Rytov model. We were able to describe our dot layers by a nominally pure 1.1 nm Ge layer with the sound velocity and density of bulk Ge or by a 2.0 nm $Si_{0.46}Ge_{0.54}$ alloy layer with values linearly interpolated from Si and Ge bulk. For the intermediate Si layers we use a reduced sound velocity and density of bulk Si that were used to precisely fit the gap energy of FLA phonons in $Si/Si_{1-x}Ge_x$ SLs. The fitted result gives an average Ge content of 0.54 within a 2.0 nm dot layer. This corresponds to an actual Ge content of about 0.80 within Ge/Si islands, if we regard islands with pyramidal shape (truncated during Si overgrowth), a height of 2 nm and a surface

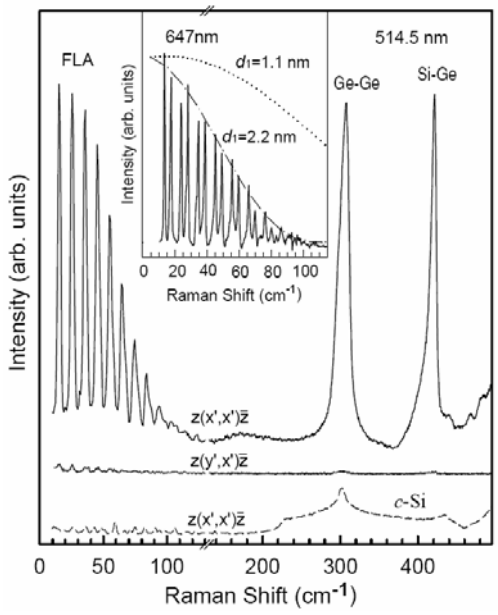

Fig.1: *Raman spectra of a Si/Ge dot SL (solid lines) and c-Si (dashed line) excited at 514.5 nm. z, x' and y' refer to [001], [110] and [110. The inset shows the FLA Raman spectrum excited at 647 nm. Dotted and dash-dotted lines are calculated envelopes of FLA mode intensities for dot-layer thicknesses of 1.1 nm and 2.2 nm.*

[1]phone:+49-89-289-12777, fax:+49-89-3206620, email: bougeard@wsi.tum.de

coverage of islands of 60%, as analyzed by AFM. This is in agreement with a Ge content of 0.82 within islands deduced from previous detailed LO phonon Raman studies. For both model descriptions, the Rytov model precisely fits the peak frequencies of FLA modes. Similarly, in x-ray diffraction (XRD) we observed SL (004) θ-2θ Bragg peaks up to about tenth order that can be simulated well by each of the two SL layer models. Thus, the fits of XRD curves or FLA Raman mode frequencies offer reliable values of the SL period and an average value of Ge content within a SL period.

The Raman spectrum of a Si/Ge dot SL sample in Fig. 2 shows distinct FLA modes up to 22nd order, which are presumably enhanced by resonant excitation. The highest observed mode frequency of about 220 cm^{-1} almost reaches the maximum value of the LA phonon dispersion of c-Ge at the edge of the Brillouin zone (BZ). The low-order FLA Raman lines are narrow and nearly symmetric indicating high-quality SLs with sharp interfaces. The frequencies of FLA phonons are shown in the inset of Fig. 2 as diamonds in the extended BZ scheme. The calculated dispersion curves of the FLA phonons using the Rytov model are also plotted in the inset of Fig. 2 as dashed lines in the mini zone and extended BZ schemes. The FLA modes in Si/Ge dot SLs up to 150 cm^{-1} are again well described by the Rytov model. By additional consideration of the nonlinear acoustic phonon dispersion of c-Si, the calculated dispersion curves of the Si/Ge dot SL (solid line in the inset of Fig. 2) are in excellent agreement with the experimental results in the whole observed spectral range. This indicates that the observed frequency reduction of the higher order FLA modes results from the nonlinear phonon dispersion curve of c-Si.

Under nonresonant conditions fulfilled e.g. at 647 nm excitation, due to the photoelastic effect, Raman scattering from folded acoustic phonons can be treated as a coherent sum of scattering within bulk-like layers. The scattered mth-order FLA Raman intensity I_m is then related to the SiGe alloy layer thickness and the SL period. We fitted the spectral envelope of FLA mode intensities using the above equation (dash-dotted line in the inset of Fig. 1). The fitted thickness of the Ge dot layer is 2.2 nm, which is in excellent agreement with the effective height of Si/Ge dot layers deduced from AFM studies. The calculated spectral envelope for a pure Ge layer with the nominal thickness 1.1 nm (dotted line in the inset of Fig. 1), in contrast, is very different from the observed profile. Therefore, the actual (Si)Ge layer thickness that is influenced by island formation, Si overgrowth and possible intermixing is sensitively analyzed by the spectral envelope of FLA modes observed in nonresonant Raman studies. Island formation appears to influence the FLA Raman modes mainly by the resulting increase of the effective dot layer width. Distinct FLA modes defined by the average SL composition profile are observed in the studied QD SLs.

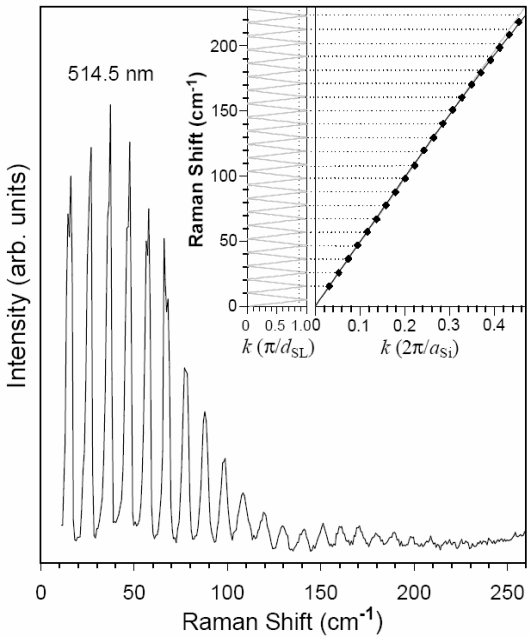

Fig.2: *FLA Raman spectra of a dot SL The insets show the calculated linear (nonlinear) dispersion curves of LA phonons as gray (black) Diamonds show the observed FLA phonon frequencies.*

supported by the DFG (Grant No. Ab 35/3-2) and the BMBF (SOWASI Grant No. 13N7870)

A new quantum wire structure fabricated by double cleaved-edge overgrowth

Sebastian Roth[1], Matthew Grayson, Dieter Schuh, Max Bichler, and Gerhard Abstreiter

The cleaved-edge overgrowth method makes it possible to fabricate very clean one-dimensional wires in the GaAs/AlGaAs material system, having atomically precise control over the structural design. Quantum wires are expected to show Luttinger liquid behavior at low temperature, giving the opportunity to explore electron-electron interactions, which strongly affect the transport properties of such systems. In a spin-degenerate noninteracting quantum wire the conductance through the channel is quantized in units of $n \cdot 2e^2/h$, for n occupied 1D subbands.

In our work we demonstrate a new quantum wire structure, in which the potential over the whole length of the channel can be modulated with atomic precision. Such systems are believed to be strongly affected by the interaction between carriers. Theory predicts that if a single barrier is introduced, the conductance through the wire will obey a power law in temperature. By creating an artificial island between two barriers, effects associated with the Coulomb blockade can be observed. Even a Mott-insulating state may be achieved by adding multiple barriers to modulate the potential periodically over the channel length and tuning the electron density with a gate to half filling.

To realize such strucures we perform double cleaved-edge overgrowth. The second and third growth steps in our double-cleave wires are analogous to the first and second growth steps in single-cleave wires. First, substrate layers are grown in (001)-direction, sandwiched by two n^+ contacts. After cleaving the sample in-situ a modulation-doped gated 2DEG is grown in (110)-direction. In the third growth step a modulation-doped AlGaAs barrier is added in the $(1\bar{1}0)$-direction, leading to an additional confinement of the electrons in the 2DEG and therefore to an accumulation of wire states at the cleavage plane. The wire channel is oriented along the primary growth direction. A variation in the substrate potential can be directly transferred to the adjacent quantum wire.

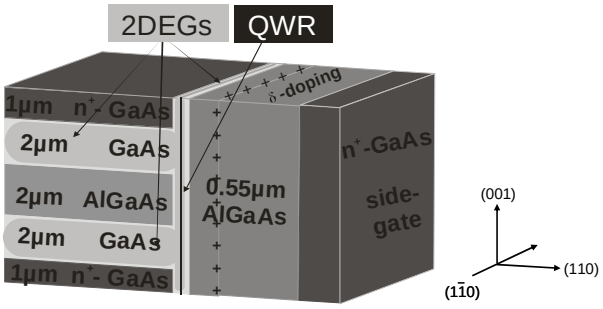

Fig. 1: *Double-cleave structure shown without final $(1\bar{1}0)$-growth. The QWR is contacted by 2DEGs in the GaAs substrate layers and the GaAs quantum well*

As a first step to realize the more complicated structures mentioned above we have to demonstrate a simple quantum wire in this double-cleave geometry. Fig.1 shows the sample structure without the layers grown in $(1\bar{1}0)$-direction. The quantum wire along the (001)-direction is contacted by the 2DEGs in the GaAs substrate layers and the quantum well. The electrons in the quantum well are confined in a triangular potential next to the GaAs substrate layers and a square potential along the AlGaAs substrate layer, leading to a high-density and a low-density region of the 2DEG. A negative gate voltage depletes the low-density 2DEG, leaving only a 2µm long quantum wire.

[1]phone:+49-89-289-12736, fax:+49-89-3206620, email: roth@wsi.tum.de

SdH-Oscilations of the quantum well 2DEG with a magnetic field applied in the (110)-direction clearly show the different 2DEG densities in Fig.2a. Fig.2b shows the gate voltage dependence and the extrapolated pinch-off values of the 2DEG for dark conditions

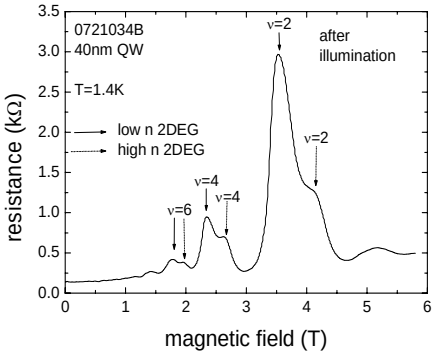

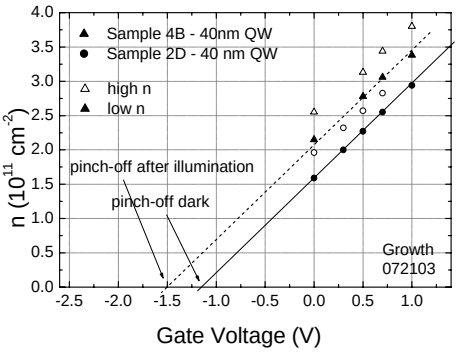

Fig. 2 a): *SdH-Oscilations show different 2DEG densities*

Fig. 2b): *n vs. U_{Gate} marks pinch-off values of 2DEG*

and after illumination.

Measuring the AC-conductance of a dark sample we observe a complete pinch-off of the low-density 2DEG at the expected values of -1.1±0.1 V, shown in Fig 3. After illuminating the sample with an IR-LED the pinch-off moves to more negative gate voltages around -1.7±0.1 V and a residual conductance plateau of order e²/h evolves, nearly unaffected by further decrease of the gate voltage. This feature is observed in several samples and indicates the accumulation of quantum wire states. Only in some

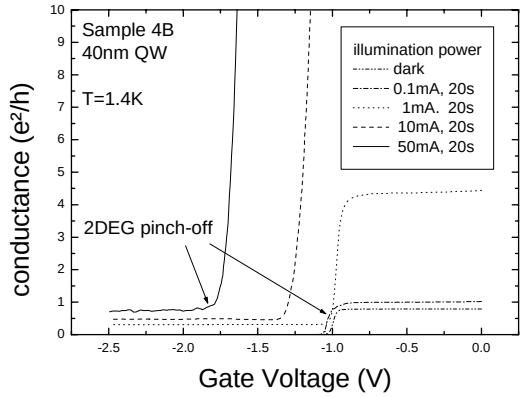

Fig. 3: *Trace of a sample without pinch-of for different illumination conditions*

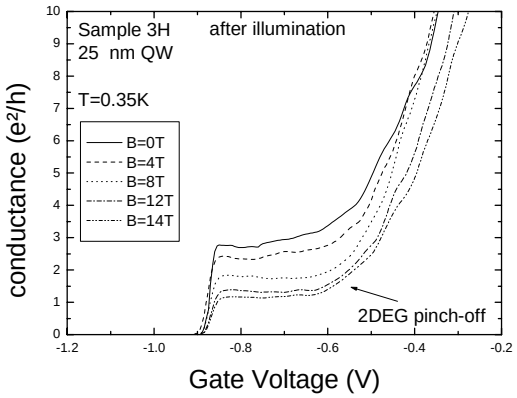

Fig. 4: *Traces of a sample with pinch-off for different magnetic field strength*

cases, however, can this plateau be pinched off, as shown in Fig.4. We also investigated the dependence of the feature with a magnetic field oriented in $(1\bar{1}0)$-direction, finding that the plateau value decreases with increasing magnetic field strength. We identify this behavior with the magnetoresistance of the 2DEG contacts.

Another indication for the existence of a quantum wire is given by the temperature dependence of the feature. While remaining at a conductance value below 2e²/h at low temperatures it rises to this exact quantization unit at higher temperatures. This can be explained by disappearence of 2D-1D scatterig, as observed in single-cleave wires.

supported by BMBF (01BM912)

Paramagnetic defects in Si nanowires

Andrea Lehner[1], Martin S. Brandt, and Martin Stutzmann

Currently, one-dimensional nanostructures, such as nanowires, receive considerable scientific interest due to their potential to test fundamental concepts of how dimensionality and size affect physical properties. Furthermore, nanowires could serve as critical building blocks for emerging nanotechnologies. With the objective of constructing electronic devices made of nanowires one has to consider the electronic properties, such as the defect density very carefully. Especially, the surface properties play an important role due to the large surface/volume ratio in low-dimensional structures. For crystalline silicon, passivation of surface defects by HF-etching is well-established. For silicon nanowires, successful hydrogen termination has been reported by Sun et al. [1]. The aim of our work is to determine the nature of the paramagnetic defects as well as the defect density in the as grown silicon nanowires by electron spin resonance (ESR) measurements. Further, the influence of HF- etching on the defect density has been studied.

Silicon nanowires were prepared by thermal evaporization at the Center of Super-Diamond and Advanced Films, Hong Kong. As described in literature [2], the as grown silicon nanowires have a crystalline core measuring 10-15 nm in diameter which is sheated with a 3-5 nm thick oxide layer. Hydrogen termination was performed by immersing the as grown silicon nanowires into an aqueous solution of 5% HF for about 5 min. Subsequently, the HF was removed by repeated dipping into H_2O. Finally, the samples were dried in a stream of N_2. To verify the successful hydrogen termination, Fourier transform infrared (FTIR) spectra were aquired at room temperature using a Bruker IFS 113V FTIR system. To this end, the silicon nanowires were finely ground and dispersed in dried spectroscopic grade potassium bromide (KBr). After correction for the KBr signal, the infrared absorbance was calculated. In Fig. 1 the infrared absorbption of the hydrogen terminated nanowires is plotted as a function of the wavenumber and is compared to the as grown nanowires. The broad peak around 1080 cm^{-1} (a), which is caused by Si-O-Si stretching vibrations, indicates the presence of a large amount of oxide on the as grown nanowires. By HF-etching this peak vanishes almost completely. At the same time, H-Si stretching vibrations appear in the spectrum at 2100 cm^{-1} (b) showing the successful termination of the wire surface. For the as grown nanowires, no vibration lines due to hydrogen could be found.

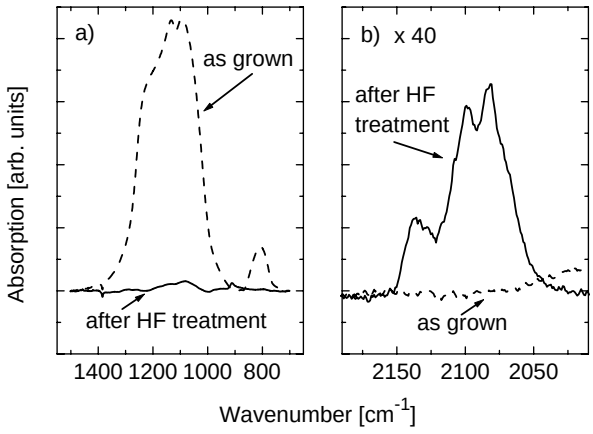

Fig. 1: *FTIR spectra of the as grown and the hydrogen terminated silicon nanowires. The curves in (b) are stretched by a factor of 40. By HF-etching the large oxide peak at 1080 cm^{-1} disappears and Si-H vibrations at 2100 cm^{-1} are generated.*

[1]phone:+49-89-289-12755, fax:+49-89-289-12737, email: lehner@wsi.tum.de

With this ability to tune the surface termination from oxidized to hydrogen terminated, we studied the paramagnetic defects in the silicon nanowires by electron spin resonance (ESR) measurements. For the ESR experiments, small amounts (approximatelly 1 mg) of nanowires were weighed and filled into small teflon tubes, which were then sealed with teflon tape. These teflon tubes were put inside a standard ESR quartz tube. ESR measurements were performed in a conventional CW X-band ESR spectrometer (Bruker ESP-300, with a TE102 cavity) operating at 9.27 GHz. A magnetic field modulation amplitude of 2.02 Gauss and a microwave power of 1 mW was used. The results of the ESR measurements of the as grown and hydrogen terminated nanowires are shown in Fig. 2. The spectrum of the as grown nanowires can be deconvoluted into three lines. First, there is a broad ESR line at g = 2.0050 which can be attributed to dangling bonds in the amorphous silicon/oxide matrix surrounding the crystalline core. Next, there is a sharp peak at g = 2.0007, which is a typical defect in SiO_2, the so called E´-center. Finally, a line at g = 1.998 is resolved which is due to conduction electrons in the crystalline cores. For the hydrogen terminated nanowires, all these peaks are significantly reduced. Beside the nature of the defects, we also analyzed the quantitative defect density in our samples. For the as grown silicon nanowires, a defect density of 4.4 $\cdot 10^{14}$ mg^{-1} was obtained. After HF-etching, the defect density is reduced by a factor of 40. By removing the oxide layer the E´-centers vanish since they were located within the oxide. Further, surface dangling bonds are saturated with hydrogen atoms and become electronically inactive. Although, hydrogen termination is known to be stable on silicon nanowires for about one day, for long term appilcations this time is still too short. Long-term stability can be obtained by terminating the surface with organic molecules, which is much more stable than hydrogen termination.

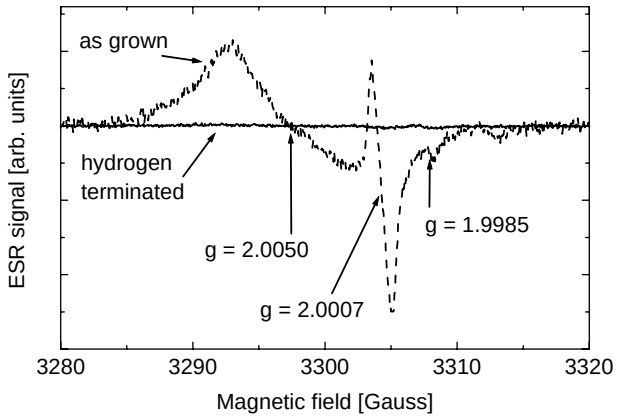

Fig. 2: *ESR spectra of the as grown and the hydrogen terminated silicon nanowires. Three lines are identified: dangling bonds at g = 2.0050, E´-centers at g = 2.0007 and conduction electrons at g = 1.9985. HF-treatment reduces the ESR signal drastically.*

[1] X. H. Sun, S. D. Wang, N. B. Wong, D. D. D. Ma, S. T. Lee; Boon, K. T. *Inorg. Chem.* **2003**, 42, 2398.

[2] Shi, W. S.; Peng, H. Y.; Zheng, Y. F.; Wang, N.; Shang, N. G.; Pan, Z. W.; Lee, C. S.; Lee, S. T. *Adv. Mater.* **2000**, 12, 1343**.**

supported by DFG (SFB 563 TP B2)
in collaboration with F. Au and S. T. Lee, Center of Super-Diamond and Advanced Films, Hong Kong

Edge-magneto plasmons in GaAs- and GaN-based two-dimensional electron gasses

Hans Huebl[1], Sebastian T.B. Goennenwein, Martin Stutzmann, and Martin S. Brandt

Among the different high-frequency properties of two-dimensional electron gasses (2DEGs), edge-magneto plasmons (EMPs) are peculiar in the sense that their properties depend on the 2DEG perimeter. With the possibility to form polarization-induced 2DEGs with very high carrier concentrations in GaN/AlGaN heterostructures, we have access to 2DEGs with electron densities covering more than one order of magnitude are now accessible, allowing for a critical test of the different EMP models proposed.

Edge-magneto plasmons can be thought to arise from a small displacement of a 2DEG with respect to the fixed atom cores, resulting in a positive and a negative line charge along opposite boundaries of the 2DEG sample. The mobile electrons move in the resulting electric field, yielding the classical plasma oscillations. If in addition a magnetic field B perpendicular to the 2DEG plane is present, the oscillating electrons will feel a Lorentz force which leads to a rotation of the line charge along the sample boundary. This rotary collective electron motion is referred to as the edge-magneto plasmon.

The oblate spheroid model (OSM model) is a first approach to account for the EMP quantitatively. Starting with a finite three-dimensional distribution of charges shaped as an oblate spheroid, Allen et al. [1] obtained for the resonance frequency of the EMP mode

$$\omega_{EMP} = \frac{3\pi^2}{8}\frac{ie}{\varepsilon_0\varepsilon_{eff}}\frac{n_{2DEG}}{PB} \qquad (1)$$

with the electron density n_{2DEG}, the electron charge e, the dielectric constant ε_0, the 2DEG perimeter P, the mode index i and the effective dielectric constant ε_{eff}, which is typically approximated by the average of the dielectric constants of the host material (ε_{GaAs} or ε_{GaN}) and the surrounding helium gas (ε_{He}). The OSM model accounts for effects of the polarizability of the media surrounding the 2DEG, but neglects effects caused by fringing fields at the boundary of the sample as well as the constant electron density over the sample area.

We have investigated the microwave-frequency properties of 2DEGs using a standard electron paramagnetic resonance setup. Our experiments are performed at temperatures between 5 K and 8 K, using a He gas-flow cryostat. Due to the magnetic field modulation and lock-in detection used, the spectra obtained show the derivative of

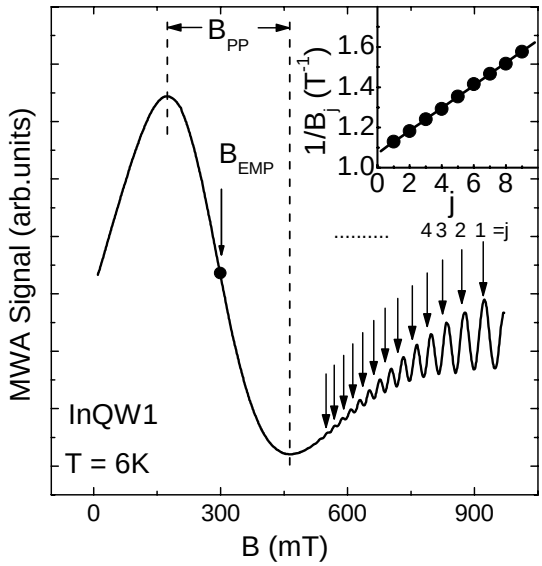

Fig. 1: *Microwave absorption spectrum of a $In_{0.15}Ga_{0.85}As$ quantum well sample, with the 2DEG plane oriented perpendicularly to the external magnetic field. The inset shows the inverse magnetic field of the oscillations plotted over the index j. The linear dependence is an indication of the Landau quantization of the system at high fields.*

[1]phone:+49-89-289-12768, fax:+49-89-289-12737, email: huebl@wsi.tum.de

the microwave absorption of the sample as a function of the applied magnetic field. We have investigated three types of heterostructures: (i) $In_xGa_{1-x}As$ quantum wells, consisting of 12 nm $In_xGa_{1-x}As$ with an In concentration of x = 0.10 or x = 0.15 sandwiched between GaAs barriers, (ii) a $GaAs/Al_{0.3}Ga_{0.7}As$ heterostructure and (iii) a $GaN/Al_{0.12}Ga_{0.88}N$ as well as a $GaN/Al_{0.08}Ga_{0.92}N$ heterostructure. Standard magneto-transport experiments show that the 2DEG density can be varied between $n_{2DEG} = 4 \times 10^{11}$ cm^{-2} and 1×10^{12} cm^{-2} in the GaAs-based samples, with a typical electron mobility $\mu = 1 \times 10^5$ cm^2/Vs in the InGaAs QWs and $\mu = 10^4$ cm^2/Vs in the GaAs/AlGaAs heterostructures at $T = 5$ K. The 2DEG density in the GaN/AlGaN samples are 2.25×10^{12} cm^{-2} and 3.7×10^{12} cm^{-2} for x = 0.12 and x= 0.08 respectively, with an electron mobility $\mu \approx 10^4$ cm^2/Vs at 5 K in both samples.

A typical microwave absorption (MWA) spectrum of an $In_xGa_{1-x}As$ quantum well, with the 2DEG plane perpendicular to the external magnetic field, is shown in Fig. 1. Two main features can be distinguished: A large resonance labelled B_{EMP} at low magnetic field, and a series of oscillations in the MWA for $B > 0.5$ T. Their $1/B$ periodicity indicates that these quantum oscillations can be directly linked to the well-known formation of Landau levels, the resulting variation in conductivity resulting in a variation of the MWA.

All experimentally observed positions of the EMP resonances for the different samples, also varying the charge density n_{2DEG} by illumination and the sample perimeter P, are compiled in Fig 2. All EMP resonances in samples grown on GaAs substrates fall onto a single line, irrespective of the mobility of the 2DEG, the exact form of the confining potential, or the composition of the well or the barriers. A quantitative analysis of the slope yields an $\varepsilon_{eff} = 8.2$, which is 30% larger than the average of $(\varepsilon_{GaAs}+\varepsilon_{He})/2$.The deviation can be attributed to the fringing fields not included in the simple theory. The ε_{eff} obtained experimentally for the GaN-based heterostructures is 6.7, which is also 30% larger than the estimated value.

The results presented show that the rather simple OSM model is able to account for the observed resonances even over 1.5 orders of magnitude in the electron density, only taking into account the different substrate materials. In addition, the study shows that for the observation of electron spin resonance in such two-dimensional systems, it is necessary to take the size of the sample into account. By either using 2DEGs with very small or very large perimeter, the EMP resonance can be shifted outside the magnetic field range where the ESR is expected, thereby limiting the crosstalk between EMPs and ESR.

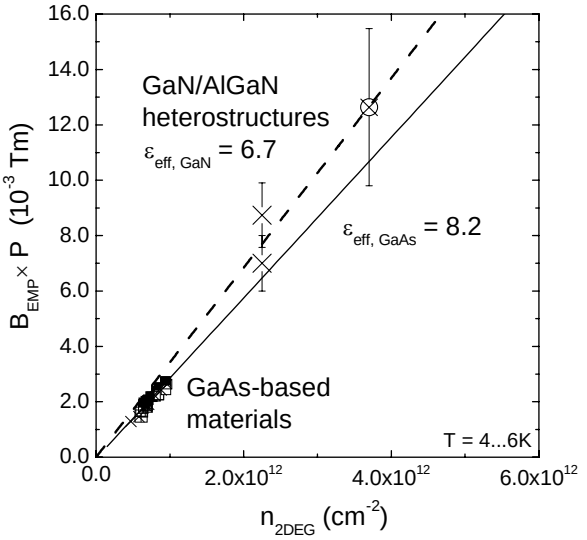

Fig. 2: *Plotting B_{EMP} x P versus n_{2DEG} leads to a linear dependence, as expected for the EMPs. From a fit to Eq. (1), one finds $\varepsilon_{eff,GaAs} = 8.2$, for the GaAs-based samples, and $\varepsilon_{eff,GaN} = 6.7$ for the GaN-based samples.*

[1] S.J. Allen, H.L. Störmer, and J.C.M. Hwang, PRB**28**, 4875 (1983)

supported by DFG (SFB348)

Hydrogen-control of ferromagnetism in magnetic semiconductors

Martin Brandt[1], Thomas A. Wassner, Hans Huebl, and Sebastian T.B. Goennenwein

During the last years, ferromagnetism has been reported in a variety of semiconductors such as GaAs, ZnTe and even Ge with Curie temperatures above 170 K. Ferromagnetic semiconductors are obtained when (i) large concentrations of local magnetic moments such as provided by the electrons in the unfilled *d* shell of the transition metal ions and (ii) large concentration of holes can be present in the material simultaneously. For the use in spintronic devices, it would be particularly desirable to electrically tune the spin polarization. However, the high hole concentrations of 10^{20} cm^{-3} and above allow switching of the magnetization via gates only in very thin films. We have in the last year developed an alternative technique to control the magnetization in GaMnAs, which is currently the best understood ferromagnetic III-V material, by post-growth incorporation of hydrogen.

Hydrogen is known to passivate acceptors in GaAs by the formation of electrically inactive complexes. Figure 1 a) shows the Mn acceptor in GaMnAs in a simple electron counting picture. One electron from the valence band is transferred into the sp^3 orbitals, leaving a mobile hole in the band. In contrast, when an additional electron is brought in by a hydrogen atom, this electron saturates the sp^3 orbitals, leaving the Mn electrically inactive (Fig. 1 b)). The local magnetic moment generated by the $3d^5$ electron configuration of the Mn is unchanged by the hydrogenation.

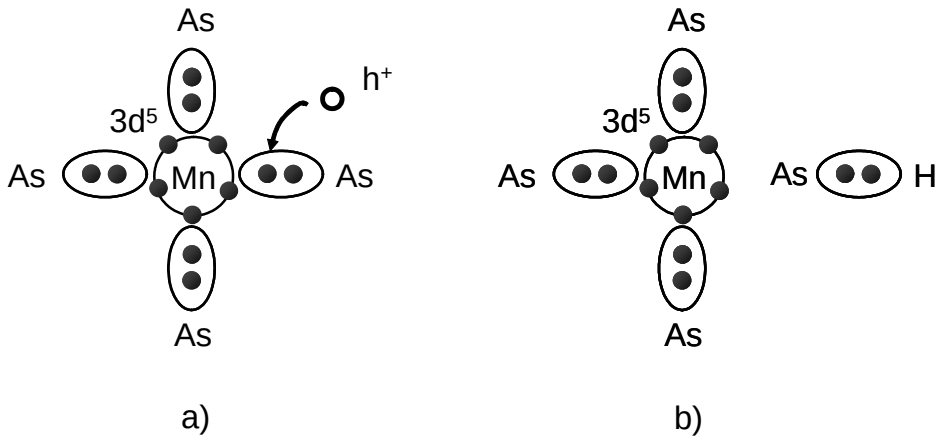

Fig. 1: *Valence electrons in the 3d and 4sp^3 orbitals of (a) a Mn accpetor in GaMnAs and of (b) a Mn-As-H complex in hydrogenated GaMnAs.*

The formation of such Mn-As-H complexes can be directly verified via the observation of characteristic local vibrational modes. Indeed, an As-H stretching mode at 2143 cm^{-1} is observed after hydrogenation of GaMnAs via Fourier-transform infrared transmission spectroscopy (Fig. 2). The same mode is also observed when other acceptors in GaAs such as Mg and Zn in GaAs are passivated with hydrogen. The lack of a clear influence of the exact chemical identity of the acceptor on the vibration frequency suggests that the H is backbonded at one of the As nearest neighbor atoms as shown in Fig. 1 b), rather than in the bond center between Mn and As.

[1]phone:+49-89-289-12758, fax:+49-89-289-12737, email: brandt@wsi.tum.de

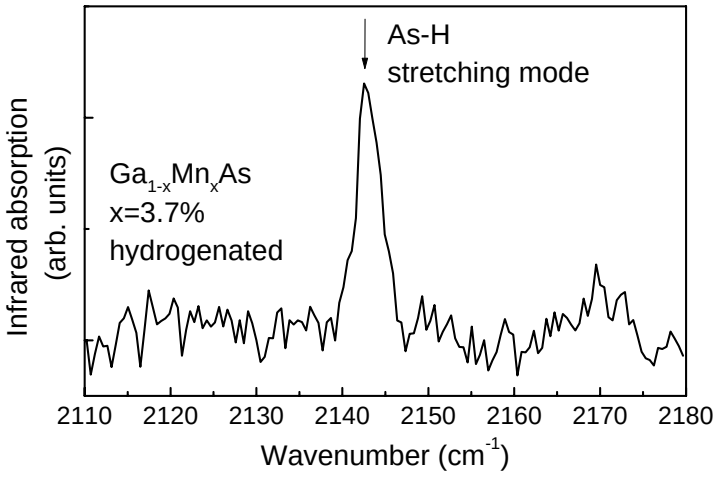

Fig. 2: *Fourier-transform infrared absorption spectrum of the As-H stretching mode characteristic for the formation of acceptor-hydrogen complexes in GaAs.*

Thin films of GaMnAs, which are metallic when ferromagnetic, become highly resistive after hydrogenation. And, as expected when one of the key prerequisites of the carrier-mediated ferromagnetism is removed, fully hydrogenated GaMnAs is paramagnetic, with no indication of ferromagnetism even at the lowest temperatures used to measure magnetization with a SQUID magnetometer (Fig. 3). A quantitative comparison of the saturation magnetizations shows that essentially no local magnetic moments have been lost by the hydrogenation, as expected.

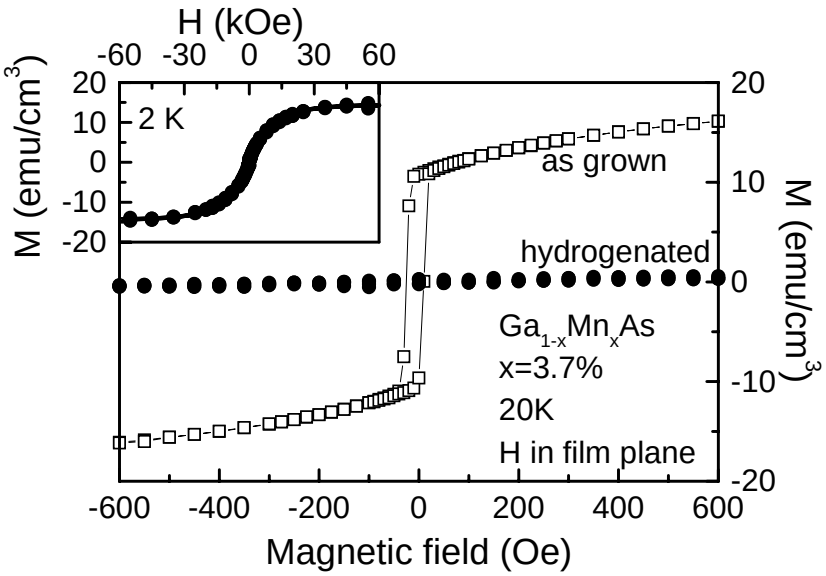

Fig. 3: *Magnetization loops of as-grown and hydrogenated GaMnAs. The insert shows the nearly perfect paramagnetic behavior of the hydrogenated sample as compared to the Brillouin function for S=5/2 and g=2.*

Since the magnetic anisotropy field reacts very sensitively on the hole concentration, post-growth hydrogenation could be a very interesting tool to form either ferromagnet/ semiconductor/ferromagnet heterostructures for tunneling magnetoresistance applications with very few interface defects from GaMnAs only, or to locally change the magnetic anisotropy and thereby form novel lateral or vertical anisotropy superstructures.

---

supported by DFG (SFB348)

A non-perturbative approach to Bloch electrons in magnetic fields

A. Trellakis[1] and P. Vogl

The problem of electrons moving under the influence of a three-dimensional periodic potential and a tunable magnetic field has become an intriguing subject due to its remarkable complexity. Here we find a rich array of nonperturbative physics, as for example the prediction of fractal energy spectra – the famous Hofstadter butterfly [1].

While experimental evidence for the existence of this phenomenon has now been found in the quantized Hall conductance of superlattices [2], much theoretical work is still needed in order to obtain a satisfactory description of semiconductor crystals in magnetic fields. Here, the first analysis of Bloch electrons in a magnetic field already dates back to Peierls, and is based on the tight-binding approximation. Within the envelope function approach, the standard method for introducing weak magnetic fields is an operator replacement procedure that is sometimes also called the Peierls substitution. But more recently it was shown that this approximation can lead to qualitatively incorrect results when the applied field introduces mixing between different energy bands. And the question of the integration path choice in tight-binding theory has not been entirely resolved yet [3].

The reason for these difficulties lies directly in the non-existence of a Bloch solution for an electron moving in a periodic crystal potential in the presence of a constant magnetic field. Here one finds that the vector potential of a constant magnetic field cannot be made periodic for any gauge choice. Consequently Bloch's theorem cannot be used to reduce Schrödinger's equation to the unit cell of the crystal lattice, and most of the standard methods in solid-state theory remain inaccessible. In this work, we present a nonperturbative solution for Bloch electrons in a magnetic field that is based on a singular gauge transformation for the vector potential. Using this singular gauge, the vector potential becomes now periodic and Bloch's theorem can be used to obtain an equation that is more accessible for further investigations [4].

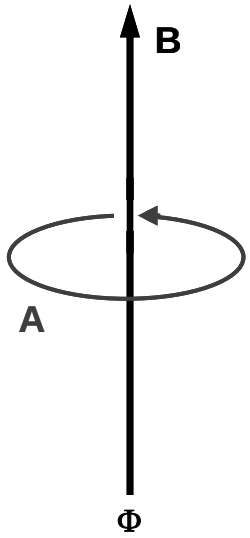

Fig. 1: *A magnetic flux line containing the flux Φ.*

In order to find a non-perturbative solution with the desired properties, we first consider the physical properties of magnetic flux lines. In this context, we define a magnetic flux line as the limiting case of a straight magnetic flux tube with infinite length and infinitesimal thickness. Fig. 1 shows such a flux line containing a magnetic flux Φ and the vector potential A that is generated by it. It should be emphasized that these flux lines are a purely mathematical trick. We also do not imply any connections to the magnetic field lines commonly used to illustrate plots of magnetic fields.

If we now examine the quantum mechanics of electrons moving in the vector potential induced by this flux line, we obtain the essence of the Aharonov-Bohm effect: An interference experiment with electrons around the flux line will obtain a phase shift that becomes a multiple of 2π for Φ being a multiple of the magnetic flux quantum $\Phi_0=e/h$. Consequently, a flux line containing a magnetic flux that is a multiple of Φ_0 is experimentally undetectable.

---

[1]phone:+49-89-289-12752, fax:+49-89-289-12737, email: alex.trellakis@wsi.tu-muenchen.de

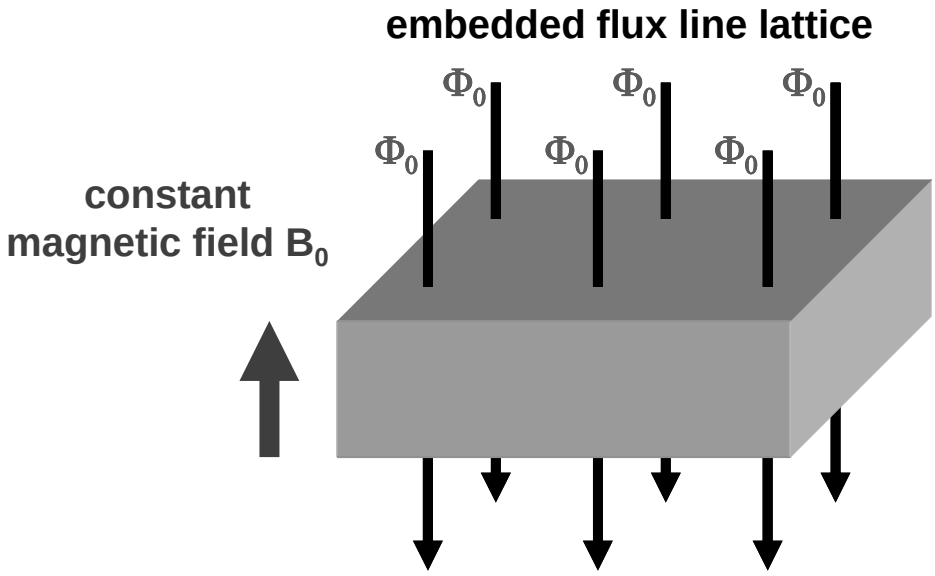

Fig. 2: *Using an embedded flux line lattice to compensate the magnetic flux from a background magnetic field B_0.*

Let us now consider a periodic lattice of parallel magnetic flux lines, as shown in Fig. 2. As for a single flux line, also this flux line lattice will remain experimentally undetectable, as long as each flux line contains one magnetic flux quantum Φ_0. By adjusting the spacing between the flux lines we can now compensate the average magnetic flux from a constant background field B_0. The resulting vector potential A_p is now periodic and relates to the original potential A generated by the background field B_0 through a singular gauge transformation. A_p is also directly related to solutions that have been obtained in the context of the ideal Abrikosov vortex lattice in type-II superconductors.

At this point, we have two periodicities in our system, one generated by the crystal lattice, and one by the flux line lattice. In order to be able to apply Bloch's theorem, we need that the periodicities become commensurable so that a magnetic superlattice forms. This is exactly then the case if we have a so-called rational magnetic field: There the magnetic flux from B_0 through the faces of the unit cell of the crystal lattice is a rational multiple of the magnetic flux quantum Φ_0, a condition that is already well known from the theory of magnetic translation groups. Incidentally, one can actually show that the singular gauge factor derived in this work is also an eigenfunction of the magnetic translation operator for primitive translations of the flux line lattice.

The results that have been obtained in this study can be easily extended to systems with spin, since the singular gauge factor used here commutes with the Pauli matrices. An extension to many-body systems is also possible; however, more care is needed since the gauge factor depends on the electric charge of each particle. Here we find that we need charge quantization (which is obviously given in electronic systems) in order to get a consistent many-body Schrödinger equation.

[1] D. R. Hofstadter, Phys. Rev. B **14**, 2239 (1976).
[2] C. Albrecht et al., Phys. Rev. Lett. **86**, 147 (2001).
[3] M. Graf and P. Vogl, Phys. Rev. B **51**, 4940 (1995).
[4] A. Trellakis, Phys. Rev. Lett. **91**, 056405 (2003).

Supported by the Office of Naval Research and by Deutsche Forschungsgemeinschaft

Experimental demonstration of a sharp quantum Hall edge

Michael Huber, Matthew Grayson[1], Dieter Schuh, Max Bichler, and Gerhard Abstreiter

Experimental studies of quantum Hall (QH) edges are essential to test our understanding of the QH effect. The internal structure of these edges strongly depends on the sharpness of the edge potential: for example in the soft edge potentials typical of etched or gated samples, the quantum Hall edge breaks up into wide compressible (metallic) and incompressible (insulating) strips, with additional edge reconstructions predicted at the compressible strip edges. The experimental realization of a sharp edge is much more difficult to achieve, but heterojunction barriers in cleaved-edge overgrown structures should approach this limit. The experimental proof of the sharp limit however was missing up to now. A non-planar sample geometry invented in the WSI for the momentum resolved spectroscopy of quantum Hall edges could now close this gap and deliver the first direct proof of a sharp quantum Hall edge.

The T-shaped tunnel geometry consists of two orthogonal GaAs quantum wells ($QW^{\perp}$ and $QW^{\parallel}$) that are separated by an $Al_{0.3}Ga_{0.7}As$ tunnel barrier (Fig. 1, right inset). A magnetic field B perpendicular to $QW^{\perp}$ identifies this as the quantum Hall effect system under study, while $QW^{\parallel}$ acts as the probe contact which is not affected by B. The tunnel barrier itself forms the confining edge potential for the QH system. As shown in the annual report of 2002, tunneling in this structure is characterized by the conservation of momentum k_y in y-direction.

This momentum conservation allows us to directly probe the real space positions of individual edge channels. Figure 1 shows the differential tunnel conductance dI/dV while sweeping the B-field, with four maxima in-dexed n = 0,1,2,3. By scaling k_y with the square of the magnetic length $l_0^2 = \hbar/eB$, the tunneling selection rules of momentum conservation can be related to the conservation of the orbit center coordinate $X = l_0^2 k_y$ in x-direction. Therefore when we convert our known Fermi momentum $k_F = 1.2 \cdot 10^8$ m^{-1} into an orbit center coordinate,

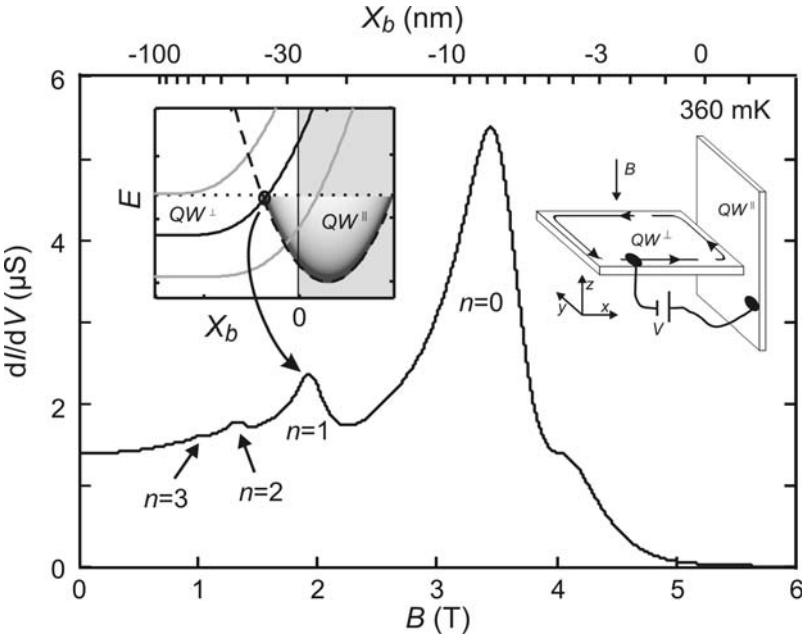

Fig. 1: *Differential conductance dI/dV as function of magnetic field B. Peaks corresponds to the Fermi point $FP^{\parallel}$ probing individual QH edge channels (n = 0, 1, 2, 3) at the orbit center coordinate X_b.* ***Right inset:*** *The QH system in $QW^{\perp}$ together with the probe contact $QW^{\parallel}$ forming the T-shaped tunnel geometry.* ***Left inset:*** *Schematic dispersion curves of the energy E vs. orbit center coordinate X in both tunnel contacts under the resonance condition for n = 1.*

[1]phone:+49-89-289-12778, fax:+49-89-3206620, email: matthew.grayson@wsi.tum.de

$X_F = \hbar k_F/eB$, we can plot the real-space distance of this tunneling point as a function of B relative to the sharp edge: $X_b = |X_F| - b - w/2$ (see Fig. 1 top axis) where $(b+w/2)$ is the distance from the sharp barrier wall to the center of $QW^{||}$. Whenever X_F, the real space position of the Fermi point $FP^{||}$ in the probe contact, coincides with the coordinate X of one of the edge channels a conductance peak occurs.

n	0	1	2	3
B (T)	3.44	1.9	1.33	1.02
ν	2.3	4.1	5.9	7.7
l_0 (nm)	14	19	22	25
$X_{b,min}$ (nm)	0	13	27	42
X_b (nm)	8 ± 2	26 ± 3	44 ± 5	62 ± 6

Tab. 1: *The measured orbit center position X_b is within a magnetic length l_0 of the theoretical sharp edge limit $X_{b.min}$.*

The edge channel positions X_b quantify the sharpness of the quantum Hall edge. Table 1 compares the position of the four outermost edge channels X_b with the theoretical sharp edge limit $X_{b,min}$. The small difference of the model from the experimental value is consistent with a slight band bending towards the edge of $QW^{\perp}$ which arises from the detailed electrostatics of this non-planar tunnel geometry. Nevertheless the measured distance X_b is always within l_0 of this sharp edge limit $X_{b,min}$ and the length scale between edge channels is found to be of order or smaller than both the magnetic length l_0 and the Bohr radius $a_0 = 10$ nm in GaAs. As a consequence, the formation of compressible strips or QH edge reconstruction standard for soft edges *does not occur here* since the electrostatic screening central to these models must take place on length scales larger than a_0 and l_0, respectively. This quantified observation of a sharp edge limit is the principle result of this work.

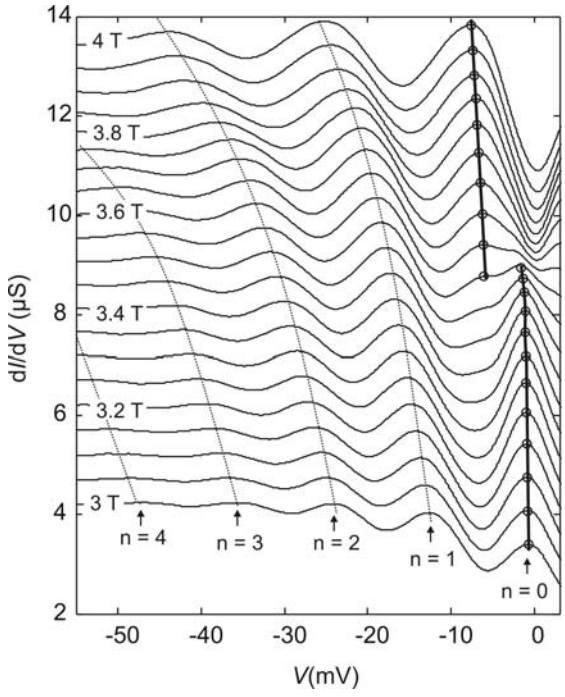

Fig. 2: *Differential conductance dI/dV as function of the tunnel bias V for different magnetic fields near a bulk filling factor n = 2 at B~3.5 T. The sharp edge condition makes the jump in the chemical potential in the bulk detectable also at the edge (see line for n = 0).*

We have also demonstrated the absence of screening in such a sharp QH edge. The maxima in the conductance data of Fig. 2 follow the dispersion of the edge states for the individual Landau levels n. When the bulk filling factor crosses $\nu = 2$ at $B \approx 3.5$ T the chemical potential in the bulk jumps as the Fermi energy traverses the Landau gap between the two lowest Landau levels. This potential jump is observable at a sharp edge: at $B \approx 3.5$ T the dispersion curve of the lowest level $n = 0$ shows a step $\Delta V \approx 6$ mV that is close to the expected jump of the chemical potential for a cyclotron energy $\hbar\omega_c = 6$ meV. This proves that the potential jump in the bulk is *not screened* in our sharp edge, as it would be in a smooth edge. The smooth edge case on the other hand (for depleted edges $n = 1$, 2, 3, or 4) has wide compressible (metallic) strips that screen this potential jump.

supported by DFG (Schwerpunktprogramm Quanten-Hall-Systeme)
in collaboration with W. Biberacher, Walther-Meissner-Institut, Garching (Germany)

Quantum Hall effect in a bent quantum well: Anomalous edge state reflection

Matthew Grayson[1], Michael Huber, Dieter Schuh, Max Bichler, and Gerhard Abstreiter

Using a recently developed crystal growth technique [1] (see Fig. 1) we have succeeded in creating a two-dimensional (2D) electron system that is bent at an atomically sharp angle of 90°. In a tilted magnetic field, we induce quantum Hall edge channels which overlap at the corner junction, and observe anomalous reflection coefficients which appear to measure the Landau orbital index of both electrons and, remarkably, *composite fermions*.

The quantum confinement structure consists of a high-mobility GaAs/AlGaAs heterostructure overgrown on a precleaved corner. This bent quantum-well heterostructure (BQW) exhibits high mobility with fractional quantum Hall effect (QHE) signatures on both facets, allowing new geometries for integer and fractional QHE edge experiments to be realized. Naming the two 2D systems after their substrate (*S*) and precleave (*P*) facets, we measure their densities n_s = 1.07×10^{11} cm^{-2} and n_p = 1.30×10^{11} cm^{-2}. In the presence of a tilted magnetic field, this system realizes an abrupt junction between two quantum Hall effect (QH) systems with differing filling factors:

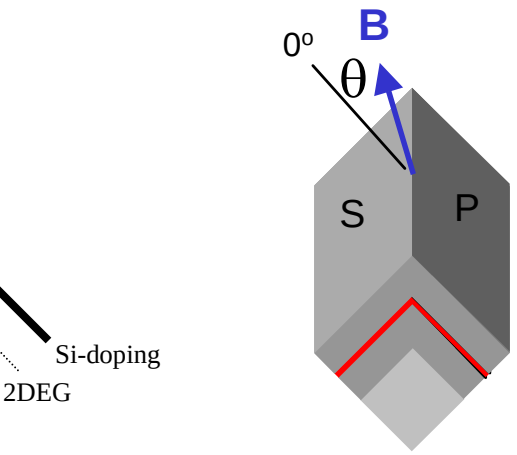

Fig.1:
Schematic of device in tilted magnetic field at angle and θ. Substrate and precleave facets are labeled 'S' and 'P' respectively. The 2D electron system on the overgrown corner is bent by 90 degrees.

$$\nu_s = hn_s / eB\cos\theta$$
$$\nu_p = hn_p / eB\sin\theta.$$

This bent quantum well geometry enables for the first time equilibration between co- or counter-propagating QH edge states in the same sample, depending on the tilt angle of the magnetic field. In particular, this system is the first experimental realization of an abrupt QH junction, which is proposed to manifest Andreev reflection of quasiparticles [2,3] or identically function as a DC step-up transformer [4].

At the angle where the two filling factors are equal, an unexpected behavior arises (see Fig. 2). Whereas within each separate 2D system the R_{xx} minima go to zero as expected (dotted and dashed lines), the minima of R_{xx} for a current sent *across the corner* do NOT all go to zero (solid line), implying a finite back reflection *r* of the edge channels at these filling factors. This finite reflection must be induced by the corner geometry since in a co-planar system of uniform filling factor the reflection coefficient would be identically zero for all quantum Hall states.

The most intriguing aspect of the behavior is the dependence on Landau index, *N*. By inspection, one sees that at $\nu = 1$ and 2 (both $N = 0$) the reflection coefficient is zero, whereas for all other filling factors ($N \geq 1$) it is finite. At fractional filling factor $\nu = 2/3$, one sees again a finite reflection. This suggests that the composite fermion Landau index N^*

[1]phone:+49-89-289-12756, fax:+49-89-320-6620, email: grayson@wsi.tum.de

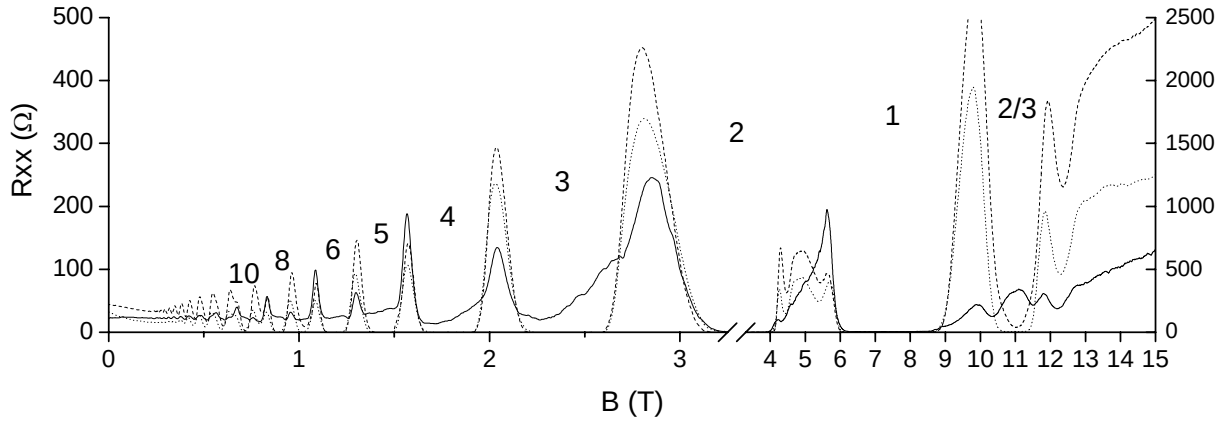

Fig.2:
Longitudinal resistance R_{xx} for the 'S' (dotted) and 'P' (dashed) facets along with the longitudinal resistance across the corner junction (solid line). The R_{xx} minima are labelled with the filling factor index. The R_{xx} minima measured within each facet go to zero for filling factors $\nu_S = \nu_P = 2/3, 1\ldots10$ demonstrating good QHE. However the R_{xx} minima for conduction across the corner shows distinct non-zero minima for $\nu_S = \nu_P = 2/3$, and $3\ldots10$.

associated with the 2/3 partially filled lowest Landau level ($N = 0$) is $N^* \geq 1$, a surprising result that is nonetheless anticipated by composite Fermion theory. By comparing $r = r(N)$ from the integer QH states with $r = r(N^*)$ from the fractional QH states, one can learn about the Landau orbitals of the other composite fermions fractions. However, the two tilted facets require a field of 22 T to reach filling factors down to 2/5 and 1/3 (see Fig. 2). This experiment will therefore be conducted in a tilting stage at the Grenoble High Magnetic Field Labs in a 22 T dilution refrigerator.

We also report a related novel structure that has been successfully fabricated at the WSI which we call a 2D-2D corner tunneling device. This device is similar to the bent quantum well, except instead of triangular confinement, the electrons are ...ed in 200 Å GaAs quantum wells, and instead of an open junction at the corner, a 128 Å $Al_{0.3}Ga_{0.7}As$ barrier separates the two systems as shown in the schematic of Fig. 3. In a tilted *B*-field, this structure should allow tunneling spectroscopy between quantum Hall edge states of arbitrary filling factor.

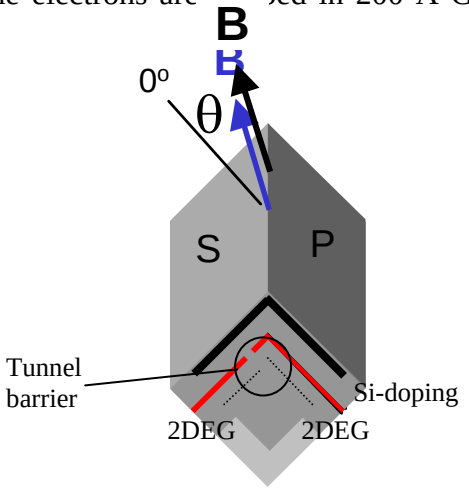

Fig.3:
Schematic of new 2D-2D corner tunneling device which has been successfully fabricated.

[1] Matthew Grayson, et al., WSI Jahresbericht 2002.
[2] I. Safi, and H. J. Schulz, Phys. Rev. B 52, R17 040 (1995)
[3] N. P. Sandler, C. de C. Chamon, and E. Fradkin, Phys. Rev. B 57, 12324 (1998)
[4] D. B. Chklovskii, and B. I . Halperin, Phys. Rev. B 57, 3681 (1998)

supported by DFG (Quanten-Hall Schwerpunkt)

Long relaxation times of holes in Si/SiGe quantum cascade structures with diagonal intersubband transitions

Ingo Bormann, Karl Brunner, Hubert. Riedl, Stefan Hackenbuchner, and Gerhard Abstreiter[1]

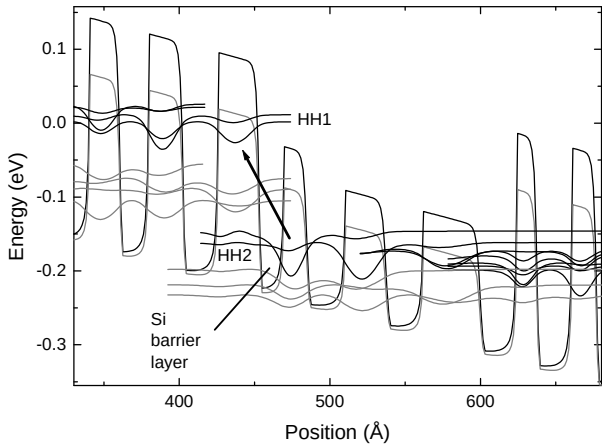

Fig.1: *Calculated band structure of the cascade. Shown are valence band edges and states for heavy (black) and light holes (gray) with an applied electric field of 55kV/cm. The arrow indicates the radiative transition.*

Intersubband lasers like quantum cascade (QC) lasers in principle offer the possibility to realize a semiconductor laser based on silicon germanium technology. The indirect band gap of silicon, which prohibits building diode lasers with silicon, is irrelevant in the intersubband scheme. The band offset of SiGe structures grown pseudomorphically on silicon is mainly in the valence band. This makes it necessary to implement the cascade scheme in the valence band using hole subbands. Up to now electroluminescence (EL) of various such structures has been shown. Neither optical gain nor stimulated emission has been demonstrated with such structures so far and it is not clear how the required population inversion can be achieved. The dominant scattering mechanism in SiGe, deformation potential scattering with optical phonons, determines the nonradiative hole lifetimes. This results in very short lifetimes (<1ps) and monotonically increasing scattering rates with increasing subband energy spacing, if it is larger than the optical phonon energy. In order to achieve population inversion it is desirable to enhance these lifetimes. One way to suppress nonradiative scattering is the reduction of the wave function overlap of the two states involved. In this work we explore the possibility to achieve long upper state hole lifetimes by using diagonal transitions between ground states of neighboring quantum wells.

The band structure of the samples used in this study is depicted in Fig. 1. It is a simple Si/SiGe quantum cascade structure similar to the ones previously investigated. Holes are injected into the HH2 state by tunneling from the heavy hole miniband on the right hand side. After relaxation down into the HH1 state (diagonal arrow in Fig. 1) by emission of phonons or a photon, they are extracted by the second miniband on the left. The wave function overlap of the HH1 and HH2 state can be changed by varying the thickness of the Si barrier. We have fabricated samples with 15 Å, 25 Å and 35 Å Si barriers. For comparison in one sample the

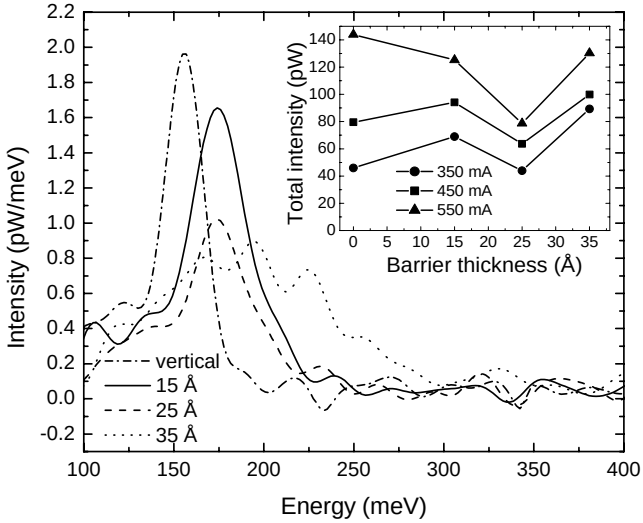

Fig. 2*: EL spectra of the diagonal and vertical transition SiGe QC structures at 50 K and 450 mA pump current. Inset: spectrally integrated EL intensities from the four structures at different driving currents.*

[1]phone:+49-89-289-12771, fax:+49-89-3206620, email: abstreiter@wsi.tum.de

diagonal transition is replaced by a vertical transition between the first two heavy hole states of a single SiGe quantum well with a Ge content of 0.39.

The structures have been grown in a Riber molecular beam epitaxy machine. We find EL emission centered at 155 meV (vertical), 174 meV (15 Å), 174 meV (25 Å) and 185 meV (35 Å), as shown in Fig.2. The spectrally integrated intensity of the four samples is plotted in the inset of Fig. 2. From the total EL intensity we have deduced experimental lifetimes as follows: after solving simple rate equations the factors that determine the EL intensity are the squared optical matrix element and the upper state lifetime t_2. Thus the intensity is given by $I=c|\langle i|p_z|j\rangle|^2 \cdot t_2$ (1). $|i\rangle$ and $|j\rangle$ denote the initial and final hole states and p_z is the momentum operator in z-direction. The constant c is unknown, as it is influenced by our experimental setup, but it should be the same for all samples. In order to interpret the results we have performed 6-band k·p model calculations for the band structure, which includes Ge-segregation effects. From this band structure we have calculated the squared optical matrix elements $|\langle i|pz|j\rangle|2$ plotted in Fig. 3.

We have also calculated nonradiative scattering rates using the hole phonon matrix element $\langle i|D\cdot u|j\rangle$. Here D is the deformation potential tensor. The results are also given in Fig. 3. There are two different scattering channels, direct scattering from the HH2 state into the HH1 state and scattering from the HH2 state to intermediate light hole states, which are present between the two HH states (see Fig. 1). By summing up the two individual channels, we obtain a total upper state (HH2) lifetime. As expected, we see a strong increase of the lifetimes, wich are derived only from the bandstructure, from 0.4 ps for the vertical transition to 23 ps in the case of the 35 Å Si barrier.

We have deduced experimental scattering times from (1) using the calculated optical matrix elements. In order to enable a comparison with nonradiative lifetimes derived by deformation potential scattering calculations, we have set the lifetimes obtained by the two methods equal for the 15 Å barrier sample. This fixes the factor c to a constant value. Experimental lifetimes also show a strong increase from 0.7 ps for the vertical transition to 12 ps for the 35 Å barrier sample.

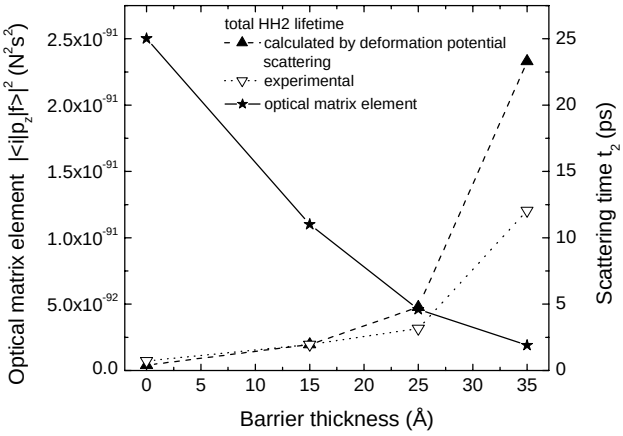

***Fig. 3**: Nonradiative lifetimes t_2 of the HH2 state calculated from the k·p model using the hole phonon matrix element and experimental lifetimes, as obtained from the integrated intensity and the optical matrix element. The stars show the corresponding calculated optical matrix element. At barrier thickness zero the values for the vertical transition are plotted.*

The results are shown in Fig. 3. Lifetimes obtained by both methods are in reasonable agreement and show a strong increase for wider Si barriers. Calculated values increase by a factor of 57 and experimental values by a factor of 17. The fact that the deformation potential calculations predict an even stronger increase for the lifetimes than experimentally observed may be due to the fact that scattering by interface roughness and hole-hole scattering is neglected in such calculations .

These findings demonstrate that it is possible to enhance the upper state lifetime by using diagonal transitions and suggest, that with a similar design population inversion between heavy hole states in a Si/SiGe quantum cascade structure can be achieved but at the cost of smaller optical matrix elements.

---

supported by: DFG (Ab35/3-2) and (Br1960/1-3)
in collaboration with S. Schmult, and W. Wegscheider, University of Regensburg

Efficient method for the calculation of ballistic quantum transport

Denis Mamaluy, Matthias Sabathil[1], and Peter Vogl

We have developed a novel and extremely efficient method [1] to calculate the ballistic transmission function and current of an arbitrarily shaped, multi-terminal two- or three-dimensional open device. This method allows for the calculation of all properties of interest such as the spectral function, the carrier density or the transmission of an open device in the ballistic regime.

The successful realization of semiconductor nanostructures such as quantum dots, electron waveguide structures, or nanoscale metal oxide semiconductor field effect transistors (MOSFET's) calls for reliable and accurate theoretical tools to predict their charge carrier transport. Quantum effects play a dominant role in some of these small size structures. Commonly used schemes to calculate the quantum transport in nanostructures are the Wigner-function approach, the non-equilibrium Green's functions, Pauli master equation, and particularly the Landauer-Buttiker formalism. The Landauer approach assumes the transport to be strictly ballistic within the nanostructure and is based on the solution of the Schrödinger equation with scattering boundary conditions. While this is a significant simplification compared to a calculation that includes the relaxation of carriers, even this approach becomes computationally very challenging for higher dimensional nanostructures with a complex geometry.

There are several existing methods to calculate the ballistic transport in quantum devices but most of them are either computationally inefficient since they scale like N^3 where N is the total number of grid points, or they are restricted to devices with two ohmic contacts only. We have developed a novel and efficient method to calculate the ballistic transmission function of a two- or three-dimensional device that may have any shape, potential profile, and number of leads. In this method, that we term contact block reduction (CBR) method, the transmission function of the open system can be obtained from the eigenstates of a corresponding closed system that need to be calculated only once and the solution of a very small linear algebraic system for each energy grid point. Importantly, we show that the calculation of relatively few eigenstates of the closed system suffices to obtain accurate results.

To exemplify the CBR method we study tunnelling through buried quantum dots [2]. We calculated the transmission through a model quantum dot resonant tunnelling structure depicted in Fig. 1. There is a cuboidal dot of 14 nm lateral diameter and 5 nm thickness embedded within a 15 nm thick barrier region. For the calculation we used a one-band Hamiltonian with an electron mass of 0.067 [m_0] and barrier heights of 0.4 eV. The potential has been set to zero in the leads and to -0.2 eV within the dot. The total size of the device region is 40×40×20 nm. With a grid spacing of 1 nm, this leads to a matrix size of 35000 for the Hamiltonian. To check the convergence

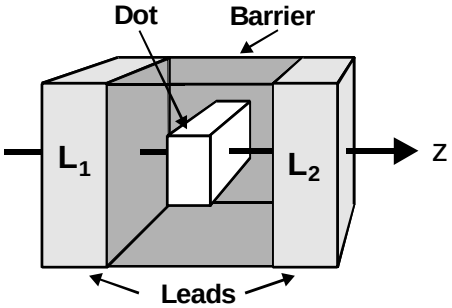

Fig. 1*: Model dot structure with outer dimensions of 40×40×20 nm with two semi-infinite leads and the interior containing a tunneling barrier region and a cuboidal quantum dot.*

[1]phone:+49-89-289-12762, fax:+49-89-289-12737, email: sabathil@wsi.tum.de

with respect to the number of eigenstates included we have calculated the transmission function for zero applied bias including 200, 400 and 600 eigenstates, respectively (Fig. 2).

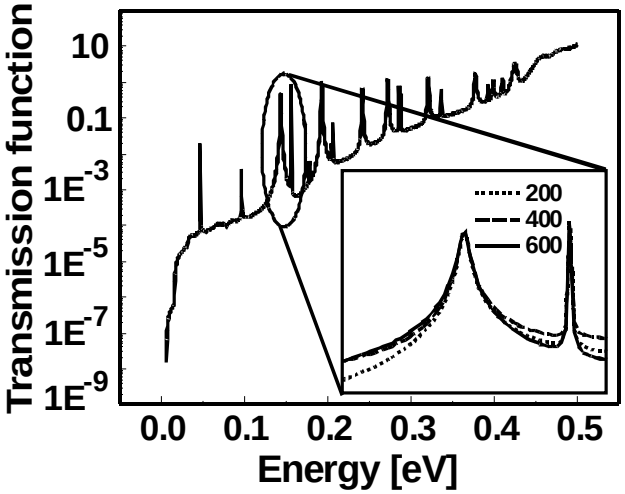

***Fig. 2**: Transmission function versus energy in eV for the structure depicted in Fig. 1. The inset shows the result when 200, 400, or 600 eigenstates are included in the transmission.*

The inset in Fig. 2 shows that the peak values of the transmission are well converged already with very few eigenstates, whereas the non-resonant part of $T(E)$ converges rather slowly. Indeed, only a single resonant eigenstate contributes to the transmission close to the corresponding pole in the Green's function whereas all eigenstates contribute otherwise, with a weight that is inversely proportional to the energy. Fortunately, the current is dominated by the peak values of $T(E)$ so that the *I-V* characteristics are insensitive to the number of eigenvalues included. The limiting factor in our calculations is the storage rather then the computer time for the diagonalization of the sparse Hamilton matrix. In Fig. 3, we show the calculated ballistic current, where we assumed a Fermi level of 60 meV and zero temperature in each lead. We note that the chosen total lateral size of the device in Fig. 1 (40 nm) is sufficiently large so that it does not influence the transmission and the current through the dot. We checked this explicitly by repeating the calculation for a 60 nm wide device.

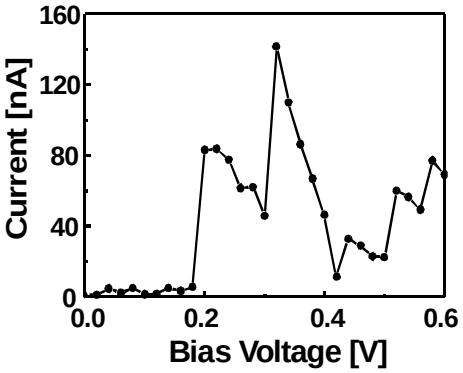

***Fig. 3**: The ballistic current through the model quantum dot structure shown in Fig. 1, assuming a Fermi level of 60 meV in each lead and zero temperature.*

This example shows that due to the efficiency of the CBR method it is now possible to calculate the current through a realistic three-dimensional device without making any simplifications such as assuming rotational symmetry. We see that the current is already converged for as few as one hundreds of all eigenstates which leads to a reduction in the computational effort of roughly a factor of 10000 compared to standard methods. Thus combining the CBR method with the device simulator next**nano**^{3} [3] we are now able to calculate the quantum transport properties of large 3D devices with a realistic band-structure that takes into account effects such as strain, band-bending and piezoelectric charges.

[1] D. Mamaluy, M. Sabathil, and P. Vogl, J. Appl. Phys. **93**, 4628 (2003)
[2] M. Sabathil, S. Birner, D. Mamaluy, and P. Vogl, J. Comput. Electronics **2**, 269, (2003)
[3] S. Hackenbuchner, *et al*. Physica B **314**, 145 (2002)

supported by the Deutsche Forschungsgemeinschaft (DFG) and the Office of Naval Research (ONR) Contract No. N00014-01-1-0242

Growth of two-dimensional high mobility hole gases on (110) oriented GaAs using Si as a dopant

Frank Fischer[1], Matthew Grayson, Dieter Schuh, Max Bichler, Karl Neumaier[2], and Gerhard Abstreiter

We report the *first growth* of a high mobility two-dimensional hole gas (2DHG) in a modulation-doped heterostructure on the (110) GaAs surface using Si as a dopant. This new technique invented at the WSI opens new device possibilities for standard III-V growth chambers since both *p*- and *n*-type high mobility layers can now be grown *on the same substrate* using the *same standard dopant* (Si) as both acceptor and donor, respectively.

	[001]	[110]	[111]
HH	$0.35m_e$	$0.65m_e$	$0.8m_e$
LH	$0.09m_e$	$0.080m_e$	$0.077m_e$
SO	$0.165m_e$		

***Tab. 1**: Effective masses of heavy holes (HH), light holes (LH) and the split-off band (SO) for different crystal orientations in bulk GaAs (Ref. 4)*

In contrast to conduction band electrons, the hole bands in bulk GaAs crystals are more complicated due to the existence of heavy holes (HH), light holes (LH) and a split-off band (SO). The HH mass is up to a factor of 12 larger than the GaAs electron mass of $m^* = 0.067\ m_e$, and the effective masses of the HH and LH's are highly anisotropic (see Table 1). This results in a smaller Landau-level separation $\hbar eB/m^*$ and mobility anisotropies, respectively. In two dimensional hole systems, the transport properties are governed by HH's because quantum confinement lifts the degeneracy of HH and LH at the Γ-point. Heavy mass systems are of increasing interest because dilute systems are more susceptible to carrier-carrier interactions, and the effective interparticle distance r_s (in units of the Bohr radius) is proportional to the mass: $r_s \propto n^{-1/2}/a_B \propto m^*$. Thus for a given density *n*, the heavier the mass is, the more relevant the carrier-carrier interactions are. Evidence for Wigner crystallisation and metal insulator transition has been reported in recent years [1, 2].

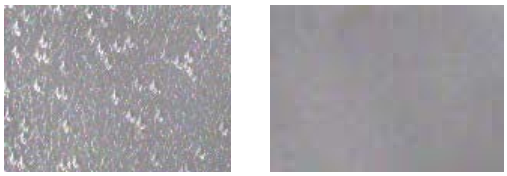

***Fig. 1:** Microscope picture of*
a) surface of a thick p-type layer (left)
b) surface of the 2DHG sample (right)

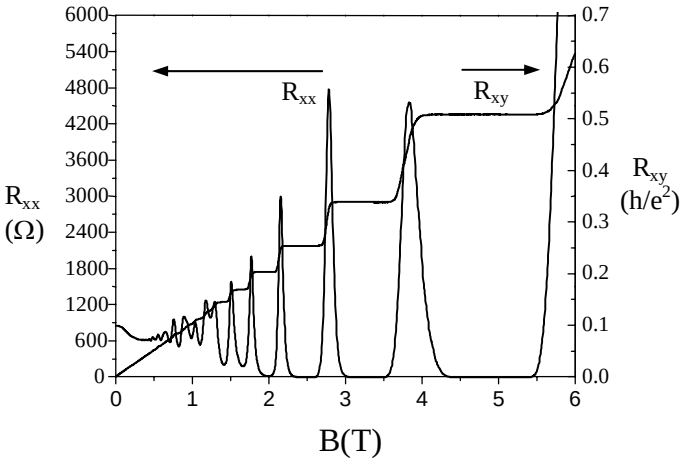

***Fig 2**: Longitudinal and quantum Hall resistance data of 2D holes in (110) GaAs taken at 30mK.*

Previously 2DHGs have been grown either on (001) GaAs substrates using Be or C as an acceptor or on (311)A substrates using Si dopants. The highest mobilities were achieved on (311)A substrates. In contrast to (311)A, Si acts as a donor on the (110) GaAs surface at typical growth conditions. However by increasing the substrate temperature from 490°C to 640°C and lowering the As pressures (beam fluxes) by a factor

[1]phone:+49-89-, fax:+49-89-289-12756, email: frank.fischer@wsi.tum.de
[2]Walther-Meissner-Institut für Tieftemperaturforschung

of about 4, Si acts as an acceptor [3]. We reached a bulk hole concentration up to p = 2 x 10^{18} cm^{-3} under these conditions, a good basis for trying modulation doped heterostructures on (110) GaAs. Unfortunately, growing a thick *p*-doped layer under such conditions, resulted in a very rough surface (Fig 1a). To improve the quality of the interface and surface (Fig. 1b) we used the high substrate temperature and low As pressure *only* during growth of the small, 20 Å thick, doping layer in $Al_{0.34}Ga_{0.66}As$ which was separated from the GaAs heterointerface by 40 nm. The rest of the sample was grown under optimal growth conditions.

This first attempt resulted in a quite high hole mobility of more than μ = 100 000 cm^2/Vs at a density of p = 2.3x10^{11} cm^{-2}. An ungated sample shows very well developed quantum-Hall plateaus and minima of the longitudinal resistance at 30 mK (Fig. 2).

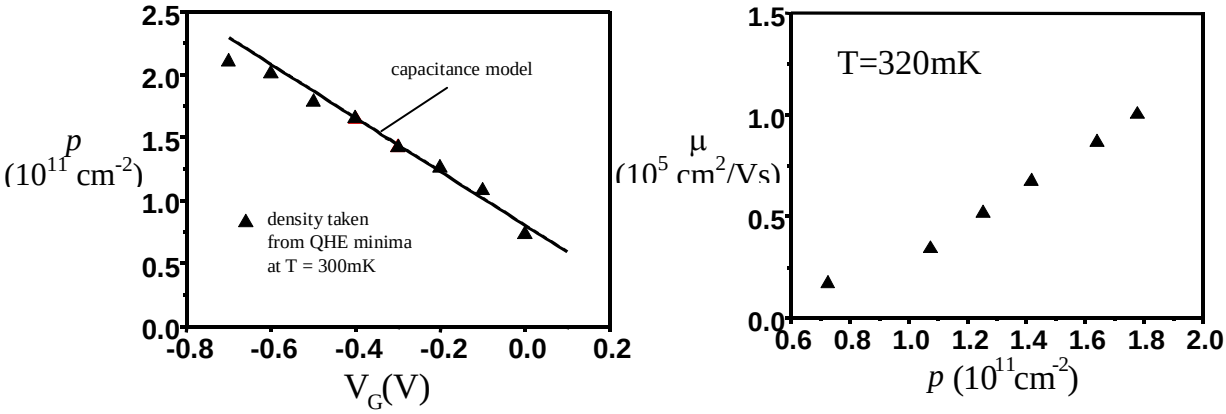

Fig. 3:
a) Comparison of the measured 2DHG density at T = 320 mK versus gate voltage with the density calculated with a capacitor model (left)
b) Mobility of the 2DHG versus density at T = 320 mK (right)

Density dependent transport parameters of our sample could be studied by evaporating an Al-gate on top of an L-shaped Hall-bar. We are able to vary the density by a factor of 4 between p = 5x10^{10} cm^{-2} up to p = 2.3x10^{11} cm^{-2} (Fig. 3a). The mobility increased up to μ = 125 000 cm^2/Vs at the highest density (Fig. 3b).

The achievement of high mobility hole gases on (110) GaAs by doping with Si opens various new possibilities for novel studies of interacting carrier systems. Since the [110] orientation is the natural cleavage plane of GaAs, it should be also possible to grow 2DHGs by cleaved edge overgrowth without introducing additional dopant sources in our high mobility MBE-machine. This enables new devices like atomically precise hole wires, and orthogonal 2D-2D tunnel-junctions for probing the quantum Hall edges of a 2DHG, analogous to previous studies in electron systems [5].

[1] For a review see: M. Shayegan, *Perspectives in Quantum Hall Effects*, **343** (1997)
[2] S.J. Papadakis et al., Phys. Rev. Lett. **84**, 5592 (2000)
[3] E.S. Tok et al., J. Appl. Phys. **61**, 1652 (1992)
[4] Sadao Adachi, *GaAs and Related Materials*, World Scientific (1994)
[5] Michael Huber et al., WSI Jahresbericht 2002, 2003

supported by DFG Schwerpunktprogramm Quanten-Hall Systeme

Silicon doping of AlN films grown by molecular beam epitaxy

Martin Hermann[1], Florian Furtmayr, Martin Stutzmann, and Martin Eickhoff

Silicon is the standard dopant to achieve n-type conductivity in group III-nitrides. However, whereas Si forms a shallow donor state in GaN (25 - 30 meV ionization energy), increasing of the Al content in $Al_XGa_{1-X}N$ results in a steep increase of the ionization energy of up to 320 meV for Si in AlN. In addition, unintentionally incorporated oxygen is believed to form a deep defect state. The interaction of both kinds of impurities and the related mechanisms of self compensation are not yet fully understood, and Si-doped AlN films with a reasonable room temperature conductivity have been difficult to obtain. One approach to overcome these difficulties is the increase of the concentration of incorporated Si-atoms above the critical density for impurity band formation, which can be estimated to occur for a Si concentration of approximately 1 at %. However, problems due to a limited solubility of the impurities as well as self compensation of the donor are likely to appear at such high concentrations.

To clarify these issues, we have made a systematic study of Si-doped AlN grown with plasma assisted molecular beam epitaxy. The AlN layers were grown on c-plane sapphire under variation of the Si-flux. We have studied both slightly Al-rich and N-rich growth conditions. The influence of the growth condition on the incorporation as well as the depth distribution of Si was measured by elastic recoil detection analysis (ERDA). For a substrate temperature of 860 °C, we found a large influence of the III/V ratio on the Si incorporation: Whereas growth under Al-rich conditions leads to Si-accumulation in the near-surface region, slightly N-rich growth results in a homogeneous Si incorporation with densities up to 5×10^{21} cm^{-3}, which is well above the expected concentration for a Mott transistion (c.f. Fig. 1).

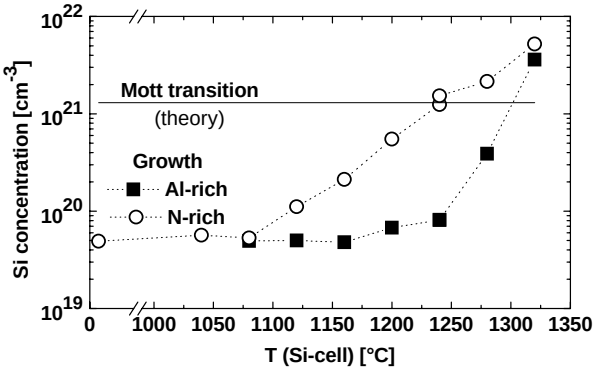

Fig. 1: *Si concentration versus Si cell temperature. For N-rich growth conditons a pronounced increase of the incorporated Si is observed.*

The structural properties of the doped AlN layers were investigated by high resolution X-ray diffraction and atomic force microscopy. We did not observe an influence of the concentration of incorporated Si on the surface morphology and the structural quality. The latter is characterized by a full width at half maximum of the rocking curve below 200 arcsec, measured at the (00.2)-peak up to Si-concentrations of 5×10^{21} cm^{-3}. Reciprocal space mapping of the (20.5)-peak showed an increase of tensile stress with increasing Si-concentration for layers grown in the N-rich regime, indicated by a decrease of the in plane lattice constant a and a corresponding increase of the c lattice constant (c.f. Fig. 2).

Temperature dependent conductivity measurements revealed a decrease of the activation energy with increasing Si concentration to less than 20 meV for a Si content of mor than $2\cdot10^{21}$ cm^{-3} (c.f. Fig. 3). In this case, the charge carrier density was $3.7\cdot10^{18}$ cm^{-3}

[1]phone:+49-89-289-12755, fax:+49-89-289-12737, email: hermann@wsi.tum.de

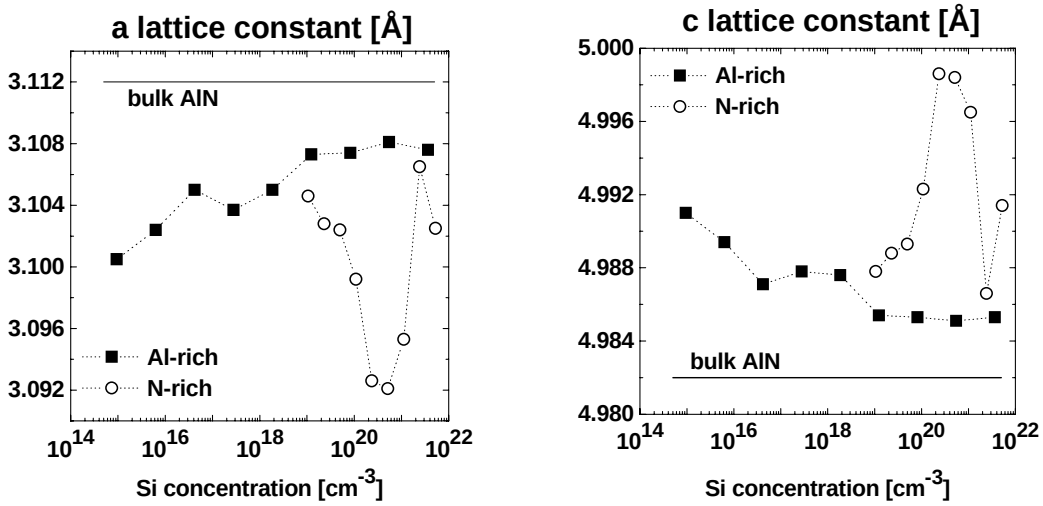

Fig. 2: *Variation of the a (in plane) and c lattice constants with increasing Si concentration. The change of the lattice constants can be attributed to the different growth conditions. Also indicated are the bulk AlN lattice constants.*

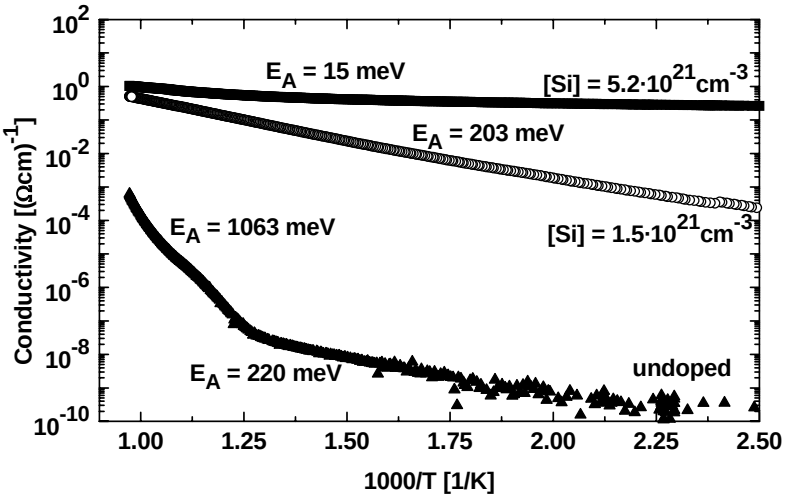

Fig. 3: *Temperature dependence of the conductivity. With increasing Si content the conductivity at 300 K increases by more than 8 orders of magnitude.*

at room temperature, resulting in a conductivity of 0.2 $(\Omega cm)^{-1}$. The Hall mobility was about 1 cm^2/Vs, also indicating the formation of an impurity band. For nominally undoped AlN a second thermally activated state with an activation energy of about 1 eV was observed. Further investigations are in progress to determine the nature of the second state.

supported by DFG (EI 518 / 1-1)

Cleaved-edge overgrown aluminum arsenide quantum wires

J. Moser, M. Grayson, F. Ertl, D. Schuh, M. Bichler, and G. Abstreiter

Cleaved-edge overgrowth (CEO) is a well-established technology that has been extensively employed in the fabrication of GaAs quantum wires [1-4]. In these systems the sharp confining potential originating from an atomically smooth interface has opened new avenues in physics where many-body interactions have been proven to play a crucial role [2,3]. To improve our understanding of those low-dimensional, strongly interacting systems, CEO wires can be fabricated in heavy mass materials like aluminum arsenide whose electron-electron interactions are stronger than in GaAs at a given density. Moreover, the band structure makes AlAs a multi-valley compound: the valley index offers an extra quantum number that can be treated as an isospin, which may give rise to additional features. Using AlAs 2DEG's with mobility ~70,000 cm^2/Vs at density ~3E11 cm^{-2}, we have fabricated AlAs CEO quantum wires and measured narrow conductance steps upon sweeping a top gate bias, using both a helium 3 and a dilution refrigerator. The tight confinement allows us to resolve closely separated 1D subbands against a background of weak conductance fluctuations. The most noticeable steps are found to lie close to 0.4, 0.8 and 1.2 e^2/h at zero magnetic field (see fig. 1) and are reproducibly observed in separate devices. However their heights fall much below the values of 4, 8 and 12 e^2/h anticipated for the spin- and valley-degenerate 1D sub-bands of a ballistic wire. Owing to the large effective mass and our present lithographic wire length (1 μm compared with ~250 nm mean free path at 350 mK), we not only expect significant backscattering within the wire, we also understand that the 2D reservoirs couple to the wire in a non-adiabatic manner due to large Fermi momentum mismatch between the 1D and 2D systems [4]. As a result measured conductance step heights are dramatically reduced.

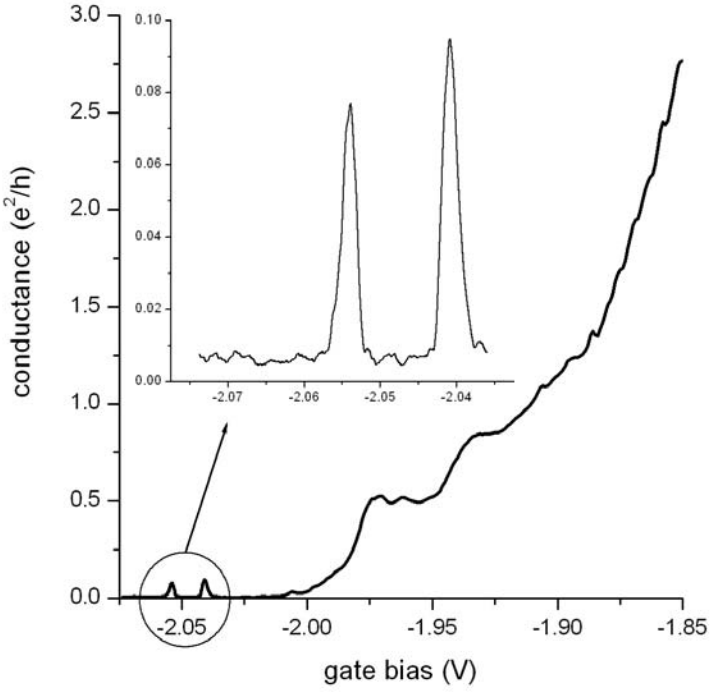

Fig. 1: *Conductance versus gate bias at a bath temperature of 20 mK. Inset: resonance peaks; note the small amplitude.*

Measurements performed at an electron temperature of 20 mK allow us to gain further insight into the 1D nature of our device. As the chemical potential of the system is lowered (by biasing a top gate electrode to deplete the electron gas underneath) eventually potential energies associated with impurities become relevant and electrons get trapped in 1D 'islands' separated by disorder-induced potential barriers. Consequently sweeping the gate

bias past the 1D pinch-off threshold reveals small, narrow conductance peaks which are resonances of localized, weakly coupled states (see fig. 1, inset). Unlike standard Coulomb blockade peaks, the area under these peaks is temperature dependent, which points towards a non-Fermi liquid scenario [5]. More can be learned by adding to the ac excitation signal a small dc bias V_{dc} between source and drain. Doing so drives the system out of equilibrium and is equivalent to a tunneling experiment across a series of isolated 1D wires whereby the differential conductance dI/dV is measured as a function of V_{dc}. Strong non-linearities are observed close to pinch-off (see fig. 2). As the gate bias is swept from the far negative side, where the conductance is strictly zero, through the resonance peaks and up to the pinch-off threshold, a well-defined, 0.5 meV wide gap develops along with two peaks on each side. Upon raising the temperature these two peaks collapse, and the gap narrows down and eventually disappears above 400 mK.

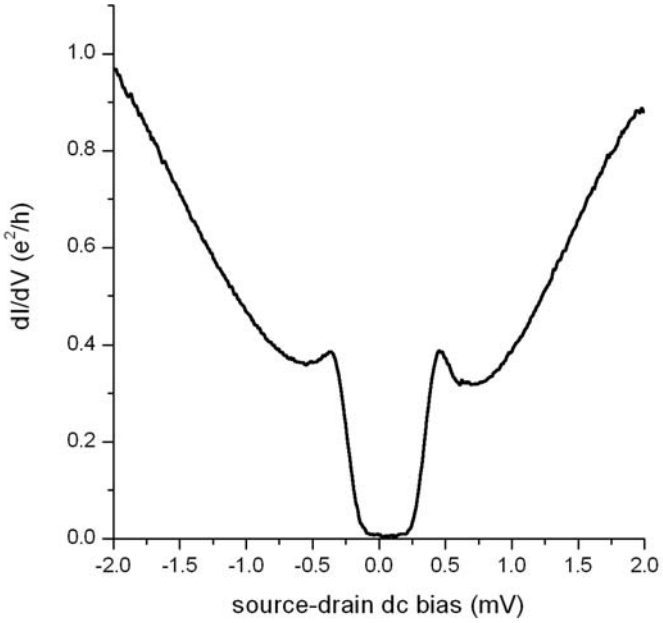

Fig. 2: *Differential conductance versus source-drain dc bias at V_g~-2V where zero-bias resonance peaks occur.*

In light of those experimental results our research is now focusing on a resonant tunneling mechanism between segments of 1D non-Fermi liquid.

[1] A. Yacoby et al., Solid State Com. **101**, 77 (1997); M. Rother, PhD Thesis, Technische Universitaet Muenchen (1999)
[2] O. M. Auslaender et al., Science **295**, 825 (2002)
[3] R. de Picciotto et al., Phys. Rev. Lett. **92**, 036805 (2004)
[4] R. de Picciotto et al., Phys. Rev. Lett. **85**, 1730 (2000)
[5] O. M. Auslaender et al., Phys. Rev. Lett. **84**, 1764 (2000)

Long-range ordered self-assembled InAs quantum dots on (110) GaAs

J. Bauer[1], D. Schuh, R. Schulz, E. Uccelli, F. Hofbauer, A. Kress, J. J. Finley, and G. Abstreiter

We demonstrate the ability to controllably position quantum dots of a well defined size on a (110)-oriented surface pre-structured with the atomic precision offered by MBE. Atomic force microscopy and spatially resolved spectroscopy confirm the long-range ordering and the excellent optical quality of these dots.

Our new approach to grow systems of aligned and well ordered quantum dots is to combine self-assembly with the cleaved-edge overgrowth (CEO) method.

In a first MBE step, a number of epitaxial layers was grown on a (001) GaAs substrate. These precise structures act as a template for quantum dot nucleation during a subsequent second MBE growth run on the cleaved (1-10) surface. For samples designed for atomic force microscopy (AFM) investigations, growth was stopped after this step whereas for photoluminescence measurements, the InAs layer was covered with 500 Å GaAs to bury the quantum dot layer.

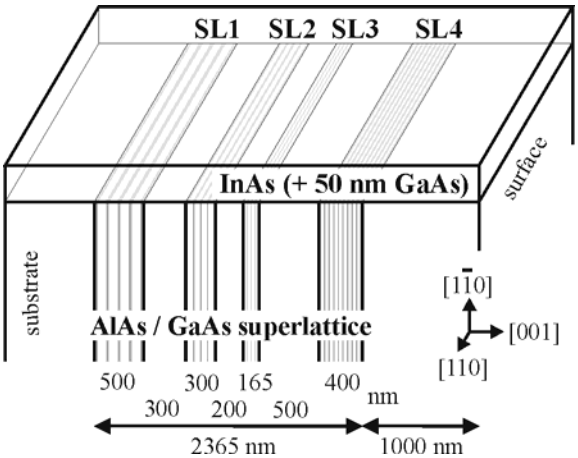

Fig. 1: *Schematic of the grown layer sequence: In the first growth step the superlattices SL1 -SL4 were grown on (001)-oriented GaAs. The InAs dot layer and a 500 Å thick capping layer were grown in a subsequent MBE run on the (1-10) GaAs surface.*

The sample investigated is depicted schematically in figure 1 and consists of 4 spatially separated AlAs/GaAs superlattices(SL1: 5 periods of 320 Å AlAs / 680 Å GaAs; SL2: 5 periods of 200 Å AlAs / 400 Å GaAs; SL3: 5 periods of 110 Å AlAs / 220 Å GaAs; SL4:10 periods of 200 Å AlAs / 200 Å GaAs) grown on semi-insulating (001) GaAs. Figure 2 shows an AFM picture of the uncapped sample. Quantum dot-like nano-structures can clearly be identified above all four superlattice regions SL1-SL4. Most surprisingly, the AFM measurements clearly indicate nucleation of quantum dot-like nanostructures along the Al-rich regions of the exposed (1-10) growth surface. Furthermore, the typical size of the quantum dots is found to directly reflect the thickness of the underlying AlAs layer; being largest for SL1 (320 Å AlAs), smallest for SL3 (110 Å AlAs) and comparable for SL2 and SL4 which share a common AlAs width (200 Å) but differ in the thickness of the surrounding GaAs and in the total number of periods. However the quantum dots grown on SL2 and SL4 appear to have larger spatial and structural inhomogeneities. We conclude, therefore, that the geometric properties of the quantum dots are sensitive not only to the thickness of the underlying AlAs layer but also the surrounding GaAs plays an important role in the dot nucleation process.

[1]phone:+49-89-289-12756, fax:+49-89-3206620, email: jochen.bauer@wsi.tum.de

In order to investigate the optical properties of the quantum dot nanostructures we performed scanning µ-photoluminescence (µ-PL) spectroscopy on a subsequently grown sample with a GaAs capping layer. The sample was mounted in a liquid He cryostat with the quantum dot layer accessible for the excitation laser beam and the microscope to collect photoluminescence. A HeNe laser, focused on the (1-10) surface of the sample was used to excite the quantum dots and a confocal excitation and collection geometry provides a maximum spatial resolution of ~1.5 µm.

Figure 3 shows a series of µ-PL spectra which differ in the excitation power.

At low excitation power, just a single emission line at 1.308 eV is observed. The linear power dependence of this feature identifies it as arising from a single exciton (X^0). In addition, this line is an emission doublet, possibly due to elongation of the quantum dots along the AlAs layer and the resulting electron-hole exchange interaction.

Upon increasing the excitation power density, several sharp lines at lower (1.3044 eV) and higher (1.3135 eV, 1.3148 eV, 1.3166 eV and 1.3182 eV) energies emerge.

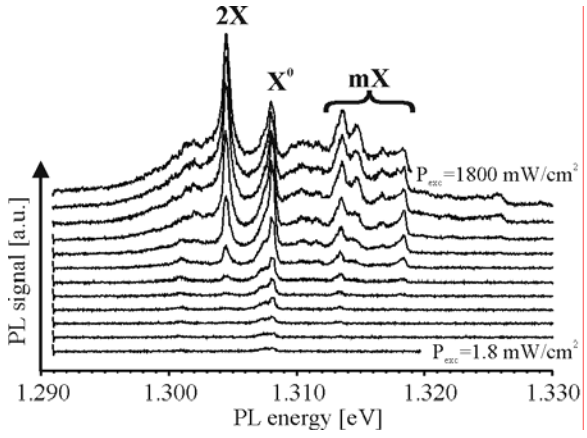

Fig. 3: *µ-PL spectra of a single InAs quantum dot on the (1-10) cleaved surface as a function of excitation power. For clarity, subsequent spectra are offset vertically.*

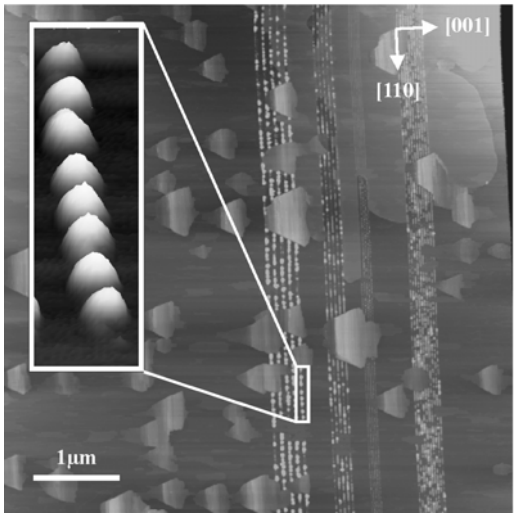

Fig. 2: *Atomic force microscopy picture of the well ordered InAs quantum dots. The inset shows a close-up of 8 perfectly aligned quantum dots with very similar size and shape. In the upper right corner of the picture the edge of the sample is visible.*

In particular, the intensity of the emission line at 1.3044 eV increases quadratically with excitation power density and dominates the spectra for the highest excitation densities investigated. This characteristic behavior identifies this peak as arising from bi-exciton (2X) recombination in the dot, an observation which is further supported by the lineshape which, in contrast with the single exciton, exhibits no exchange splitting as expected from the spin-singlet nature of the bi-exciton ground state. The other lines probably arise from multi exciton complexes (mX) and charged excitons.

In conclusion the fabricated quantum dots show excellent optical properties and have a high potential for the realisation of well defined arrays of quantum dots with weak inhomogeneous broadening.

supported by DFG (SFB 348 A10)

Influence of the interfacial oxide layer on the aluminum-induced layer exchange process

Mario Gjukic[1], Jens Lübke, Robert Lechner, and Martin Stutzmann

Polycrystalline silicon is increasingly gaining importance for the fabrication of large-area devices such as flat panel displays or thin film solar cells. Of fundamental importance for the commercial application is the use of cheap and transparent substrates, for example glass, requiring low temperature processing (T < 550 °C). In addition to chemical vapor deposition, solid phase crystallization and laser-induced crystallization, metal-induced crystallization of amorphous silicon (a-Si) can also be applied for the formation of poly-Si thin films on substrates such as glass.

One technique which is known to lead to poly-Si layers with good structural and electronic properties is the aluminum-induced layer exchange (ALILE) process. We are investigating the improvement of this method and its adaptability to the binary SiGe system. Fig. 1 illustrates the ALILE process. A bilayer of aluminum (Al) and amorphous silicon or silicon-germanium (a-SiGe) is deposited on a glass substrate by e-beam evaporation (Fig.1a). If the layers are separated by a thin oxide film, for example aluminum oxide, the annealing process results in a complete layer exchange and the formation of a coherent poly-SiGe thin film. Shortly after the annealing treatment starts, SiGe nuclei begin to form (Fig.1b). The crystallites grow into the Al layer until they reach the glass surface (Fig.1c). At this point lateral growth starts (Fig.1d) and leads to the formation of a polycrystalline SiGe layer on the glass substrate (Fig.1e). The remaining aluminum layer can be removed by wet-chemical etching.

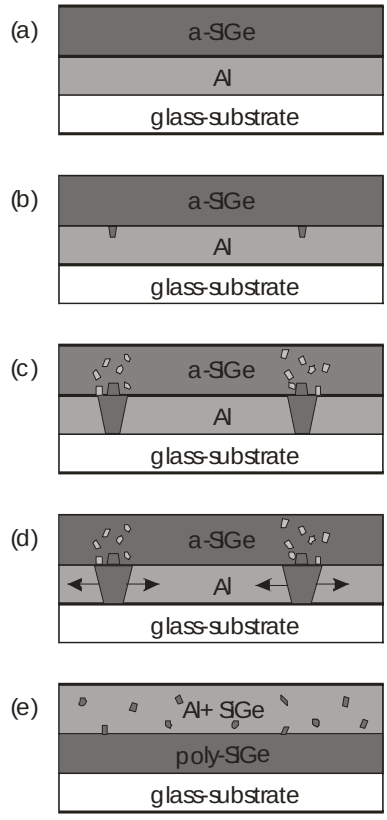

In accordance with two other groups we have observed that the relevant process parameters controlling the final grain size of the silicon crystallites are, among others, the annealing temperature, the thickness of the oxide interface layer and the aluminum grain size. Moreover, so far research on the ALILE process has focused on samples without or with a native aluminum- or silicon-oxide layer only. Since the native aluminum-oxide thickness is limited to about 1 nm due to self-passivation, we have investigated the influence of a deposited aluminum-oxide interlayer with a thickness up to 40 nm on the process dynamic and the surface morphology.

Fig.1: *Schematic cross-section view of an aluminum-induced layer exchange (ALILE) process: (a) – initial sample structure; (b) to (e) – temporal evolution of the layer exchange process.*

[1]phone:+49-89-289-12783, fax:+49-89-12737, email: gjukic@wsi.tum.de

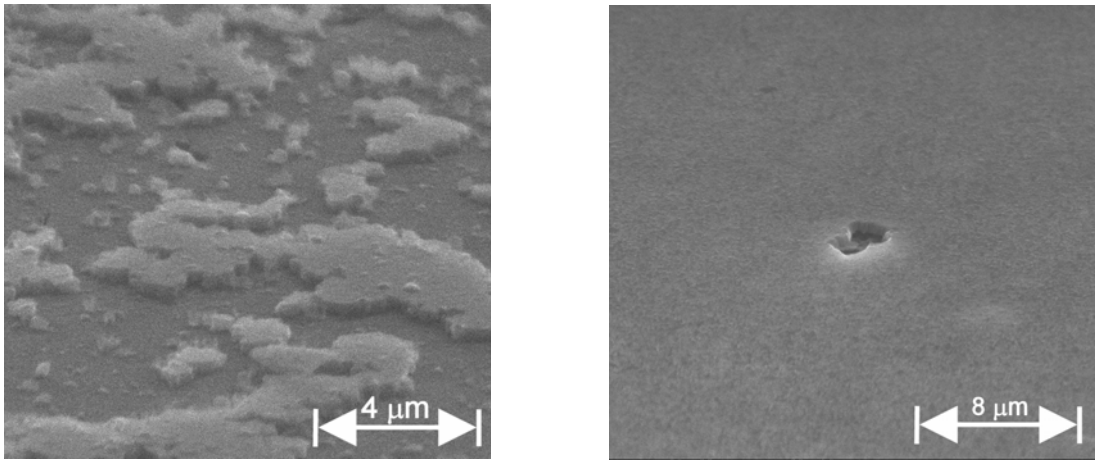

Fig.2: *Scanning electron micrographs of poly-Si samples after Al removal. Samples with a native oxide layer show the formation of polycrystalline precipitations on the closed poly-Si thin film (left). The samples with a thicker interfacial aluminum-oxide layer (40 nm) reveal smooth surfaces (right). For better visualization/contrast a single pinhole in the middle of the right picture is shown. In both cases the thickness of the coalesced poly-Si thin film is about 0.3 µm.*

The experiments have shown that the annealing time necessary for the layer exchange increases with an increase in oxide layer thickness. In the case of a native oxide interlayer, the time for the layer exchange is in the order of 30 minutes, for an oxide interlayer thickness of 40 nm about 1000 minutes (T = 530°C). Apparently, the interfacial aluminum-oxide layer acts as a barrier reducing the flux of dissociated silicon atoms into the aluminum matrix.

We also have observed that the nucleation density is reduced by the thicker aluminum-oxide layer. This is in agreement with a model for the ALILE process which was originally proposed by O. Nast and extended by us to take the interfacial oxide-layer into account.

Of considerable interest is the surface morphology of the samples after the ALILE process. In the case of a native oxide layer, the ALILE process leads to the formation of polycrystalline silicon precipitations on the coalesced polycrystalline surface (Fig.2 left). The formation of these ‘hillocks’ is a common observation for all experiments on ALILE up to now. The samples with an artificial aluminum-oxide layer, on the other hand, exhibit a distinctly different surface morphology, with a complete absence of hillocks and smooth surfaces (Fig.2 right).

The use of artificial aluminum-oxide layers seems to be a promising and technologically simple way of obtaining polycrystalline silicon layers with adequate surface morphology for further epitaxial thickening. Since the sample with the thinnest aluminum-oxide interlayer (about 5 nm) already exhibited this desirable surface morphology, future work will focus on the minimization of the oxide interlayer thickness and thus the reduction in annealing time.

Supported by ‘BMWA’ (contract No. 0329814A)

Transport properties of ALILE silicon-germanium thin films

Robert Lechner[1], Michael Buschbeck, Mario Gjukic, and Martin Stutzmann

Crystalline silicon-germanium alloys (c-$Si_{1-x}Ge_x$) are indirect semiconductors whose optical and electronic properties strongly depend on the germanium concentration x. Upon alloying silicon with germanium, the fundamental band gap and characteristic interband transitions shift to lower energies. Thus, even sub-micron thick layers can absorb a large fraction of the solar spectrum, making this material interesting for the application as an absorber in thin film solar cells.

This fact is illustrated by Figure 1, where the absorption coefficient of various c-$Si_{1-x}Ge_x$ alloys is plotted versus photon energy, together with the solar irradiation density. Obviously, already a 300 nm layer of c-$Si_{0.25}Ge_{0.75}$ is able to absorb 73% of the incoming photons, compared to 28% for pure silicon of the same thickness. In particular, c-$Si_{0.15}Ge_{0.85}$ is a promising candidate for a thin film photovoltaic absorber, since it combines the enhanced absorption with a still sufficiently large indirect band gap to enable reasonable energy conversion efficiencies.

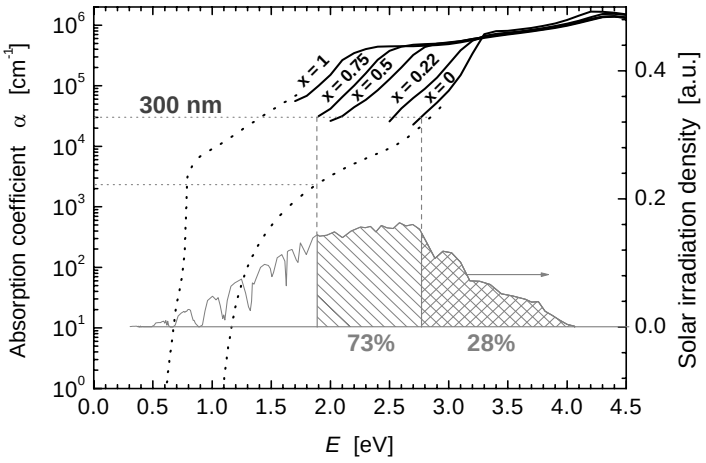

Fig. 1: *Absorption coefficients of c-$Si_{1-x}Ge_x$ alloys (lines) and spectral density of the solar irradiation (lower graph).*

To obtain thin films of crystalline silicon on glass substrates, the aluminum induced layer exchange (ALILE) process has been used.

We have observed (cf. p. 40) that SiGe alloys also can be recrystallized via ALILE throughout the entire alloy range, without significant phase segregation. The only constraint is the lower eutectic temperature of the Al-Si-Ge ternary system limiting the annealing temperature to below 420°C. Optical reflectivity and Raman measurements have attested the good crystalline quality of the resulting large-grained polycrystalline films.

The electronic properties of ALILE-produced SiGe mainly are determined by the intimate contact with the aluminum during the layer exchange reaction. Since aluminum is known to act as a shallow acceptor in SiGe, p-type conductivity of the recrystallized films is expected. The results of room temperature Hall measurements with a series of ALILE silicon-germanium samples are shown in figure 2. Here, the symbols mark the measured hole concentrations. The solid solubilities of aluminum in silicon ($8\times10^{18}cm^{-3}$) and germanium (5×10^{20} cm^{-3}) at the annealing temperature are interpolated for intermediate alloy compositions by the continuous line, which has been obtained from a simple interpolation model. The dashed line indicates the fraction of ionized acceptors at room

[1]phone:+49-89-289-12783, fax:+49-89-289-12737, email: lechner@wsi.tum.de

temperature, taking into account the appropriate ionization energies (E_{Al}(Si) = 70meV … E_{Al}(Ge) = 10meV).

As evident from Figure 2, hole concentrations both in ALILE silicon and $Si_{0.75}Ge_{0.25}$ agree well with the expected values of $2\times10^{18}cm^{-3}$ and $5\times10^{18}cm^{-3}$, respectively, while samples with germanium fractions x >0.5 show the behavior of degenerately doped semiconductors. This is in good accordance with the estimated critical Mott densities marked by the shaded area. For these samples, the measured hole concentrations equal the solid solubility of aluminum, reaching values as high as $4\times10^{19}cm^{-3}$, $7\times10^{19}cm^{-3}$, and $8\times10^{20}cm^{-3}$, for $Si_{0.55}Ge_{0.45}$, $Si_{0.70}Ge_{0.20}$, and Ge, respectively.

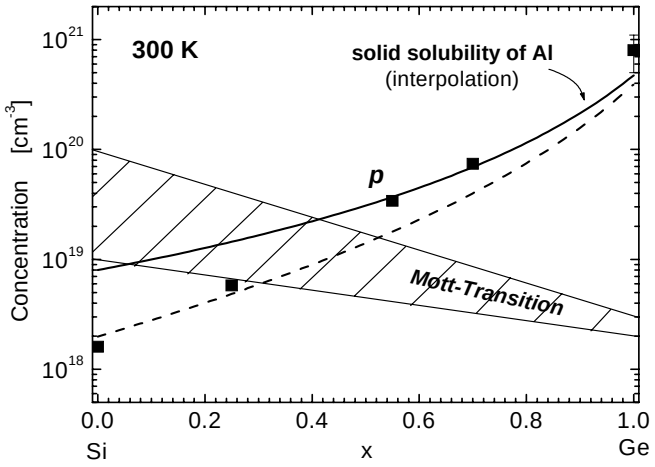

Fig. 2: *Room temperature hole concentration versus alloy composition in 200nm thick ALILE $Si_{1-x}Ge_x$-films (symbols) and solid solubility of aluminum in SiGe (continuous line).*

The Hall mobility and dark conductivity data are shown in Table 1. Given the high doping level in the crystallized films, the observed Hall mobilities of 10–60 cm^2/Vs at 300 K are rather high compared to what can be reached by other recrystallization methods. In the case of pure Si, the mobility is only a factor of two lower than literature values for monocrystalline bulk material with a similar doping level. For the Ge-rich alloys, the lower mobilities are partially due to the very high acceptor concentration. A second reason is the fact that in this alloy range, coherent thin films covering the entire substrate surface could not be produced so far. Thus, the mobilities given in Table 1 are only a lower limit for the true intra-grain mobility, which actually is the relevant parameter for thin film solar cell applications of a polycrystalline absorber material, where the lateral grain size is much larger than the grain thickness.

Ge content x	σ (1/Ω cm)	μ_p (cm^2/Vs)
0	14	60
0.25	15	20
0.55	44	8
0.70	52	5
1	990	8

Tab.1: *Dark conductivity and Hall mobility at room temperature.*

To reduce the high carrier concentrations, first passivation experiments with atomic hydrogen have shown that the electrical activity of the aluminum acceptors can be diminished by roughly two orders of magnitude. Further experiments will focus on the epitaxial thickening of ALILE silicon-germanium seed layers.

supported by BMWA (contract #0329814A).

Novel methods for the seeding of pore-arrays in silicon

Svetoslav Koynov[1], Martin Brandt, and Martin Stutzmann

Areas of ordered macro-pores in silicon can have attractive applications in optoelectronics, micromachining and cell biology. Such areas consists of vertical channels (along {100} direction) with surface openings ordered in a periodic lattice. The channels can have circular to square cross-section with typical dimensions of 1-20 µm and a lattice period about twice the diameter. The aspect ratio (depth/diameter) can reach several hundreds. The pores are prepared by anodic etching of weakly doped, n-type (100) Si, in a HF:H_2O electrolyte under back side illumination. A key step in the preparation of ordered arrays is the pore seeding. It determines the pattern of micro-channels by creation of etch pits in the Si surface, at which the electrochemical pore formation initiates. Usually, the pits are made by oxidation of Si surface, followed by standard photolithography to open windows in the SiO_2 layer, and subsequent anisotropic KOH etching. This way, uniform array of inverted pyramids with sharp tips is formed in the Si surface. This method gives excellent results once the typical lattice dimensions are larger than a few micrometers. On the other hand, it becomes problematic if small pores (diameters bellow 1 µm) are needed. Some additional limitations are illustrated in Figure 1. The base of a pyramid is bigger than the respective window in a photo-mask due to the enlargement caused by the subsequent etching processes. Thus, the pores with diameter below 1 µm, have a pyramidal opening at the initial surface. This can be a problem for some applications, which need an abrupt start of the channels from a flat surface. Another problem is the appearance of parasitic pores at the sharp edges of the remaining pyramidal parts due to a concentration of the electric field there during the electrochemical process. Such pores tend to branch and diverge from the {100} direction, thus, destroying the ordered micro-channel structure.

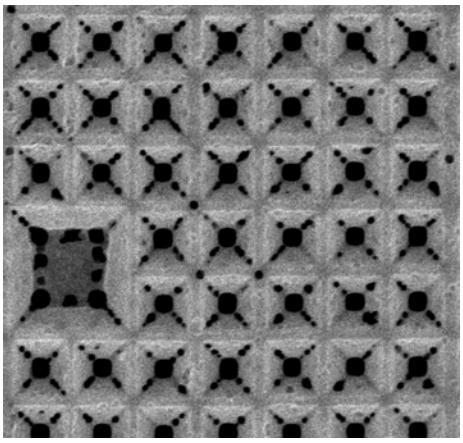

Fig. 1: *Top view of ordered pore area, obtained by standard lithographic seeding. The lattice period is 2 µm. The mouths of the channels can be seen as squares (contours of the pyramidal bases). Small parasitic pores are developed at the sharp edges of the pyramids, appearing as crosses around the central pore .*

To avoid such problems we have developed a new approach to the seeding of ordered pores, based on holographic laser patterning. The experiments have been carried out by using a pulsed YAG:Nd laser, operating at the second harmonic (532 nm) or third harmonic (355 nm). By 3-beam interference a dot square lattice is projected on the sample surface with a single 10 ns pulse. To transfer this holographic image into etch pits we

[1]phone: (+49-89)289-12765, fax: (+49-89)289-12737, email: koynov@wsi.tum.de

deposit a thin film of gold (20-30 nm) directly onto the clean Si surface after the native oxide has been removed by HF dip. The idea is to induce alloying of the metal with Si in the illuminated parts of the pattern during the intense laser pulse ("Metal-Induced Seeding" - MIS). Gold was chosen because it can form a low temperature eutectic with Si (melting point of 360^{o}C at 4 wt% Si and 96 wt% Au). Other advantages of Au are its optical properties – a strong decrease of the reflection in the green to UV range and high transparency of Au in the green region of the spectra (around the plasma frequency at 510 nm). Thus, a significant portion of the second harmonic pulse energy can be absorbed at the interface of the Au/Si system. The so-far optimized exposure conditions use a pulse energy of 540-600 mj/cm^2. After exposure, the remaining gold, including the alloyed part of Si, is removed from the sample by using aqua regia (HCl:HNO_3 3:1) and Standard Clean 2 solution (SC2-H_2O:H_2O_2:HCl 6:1:1). The result is shown in Figure 2a. Periodically ordered shallow craters with well defined positions can be seen. Uniform pores are formed after the anodic etch of the sample with these seeds as shown in Figure 2b.

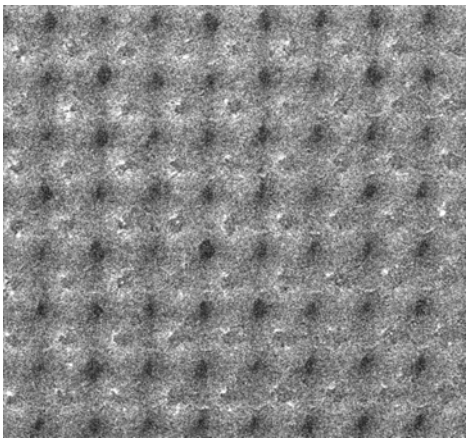

Fig. 2a: *"Metal-Induced Seeding" (MIS) of pore array in silicon. The seeding sites appear as craters with a typical size of 100-200 nm, ordered in a square lattice with 2 µm period.*

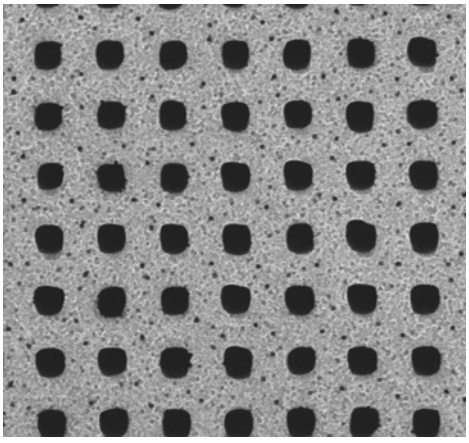

Fig. 2b: *Top view of ordered pore array, obtained by MIS. Channels of diameter below 1 µm start abruptly from the surface. The lattice period is the same as in Fig. 2a.*

Actually, a better pore uniformity has been achieved by using MIS than by the control experiments, which apply photolithographic processing to transfer the 3-beam interference pattern (at 355 nm) into inverted pyramidal pits. Figure 2b shows that an abrupt start of ordered pores from a flat surface can be achieved by MIS on the scale of 1 µm. An investigation of the ultimate resolution of the method is in progress. The technological advantage of MIS is that the process is simpler and less time-consuming than the standard photolithographic seeding.

---

supported by Bayerische Forschungsstiftung - Project ForNano, TP4

Micro-contact printing on silicon

Jorge Hernando[1], Radina Presker and Martin Stutzmann

The microfabrication of small structures is crucial for modern science and technology. Photolithography is the most common technology for microfabrication. However, as the feature size decreases towards 100 nm, photolithography is becoming increasingly challenging. These limitations of photolithography suggest the need for alternative microfabrication techniques. Among the different non-photolithographic techniques already demonstrated, soft lithographic techniques are very promising. Soft lithography is low in capital cost, procedurally simple, and features with lateral dimensions below 100 nm can be achieved. The key element of soft lithography is an elastomeric stamp or mold with the desired pattern. For micro-contact printing, the stamp is coated with a reagent containing specific “ink” molecules, and brought into contact with a substrate, the surface of which is functionalized in a way to provide specific bonding for the ink molecules. A patterned organic monolayer film is deposited on the substrate from the protruding features of the mold and this film can be used as a lithographic mask for subsequent processing of the substrate.

In this work we use micro-contact printing to fabricate micron-sized patterns on oxidized silicon. An organosilane molecule, octadecyltrichlorosilane (OTS), is used for the printing. The chemistry of this type of molecule is dominated by the reaction between the Si-Cl bonds of the molecule and hydroxyl groups:

$$Cl–SiR + H–O–R' \Rightarrow R'–O–SiR + HCl$$

R denotes an alkane, R´ the substrate surface. If hydroxyl groups are present at the surface, the molecules will bond covalently to them. However, this reaction could also take place with the hydroxyl groups in water (R´= H). Water can be present as a thin film on the oxidized surface as well as in the solvent. The reaction of the molecules with water would lead to their hydrolysis and polymerization. Therefore, there would be a competition between the desired reaction with surface and the unwanted polymerization, which could hinder the coating of the surface. For all these reasons, the control of the reaction conditions, especially water content in the solvent and on the surface, is of most importance.

We decided to study the chemistry of the reaction by dip coating, before using it for contact printing. The ink solution was always prepared inside a glove box under an Argon atmosphere (H_2O < 1 ppm, O_2 < 1 ppm). The solvent used was toluene. Crystalline silicon samples were oxidized by immersion in piranha etch (H_2SO_4:H_2O_2:3:1) at 100 º C for 1 hour. Next, the samples were rinsed in distilled water. This treatment yielded hydrophilic surfaces with a contact angle below 5 degrees.

The oxidized silicon samples were introduced in the glove box and were immersed in freshly prepared solution of OTS in toluene. The OTS concentrations were varied from 1 mM to 10 mM, and the time of immersion from 5 minutes to 24 hours. After the process, the sample was mechanically cleaned with a cotton swab soaked with toluene in order to remove any physisorbed material. For all these experiments, the obtained contact angle was never higher than 60 degrees. As the end group of the OTS molecule is a methyl group, this should give rise to hydrophobic surfaces with contact angles above 90 degrees.

[1]phone:+49-89-289-12765, fax:+49-89-289-12737, email: jorge.hernando@wsi.tum.de

So, we can conclude that the coating of the surface with OTS molecules was not effective in this case.

In order to control better the reaction, it was necessary to remove the solution from the glove box and to expose it to air. After 30 minutes of contact with air (humidity around 30 %), the solution was introduced again in the glove box and the immersion of freshly oxidized samples carried out. After 5 minutes of immersion in a 10 mM OTS solution, the measured contact angle was about 100 degrees (Fig. 1), confirming the dense attachment of OTS molecules on the surface. Further experiments are now in process in order to understand why it is necessary to remove the solution from the glove box.

Once the surface functionalization was under control for dip coating, the patterning of oxidized silicon was performed by soft lithography. The master used to make the stamp was a film of photoresist patterned by UV lithography. The elastomer material (poly(methylsiloxane), PDMS) to fabricate the stamp was poured over the master and cured for 12 hours at 60 º C. The structure of the stamp consists of a periodic pattern of squares with a side of 4 microns.

The printing procedure was as follows. The stamp was covered with 10 µl of ink solution per each mm^2 of stamp for 30s. The solution was prepared in the same way as for dip coating, in order to activate the reaction. Next, the stamp was dried with nitrogen for another 30 s and placed over the sample without applying any pressure. A conformal contact could be observed. In order to minimize the swelling of the stamp after being impregnated with the solution, the backside of the stamp was fixed to a glass substrate. The success of the printing was first checked with planar stamps, where again contact angles of about 100 degrees for a printing time of 5 minutes and an OTS concentration of 10 mM were obtained. Next, the patterned stamps were used to pattern the silicon surface. Figure 2 is an AFM image of the oxidized silicon after printing, showing 4 micron-sized OTS-coated squares.

Further experiments are planned to minimize the spreading of the molecules during printing beyond the protruding features of the stamp and to investigate OTS resistance to chemical etching in order to transfer the pattern on the silicon.

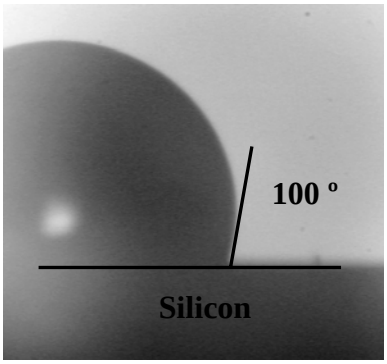

Fig. 1. *Contact angle of OTS-coated silicon after 5 min. in 10 mM OTS solution.*

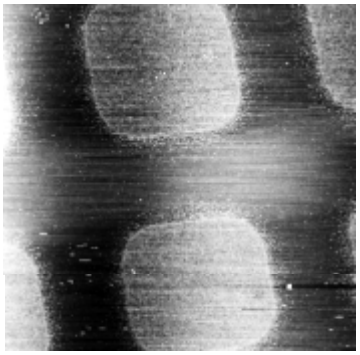

12 µm x 12 µm

Fig. 2. *AFM image of 4 micron-sized OTS-coated squares on silicon after micro-contact printing.*

supported by BMBF 01SF0120 (Photonen-Management).

AlGaN/GaN field effect transistors for biosensors

Georg Steinhoff[1], Barbara Baur, Martin Stutzmann, and Martin Eickhoff

Field effect transistors based on AlGaN/GaN heterostructures are of great interest for chemical and biochemical sensor applications. Chemical sensors based on Pt:GaN Schottky diodes and AlGaN/GaN heterostructure field effect transistors for the detection of hydrogen and hydrocarbons up to temperatures of 600°C have been demonstrated. In addition to their high temperature stability, AlGaN surfaces are chemically inert in aqueous solutions and non-toxic to living cells, which are basic requirements for the application as a functional material for biosensors.

Recently, we have demonstrated the deposition of highly mobile lipid membranes on hydrophilized III-nitride surfaces by vesicle fusion. This allows the design of biosensors based on such lipid membranes deposited directly on the nonmetallized gate regions of AlGaN/GaN transistors. These devices should allow the electronic detection of ligand binding to specific receptors in the lipid membrane as well as electrochemical detection of transmembrane transport. A different approach for the realization of biosensors is the cultivation of living cells directly on the gate area and the measurement of their ionic response to chemical, physical or biological stimuli.

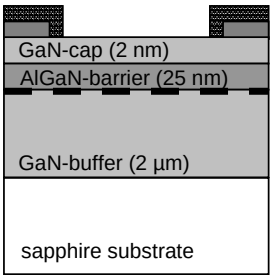

Fig. 1: *Schematic layout of the GaN/AlGaN/GaN transistor structure*

For this purpose, transistor arrays of 4x4 transistors with a channel length and width of 35µm were fabricated on MOCVD grown GaN/AlGaN/GaN heterostructures shown in Figure 1. The 2DEG carrier density was determined to $n_{2DEG}= 8\cdot10^{12}$ cm^{-2} by capacitance-voltage measurements. For electrical characterization in aqueous solutions, the potential V_{GS} of the electrolyte gate with respect to the source contact was adjusted via an Ag/AgCl reference electrode by a potentiostat.

Figure 2 shows the drain-source current, I_{DS} as a function of the gate-source voltage V_{GS} and different drain-source voltages V_{DS}. For sensor applications the transistors are operated at the point of the highest transconductance of $g_m= 0.1mS$ (operating point: $V_{DS}= 0.2V$, $V_{GS}= -1.8V$) for maximum sensitivity to changes in the surface potential. Cyclic voltametry measurements revealed a stable surface and insignificantly low leakage current I_{GS} form the device gate into the electrolyte for gate-source voltages V_{GS} between -4V and 0V

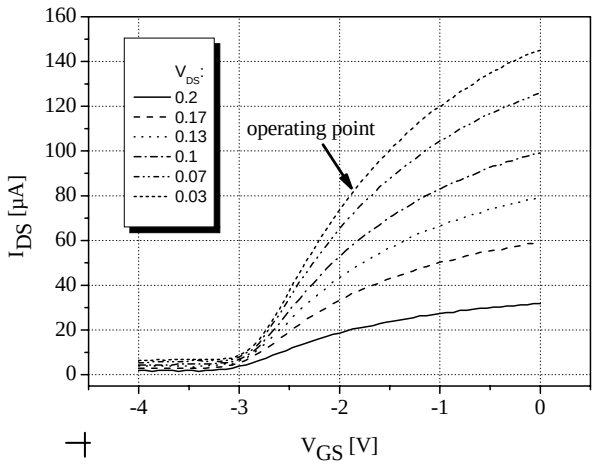

Fig. 2: *I_{DS} as a function of V_{GS} for different V_{DS}*

Different types of cells (cardiac myocytes, HEK-cells, cortical neurons) were cultivated directly on the device surface and exhibited good adhesion and conserved vitality. Figure 3 shows a

[1]phone:+49-89-289-12774, fax:+49-89-289-12737, email: steinhoff@wsi.tum.de

cortival neuron cell adhered directly on the transistor gate area.

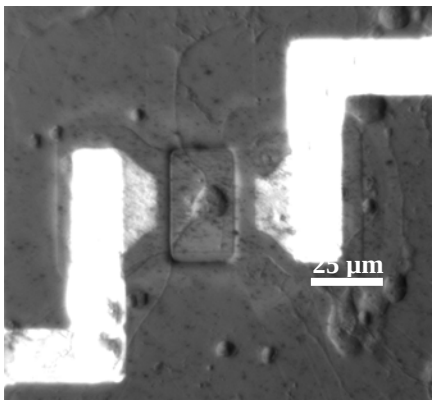

Fig. 3: *Neuron on the gate of a transistor*

As H^+, Na^+, K^+, Ca^{2+} and Cl^--ions are important ions for cell metabolism and give the main contribution to cell action potentials, we have investigated the response of AlGaN/GaN transistors and transistor arrays to changes in the concentration of these ions in the ambient electrolyte. The total ionic strength of the electrolyte was kept constant by adequate buffer solutions. The potential drop at the interface between the gate surface and the electrolyte was the sensor signal. A linear sensor response of approximately 56 mV/pH was found for variations in the H^+-concentration between 10^{-1} and 10^{-13} mol/l, which is close to the theoretical Nernst limit, determined by the native oxide layer present on the surface. Additionally, GaN surfaces are highly selective, because almost no sensitivity (<2 mV/decade) was found towards Na^+, K^+ and Cl^--ions over 5 decades in concentration.

For the measurement of cell action potentials, relatively small equivalent gate-source voltages around 1mV have to be resolved. Therefore, noise and transconductance of the transistor arrays are the crucial device parameters. Cell signals were simulated by applying 100ms gate-source voltage pulses and recording the sensor signal. Figure 5 shows that even a -100µV pulse could clearly be resolved in the background noise.

Further improvement of the device sensitivity by enhanced transconductance due to a larger channel width to length ratio is likely to be possible.

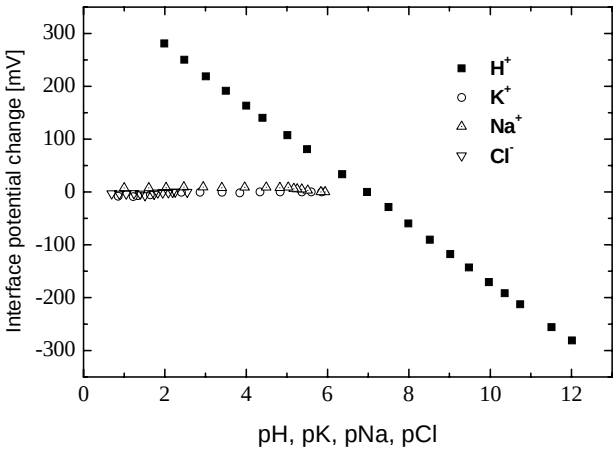

Fig. 4: *Variation of the GaN/electrolyte interface potential as a function of specific ion concentrations*

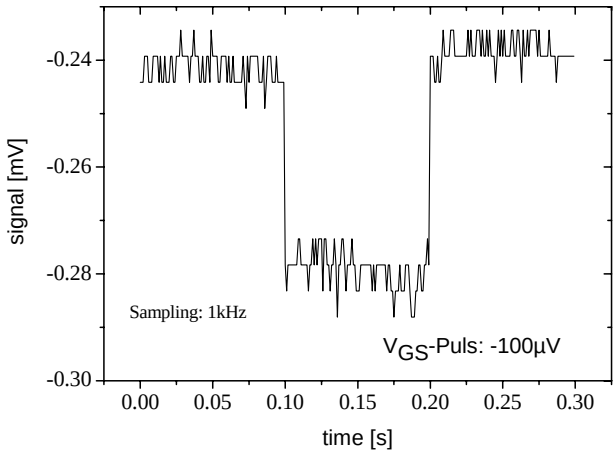

Fig. 5: *Sensor response to a -100µV V_{GS}-pulse*

supported by DFG (SFB 563 B11)

Surface functionalization of GaN and AlN

B. A. K. Baur[1], G. Steinhoff, J. Hernando, M. Stutzmann, and M. Eickhoff

Biosensor applications of semiconductor devices for operation in aqueous electrolyte solutions are currently a topic of intense research. Wide bandgap semiconductors, such as group III-nitrides are regarded as promising materials for these applications, as they combine high chemical inertness with optical transparency and low thermally generated noise in electronic devices. Investigations of cell adhesion on AlGaN-surfaces have demonstrated the biocompatibility of this material system. Recent work revealed a stable operation of AlGaN/GaN heterostructure ion sensitive field effect transistors (ISFETs) in aqueous electrolytes. The pH-sensitivity of such devices showed an almost Nernstian behaviour.

For the realization of biosensors, biological systems like enzymes, lipid layers or living cells have to be attached to the device surface. For this purpose, a detailed understanding and the control of the anorganic/organic interface are basic requirements. We have investigated the functionalization of GaN- and AlN-surfaces by deposition of self-assembled monolayers (SAMs) based on two different kinds of alkylsilanes. Aminopropyltriethoxysilane (APTES) contains an amino group at the end of the hydrocarbon chain and can act as a reactive end group for further attachments of e.g. crosslinkers. Octadecyltriemethoxysilane (ODTMS) with its long hydrocarbon chain provides a hydrophobic surface after SAM formation. Silanization is performed by a self-assembly process from an organic solution of silane molecules (Figure 1). During the silanization process, hydroxyl groups have to be provided which are formed on oxidic surfaces and act as covalent coupling sites for alkylsilane to form a siloxyl bond [1].

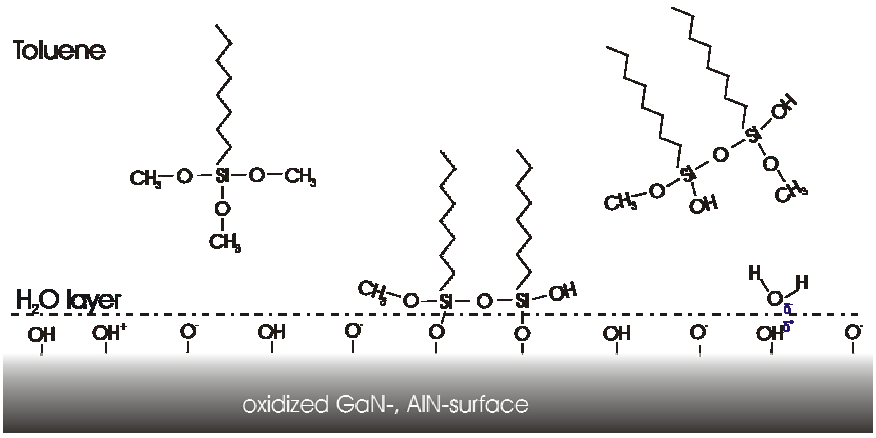

Fig. 1: *Covalent binding of alkylsilanes to hydroxyl groups at the oxidized surface and competing reactions.*

One of the crucial points in order to achieve a homogenous siloxane coverage is the water content in the organic solution as well as on the surface. A certain amount of H_2O at the oxidic surface is required to hydrolyse both, surface groups and active side groups of silane. On the other hand water in the solution leads to polymerisation of silane molecules. Finally H_2O-molecules at the surface can block the hydroxyl groups there.

[1]phone:+49-89-289-12769, fax:+49-89-289-12737, email: baur@wsi.tum.de

In order to obtain hydrophilic surfaces, we have compared wet thermal and chemical (H_2SO_4:H_2O_2) oxidation processes on GaN- and AlN-surfaces with respect to their efficiency in the silanization process. XPS measurements after hydrophilization showed thicker oxide layers (8-10ML) for the wet thermally oxidized AlN surface. However, contact angle measurements indicated that surface activation with H_2SO_4:H_2O_2 is

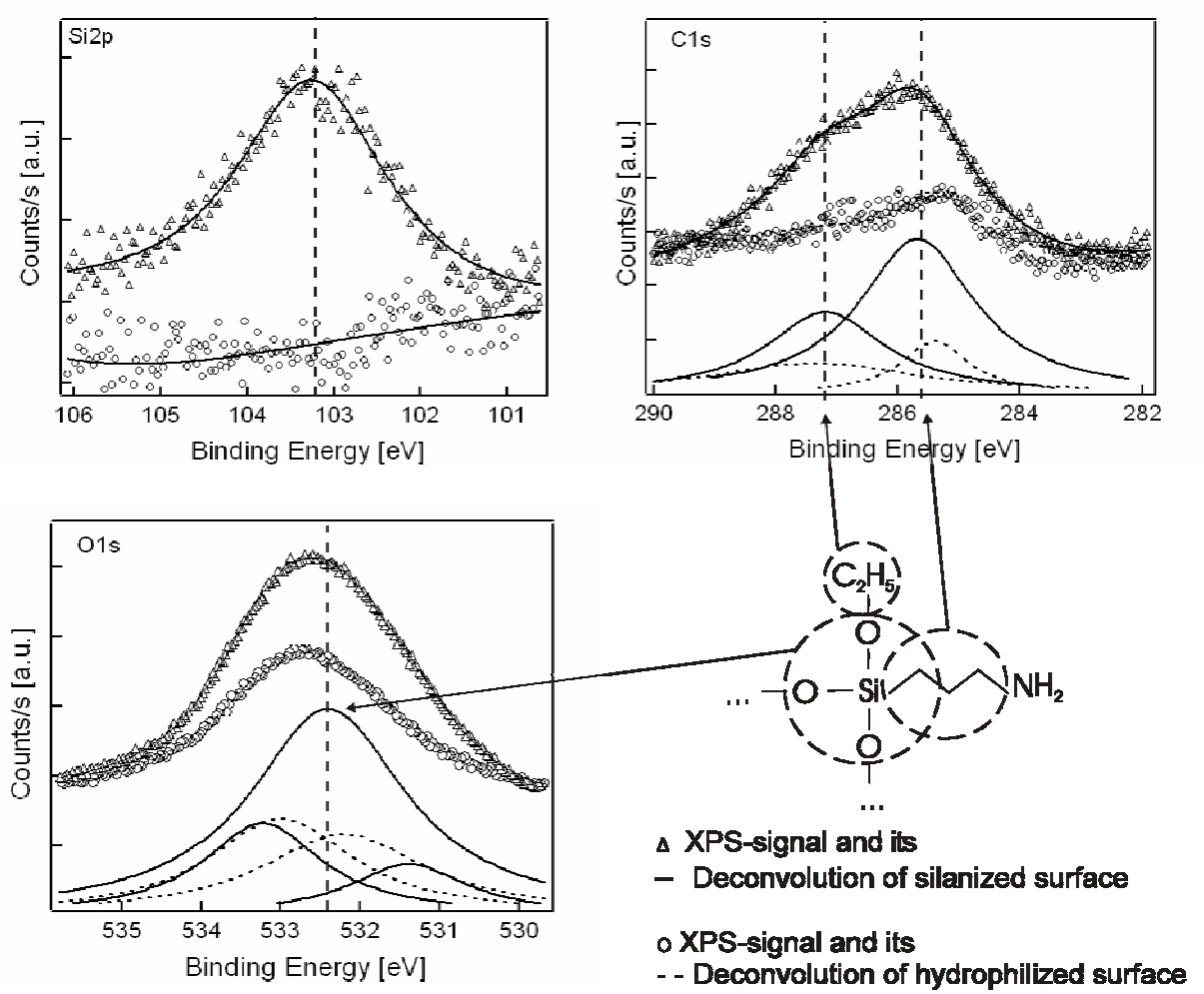

Fig. 2: *XPS-Signals for Si2p-, C1s-, O1s-Core level of silanized AlN surface (open triangles). The open circles indicate the reference signal of the hydrophilized surface.*

necessary to achieve sufficiently hydrophilic surfaces. A successive optimization of the silanization process with APTES led to homogenous coverage for oxidized surfaces.

X-ray photoelectron spectroscopy (XPS) measurements were also carried out to confirm the chemisorption of APTES on AlN (Figure 2). The Si2p core level peak at 103.1eV proves the existence of Si-O bonds on the surface. Together with the characteristic changes of the C1s and O1s core-level peaks, this provides convincing evidence for the formation of siloxane networks on the surface.

[1] Parikh et. Al., J. Phys. Chem., 1994, 98, 7577-7590

---

in collaboration with M. Tanaka

Active control of short DNA strands on gold surfaces

Ulrich Rant[1], Kenji Arinaga[*], Gerhard Abstreiter, and Marc Tornow

We have been conducting combined fluorescence and electrochemical studies on oligonucleotide monolayers immobilized on gold electrodes. The versatility of our experimental approach enabled us to investigate various aspects of the manifold and fascinating properties of DNA monolayers tethered to metal substrates, such as cooperative structural conformations of the layer, dictated by its molecular packing density, or to probe the polyelectrolytic nature of DNA, i.e. its effective charge which adjusts according to the ionic strength of its surrounding electrolyte. We also succeeded to attain active electrical control over the DNA orientation with respect to the surface; by applying AC potentials to the electrode, we can persistently switch the strand-conformation on the surface, thereby adding a novel functionality to this system which opens incredible perspectives to new fundamental investigations as well as applications.

Figure 1 presents optical investigations on the conformation of oligonucleotide layers on Au surfaces. These studies concentrate on the effect of varying surface coverage densities on the structural properties of layers of 12 and 24mer single stranded (ss) DNA, tethered to the Au surface at one end while being labelled with a fluorescent marker at the opposing end. The distance dependent energy transfer from the marker dye to the metal surface, which causes quenching of the observed fluorescence, is used to provide information on the orientation of the DNA strands relative to the surface. Variations in the oligonucleotide coverage density, as determined from electrochemical quantification, over two orders of magnitude are achieved by employing different preparation conditions. The observed enhancement in fluorescence intensity with increasing DNA coverage can be related to a model involving mutual steric interactions of oligonucleotides on the surface, as well as fluorescence quenching theory, showing good agreement. Hence, we are able to extract the effective length of the oligonucleotides which points to a considerable flexibility of the DNA in its single stranded conformation.

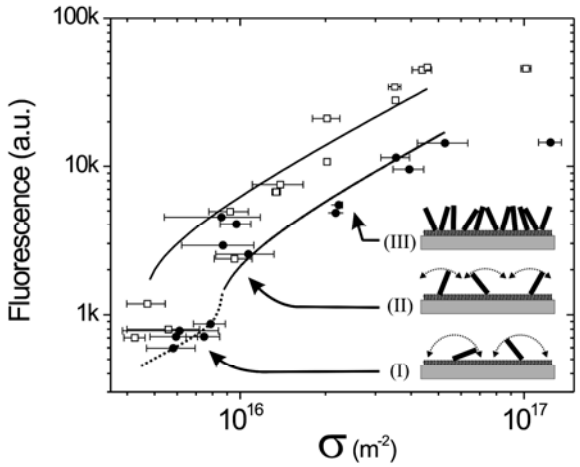

Fig. 1: *Fluorescence vs. number density of oligonucleotides of single stranded 12mer (solid circles) and 24mer (open squares) on the surface. The inset depicts three regimes of steric interactions denoted by different monolayer packing densities. Solid lines are model calculations.*

Control over the electrochemical potential of the DNA-supporting electrode gives access to a variety of measurements making use of electrostatic interactions between the intrinsically charged DNA and its biased substrate. By tuning the electrode potential to substantially negative values (e.g. -0.8V vs. Ag/AgCl), we observed a bias induced release of

[1] phone:+49-89-289-12776, fax:+49-89-320-6620, email: rant@wsi.tum.de

immobilized, ss24mer oligonucleotides from Au-surfaces into electrolyte solutions of varying ionic strength (cf. Figure 2). Desorption was evidenced by fluorescence measurements of the dye labelled ssDNA. Electrostatic interactions between adsorbed ssDNA and the Au-surface were investigated with respect to (i) a variation of the bias potential applied to the Au-electrode, and (ii) the screening effect of the electrolyte solution. For the latter, the concentration of monovalent salt in solution is varied from 3 to 1600mM. We find that the strength of electric interaction is predominantly determined by the effective charge of the ssDNA itself and that the release of DNA mainly occurs before the electrochemical double layer has been established at the electrolyte/Au interface. In agreement with Manning's condensation theory, the measured desorption efficiency (η_{rel}) stays constant over a wide range of salt concentrations, however, as the Debye length is reduced below a value comparable to the axial charge spacing of the DNA, η_{rel} decreases substantially. We assign this effect to *excessive counterion condensation* on the DNA in solutions of high ionic strength.

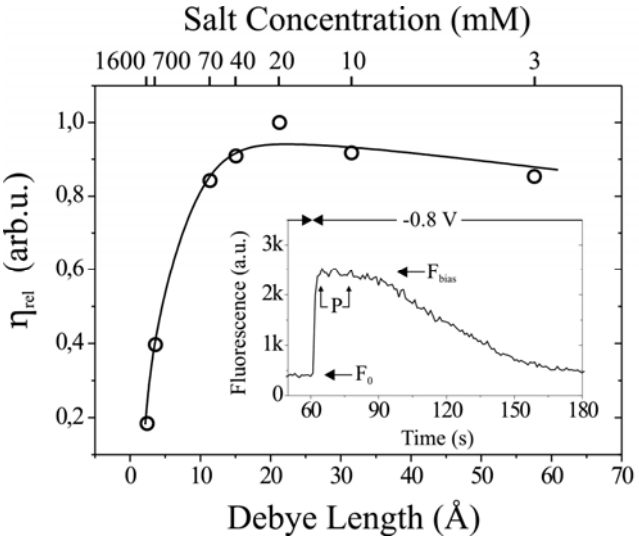

Fig. 2: *Relative desorption efficiency η_{rel} of ss24mer DNA from Au-electrodes upon application of -0.8V as determined from fluorescence measurements. The sharp decrease of η_{rel} at high salt concentrations denotes a neutralisation of the DNA's negative charge. Inset: Transient fluorescence enhancement due to desorption of molecules from the surface upon application of the negative bias step.*

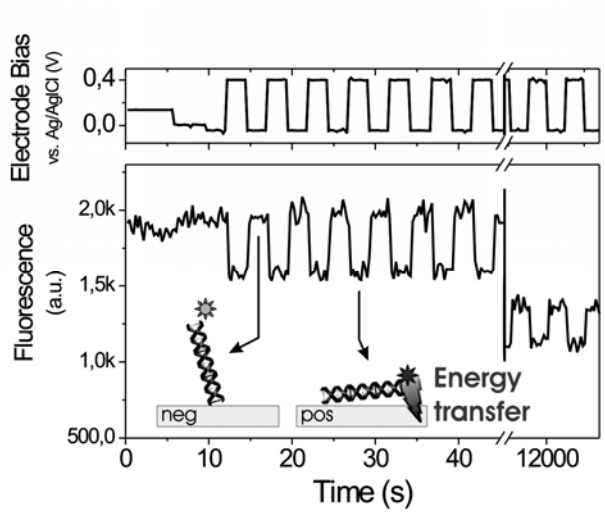

Fig. 3: *Persistent switching of DNA orientations on Au-electrodes. Inset: distance dependent energy transfer causes the lying conformation to be 'dark'.*

When tuning the potential of the Au substrate carefully across the electrode's potential of zero charge, it is possible to induce conformational changes in the DNA monolayer without causing desorption and therefore achieve remarkable sample stability. Figure 3 depicts persistent switching between a 'lying' and 'standing' state of the tethered DNA on the surface, induced by applying AC potentials to the Au electrode.

supported by Fujitsu Laboratories Europe and DFG (SFB 563)
* Fujitsu Laboratories Ltd., 10-1 Morinosato-Wakamiya, Atsugi 243-0197, Japan

Controlling the surface density of immobilized DNA on Au

Kenji Arinaga[1], Ulrich Rant, Marc Tornow, and Gerhard Abstreiter

Self-assembled monolayers of organic molecules immobilized on Au surfaces have many possibilities for various application fields as novel functional surfaces due to various tailored groups attachable to the end group of the molecules. Especially, if DNA is used as a functional end group, this DNA can be further modified in order to establish linkage to other bio-molecules, and then we can expect to apply this scheme to biosensor applications as a new bio-compatible surface.

A conventional method to obtain such a bio-functional surface is using self-assembled monolayers of alkanethiol molecules with oligonucleotides attached[*]. Using this method, DNA layers can be formed relatively easily, however, in the case of densely packed DNA layers, one must take care of the steric hindrance between DNA strands; particularly if other molecules, for example proteins, are linked to the DNA, significant steric hindrance might occur. Therefore, a technology which can accurately assess and control the surface density of DNA layers on Au is necessary.

In aqueous solution DNA is highly negatively charged along its phosphate backbone, and, as a consequence, DNA strands repel each other. Furthermore it is known that positive counter-ions surround the DNA molecules in the electrolyte to partially compensate (screen) the DNA's negative charge. This screening effect strongly depends on the ion concentration in the electrolyte. Therefore, the distance between immobilized DNAs can be controlled by changing the ion concentration in solution, which constitutes a possibility of adjust the surface density of immobilized DNA on Au surfaces. Moreover, the surface density of DNA also depends on the density and the diffusion mobility of DNA in the electrolyte. Considering the arguments of above, we tuned the DNA surface density by changing the ion concentration and immobilization time to clarify the dependency of such parameters. For quantitative determination of the surface density, we used an electrochemical technique which detects the amount of redox markers (Hexaammineruthenium III chloride) compensating the negative charge of DNA (Steel et al, Anal. Chem. 70, 4670, 1998).

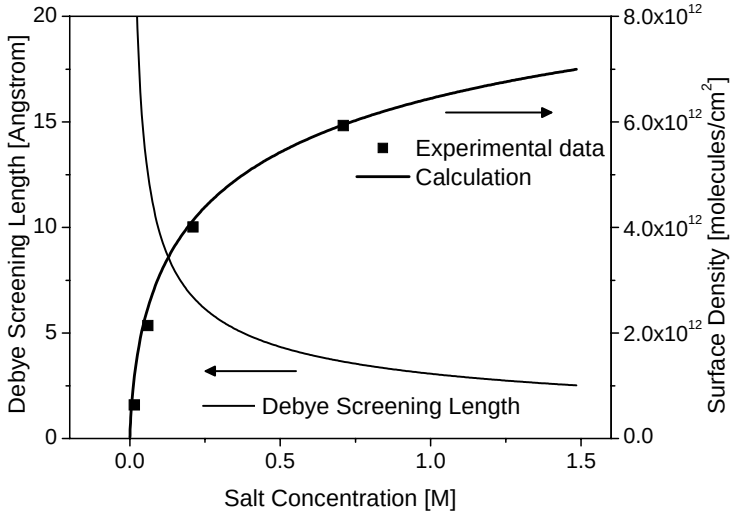

Fig. 1: *Debye screening length and immobilized DNA surface density vs. monovalent salt concentration (squares: experimental data, solid lines: calculation)*

Figure 1 shows the measured surface density of DNA molecules on Au together with the Debye screening length versus the ion (salt) concentration. We immobilized 12mer DNA which has an alkanethiol linker ($(CH_2)_6$-SH) using

[1]phone:+49-89-289-12775, fax:+49-89-320-6620, email: arinaga@wsi.tum.de

Tris as buffer and varying concentrations of NaCl as salt in the electrolyte solution. DNA and Tris concentration were fixed to 10µM and 10mM, respectively. In the regime of low salt concentration, the immobilized DNA density is significantly low because of pronounced mutual DNA-DNA repulsion due to long Debye screening lengths. With increasing salt concentration the screening mediated by counter-ion (Na^+, $Tris^+$) is getting more effective, such that DNA can be immobilized in a more densely packed layer. As a result, high surface densities are obtained in the regime of high salt concentrations. Figure 1 also shows the calculated density using a simple model considering the Debye length and the DNA's molecular dimensions. According to the good agreement between experiment and calculation the immobilized DNA density can be controlled in a very exact manner via setting the salt concentration in electrolyte solution.

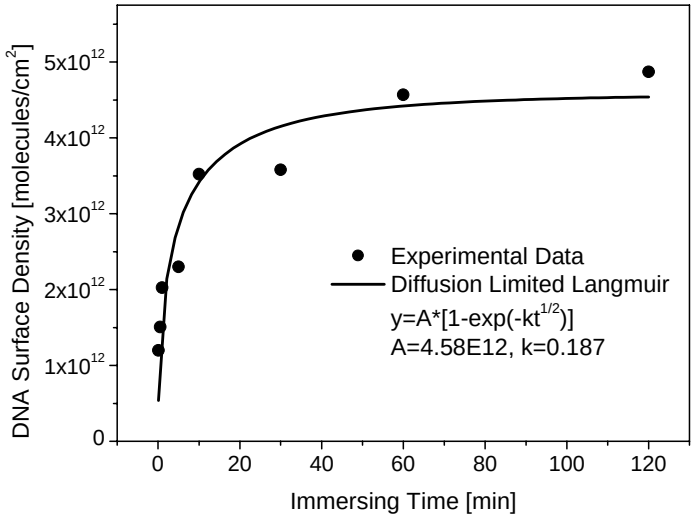

Fig. 2: *Immobilized DNA surface density vs. immersion time in electrolyte solution (circle: experiment, solid line: fit using the diffusion limited Langmuir adsorption model).*

Figure 2 presents the surface density of DNA on Au versus the immersing time in the DNA containing electrolyte solution. We used 24mer DNA with alkanethiol linker ($(CH_2)_6$-SH). DNA, Tris and NaCl concentration were fixed to 10µM, 10mM and 1M, respectively. At relatively short times the surface density increases rapidly as time increases before it eventually almost saturates. Figure 2 also depicts a fitting curve using a diffusion limited Langmuir isotherm. Due to the good agreement of the fitted model to experimental data we found that the DNA immobilization process can be explained by a diffusion limited Langmuir adsorption enabling us to estimate the obtained density in this way.

In summary, we have investigated how to control the surface density of immobilized DNA on Au surfaces studying the main mechanisms of the immobilization process as governed by electrolyte screening and molecular diffusion. The described techniques have high potential for applications in the functionalization of metal surfaces with organic and bio-molecules.

*The alkanethiol molecules assemble as monolayers, chemically linked to the supporting Au surface by Au-S bonds; van der Waals and hydrophobic interactions further facilitate layer growth and stabilization.

Financially supported by Fujitsu Laboratories of Europe and SFB563

Covalent attachment of proteins on nanocrystalline diamond

Andreas Härtl[1], Evelyn Schmich, José A. Garrido, Jorge Hernando, and Martin Stutzmann

Diamond exhibits several special properties, e.g. a good biocompatibility and a large electrochemical potential window, which make it particularly suitable for bio-functionalization and biosensing. Here, we show that proteins and enzymes can be attached covalently to nanocrystalline diamond thin films. Moreover, we have confirmed that, once immobilized at the surface, the biomolecules are still fully functional and active.

We have investigated nanocrystalline diamond (NCD) samples, grown on silicon substrates by hot wire chemical vapor deposition (HWCVD) from a CH_4 / Ar mixture. The thickness of the diamond film was about 2 µm and the average grain size was about 25 nm. As-grown samples were first cleaned, and then oxidized chemically with chromosulfuric acid. Finally, the samples were hydrogenated in a hot wire reaction chamber, resulting in a surface covered with C-H bonds, as confirmed by the high hydrophobicity of the hydrogen-terminated NCD.

The H-terminated surface was patterned with conventional photolithography using a regular array of 4 µm square spots. These spots were oxidized with an oxygen-plasma. The success of the oxidation was verified with Kelvin Force Microscopy. After cleaning, the sample surface was modified using a photochemical process. As a reagent we used a TFA-protected long chain ω-unsaturated amine, generating a surface layer of amine groups, to which proteins or enzymes can be covalently bound in several subsequent steps. The success of this first photochemical treatment was controlled by X-ray Photoelectron Spectroscopy (XPS). The presence of nitrogen in the amine groupand fluorine in the protection group on the treated diamond samples was confirmed.

The next step was the deprotection of the amine group. The function of the protection group attached to the amine is to prevent the photochemical reaction of the amine (instead of the carbon double-bond at the other end) with the C-H bonds at the diamond surface. The protection group can be removed with a 25 % solution of $(CH_3)_4NOH$ in methanol. The XPS-spectra of a deprotected sample confirms the disappearance of the F1(s) peak as the protection group is removed, while the nitrogen peak of the amine is not affected.

The next step in the protein attachment process was to add a carboxyl group at the primary amine, the activation of this carboxyl group and the binding of crosslinkers. Then the proteins can be attached to the functionalized diamond surface.

First we attached the green fluorescent protein (GFP); it contains a chromophore which absorbs blue light (maxima at 395 nm and 470 nm) and reemits it as green fluorescence (maximum at 509 nm). The protein functionalized diamond samples were measured with a fluorescence microscope, equipped with the matching optical filters to excite the protein with blue light and detect only the green fluorescence emission light. Even after strong cleaning, a fluorescence signal was detected (Fig. 1). This provides clear evidence that the proteins are not just physisorbed, but covalently bound to the diamond surface. The dark regions in Fig. 1 correspond to the surface areas which were oxidized initially. Therefore, the photochemical treatment described above is not expected to function at those regions. In accordance, a fluorescence signal from GFP is only observed in the formerly hydrogenated surface area where the amine groups were anchored.

[1] phone:+49-89-289-12768, fax:+49-89-289-12737, email: haertl@wsi.tum.de

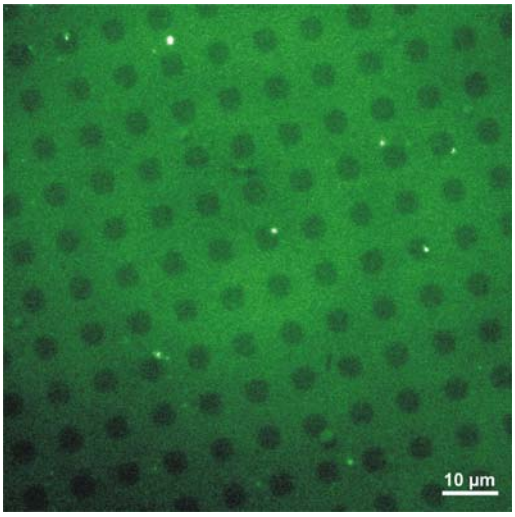

Fig. 1: *Fluorescence image of a nanocrystalline diamond sample patterned by oxidation and functionalized with green fluorescent protein.*

We have also shown that diamond does not just provide the possibility of covalent protein attachment, but also acts as a biocompatible substrate suitable for protein electrochemistry. For this purpose the enzyme catalase was used. Instead of the photolithographic pattern described above, an electrode device was fabricated on top of the completely hydrogenated nanocrystalline diamond. Two small Ti/Au contacts were evaporated, and the area between them isolated from the rest of the sample by oxidation. Subsequently, these samples were photo-chemically treated as described above. Instead of GFP, catalase was bound to the surface. After the functionalization, the metal contacts were covered with a chemically resistant silicone glue, to expose only the functionalized area between them to the electrolyte for electrochemical measurements. We used an electrochemical cell consisting of an Ag/AgCl reference electrode, a Pt counter electrode, the diamond sample as the working electrode, and a potentiostat to control the electrolyte potential. The measurements were carried out in an aqueous KCl-based phosphate buffer. Fig. 2 shows the current voltage curves for an unmodified (1) and a catalase-modified (2) NCD electrode measured at a scan rate of 5 mV/s. Characteristic redox peaks (cathodic peak at 0 V and the anodic one at +0.15 V), associated with the direct electrochemistry of the heme group of the catalase, are observed only in the enzyme-functionalized electrode. The catalase heme group consists of a protoporphyrine ring with a central iron atom which acts as a redox couple by switching its charge state between Fe^{2+} and Fe^{3+}. The observed peaks are related to the oxidation and reduction of the iron ion, confirming that the immobilized enzyme maintains its electrochemical activity. Another cathodic peak was observed at about -0.25 V, which is attributed to the catalytic reduction of O_2 by the enzyme catalase, since O_2 is normally present in a non degased electrolyte solution.

With an appropriate storage conditions the functionalization has shown to be stable for at least 8 weeks.

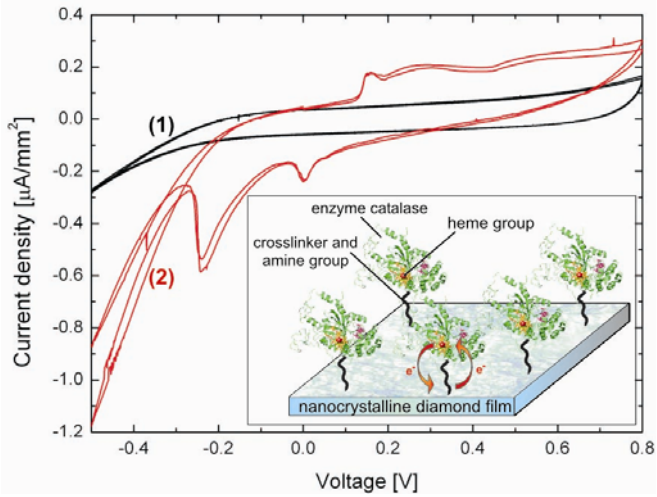

Fig. 2: *Cyclic voltammograms of an untreated NCD electrode (1) and a catalase-modified NCD electrode (2), measured in buffer solution. The inset shows a schematic view direct electron transfer between the diamond electrode and the heme group of the catalase.*

---

in collaboration with Silvia C. R. Catharino and Stefan Walter (Institute for Organic Chemistry and Biochemistry, TU München), and Peter Feulner (Physics Department E20, TU München)

High-temperature (490 K) operation of InP-based quantum cascade lasers with InP/GaInAs waveguides

Andrea Friedrich[1], Giuseppe Scarpa, Gerhard Böhm, and Markus-Christian Amann

Quantum cascade lasers (QCLs) are among the most promising light sources in the mid- and far-infrared spectral region for applications based on absorption lines of gas molecules and atmospheric transmission windows. A considerable level of performance has been reached, such as very high peak output power levels in the Watt range and high temperature operation in pulsed mode as well as continuous wave operation slightly above room-temperature.

A crucial point in the design of high-quality QCLs is the reduction of the waveguide losses. Former samples were grown with GaInAs as cladding layer material. Making use of InP as a cladding layer an improved waveguide design has been developed. Besides the higher thermal conductivity, the relevant advantage of InP over GaInAs is its lower refractive index. Incorporating a 2 µm thick InP-cladding layer, a better confinement and lower internal losses have thus been achieved. Fig. 1 shows the TM-modes and the refractive index profiles of two samples which are referred to as sample A and B. The active region is the same for both structures, but the waveguide design of sample B has been improved. Generally a strong decrease of the refractive index enhances the confinement factor of the mode. Designing waveguides with only GaInAs, one can take advantage of the abnormality of the refractive index in highly doped layers, but along with the reduction of the refractive index goes a strong increase in the absorption. Therefore, to reduce the optical losses, in sample B a thick, low doped InP-layer with small losses, has been included. For both structures the top cladding is made by a (GaInAs) plasmon waveguide layer. Again the decrease of the refractive index enhances the confinement factor of the mode and also suppresses the mode penetration into the contact region. The calculated values of the free carrier absorption losses and the TM-mode confinement factor are $\alpha_w = 6.5$ cm^{-1} and $\Gamma_{AR} = 47.6$ % for sample A and $\alpha_w = 3.1$ cm^{-1} and $\Gamma_{AR} = 62.5$ % for sample B.

After growth, ridge-waveguide lasers were fabricated from sample B by conventional photolithography and nonselective wet chemical etching using a $HBr:H_2O_2:H_2O$ solution. After evaporation of Ti/Pt/Au contacts the wafer was thinned to 120 µm and a Ge/Au/Ni/Au bottom-contact metallization was made.

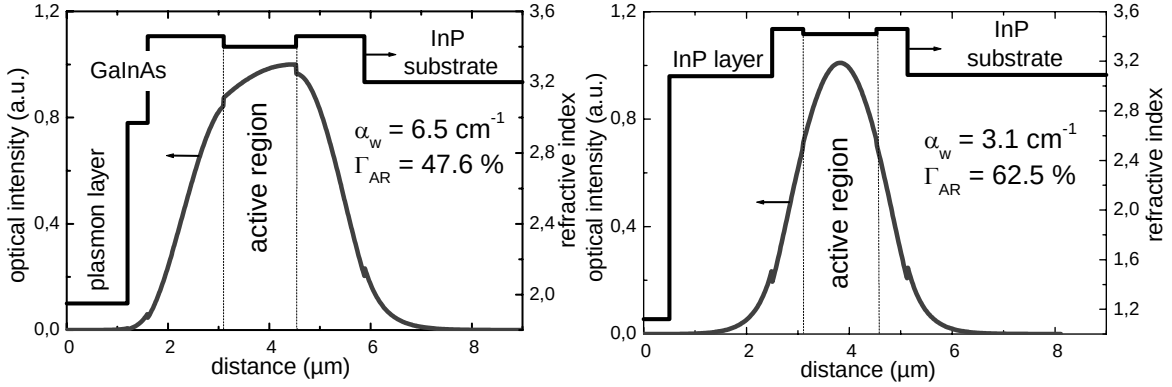

Fig. 1: *TM-modes and refractive index profiles of the samples A and B. The calculated optical losses at room temperature and the confinement factors are also indicated.*

[1]phone:+49-89-289-12767, fax:+49-89-3206620, email: friedrich@wsi.tum.de

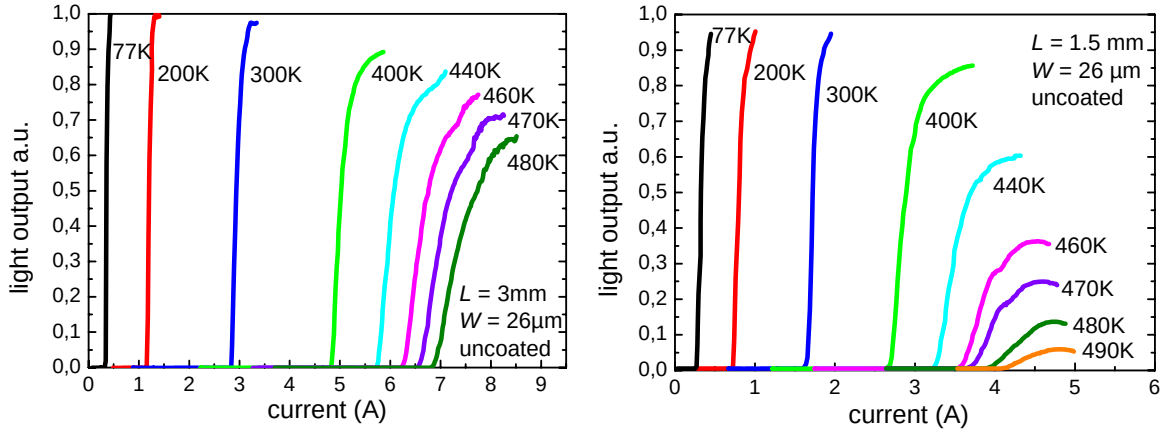

Fig. 2: *Pulsed (τ = 250 ns, f = 250 Hz) light output of uncoated quantum cascade lasers (sample B) at various heat sink temperatures*

A 250 nm thick SiO_2 layer was used as insulation. All devices were mounted ridge-side up on copper heat sinks and contacted by wire bonding.

Typical pulsed light output-current (*P-I*) characteristics of uncoated devices from sample B with 26 µm width and 3 mm or 1.5 mm cavity length are shown in Fig. 2. The applied pulse width was 250 ns and the repetition frequency 250 Hz. At 300 K the emission wavelength was about 5.8 µm. The lasers work up to the record high heat sink temperature of 480 K and 490 K (~ 220 °C) respectively. Note that the maximum operation temperature here is setup-limited because of melting of the for contacting needed tin-solder at heat sink temperatures of 490 to 495 K. Previous samples with GaInAs waveguides (sample A, Fig. 1) worked up to 450 K without and 470 K with high-reflection (HR) coating.

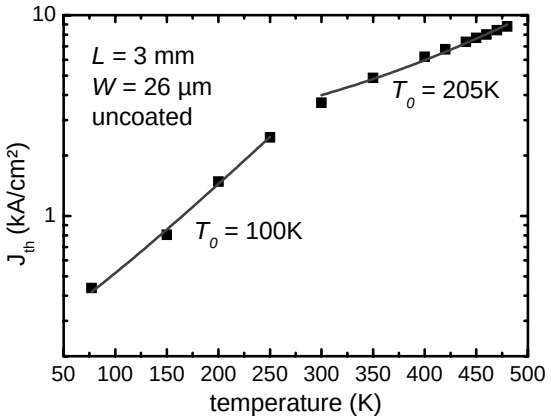

Fig. 3: *Threshold current density vs. heat sink temperature*

A plot of the threshold current density at various heat sink temperatures for an uncoated 3 mm long and 26 µm wide representative device of sample B is shown in Fig. 3. Low threshold current densities of 0.44 kA/cm^2 and 3.65 kA/cm^2 at 77 K and 300 K respectively, have been obtained. Devices of 2.5 mm cavity length and 30 µm width without InP-cladding (sample A) showed best values like 1kA/cm^2 at 77K and 4.2 kA/cm^2 at 300K. The exponential fit curves for the determination of T_0 in two temperature ranges are also displayed.

HR coated laser devices were also tested. The maximum operation temperature in pulsed mode again was 480 K. Low threshold current densities like 0.15 kA/cm^2 at 77 K and 2.47 kA/cm^2 at 300 K have been achieved for a 26 µm wide and 2 mm long device. Compared to a device of same width and length from sample A, the threshold has been reduced by 84 % at 77K and 35 % at 300K.

In conclusion, we have fabricated high-performance InP-based QC lasers using InP and GaInAs as cladding materials, with low threshold current densities and record high operation temperatures.

Room temperature continuous-wave GaInAsSb-AlGaAsSb lasers in the 2.2 to 3 µm wavelength range

Markus Grau[1], Chun Lin, Oliver Dier, and Markus-Christian Amann

In recent years there have been considerable research efforts to realise mid-infrared lasers. The applications of such lasers are found in the fields of molecular spectroscopy, pollution monitoring or medical diagnostics. For these applications, room temperature continuous-wave operation is important.

The GaInAsSb material system can principally cover a broad wavelength range from 1.7 to 4.3 µm, where many gas absorption lines exist. However, lasers with GaInAsSb quantum wells so far have only shown room temperature continuous-wave operation up to 2.8 µm. A problem of using GaInAsSb for long wavelengths is that due to an increased Indium concentration the band alignment between the GaInAsSb quantum wells and the AlGaAsSb barriers switches from type-I to type-II. In case of a small type-I-, or even worse, a type-II-offset, the hole leakage is increased and the wave function overlap is deteriorated.

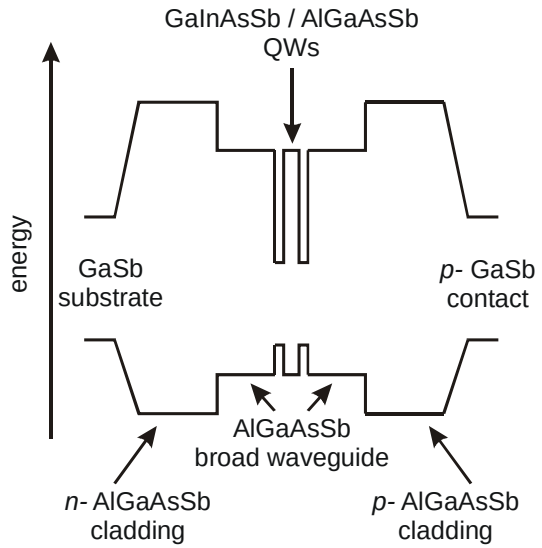

Fig. 1: *Bandstructure of GaInAsSb-AlGaAsSb lasers on GaSb substrate.*

We present GaInAsSb-AlGaAsSb lasers in the wavelength range from 2.2 to 3 µm with the first demonstration of room temperature continuous-wave operation at 3 µm. The lasers were grown by molecular beam epitaxy on GaSb wafers and comprise an undoped active region between two AlGaAsSb cladding layers. The active region consists of an AlGaAsSb broad waveguide structure and GaInAsSb-AlGaAsSb quantum wells. A schematic bandstructure of our lasers is shown in figure 1.

In order to preserve a type-I alignment between the quantum wells and the barriers, we adjusted the strain in the quantum wells: For 3 µm lasers we used heavily (1.5%) compressively strained $Ga_{0.50}In_{0.50}As_{0.23}Sb_{0.77}$. In order to achieve long emission wavelength and at the same time keep the Indium concentration as low as possible, we used 20 nm wide quantum wells to minimise the quantisation energy for all lasers above 2.7 µm wavelength.

For the highly strained quantum well material used in our lasers, the possibility of relaxation has to be considered, especially because of the rather large thickness of the long wavelength quantum wells. Therefore a maximum of only two quantum wells is feasible for these highly strained active regions. For lasers with lower strain and thinner GaInAsSb layers, we used three quantum wells.

[1]phone:+49-89-289-12759, fax:+49-89-320 6620, email: markus.grau@wsi.tum.de

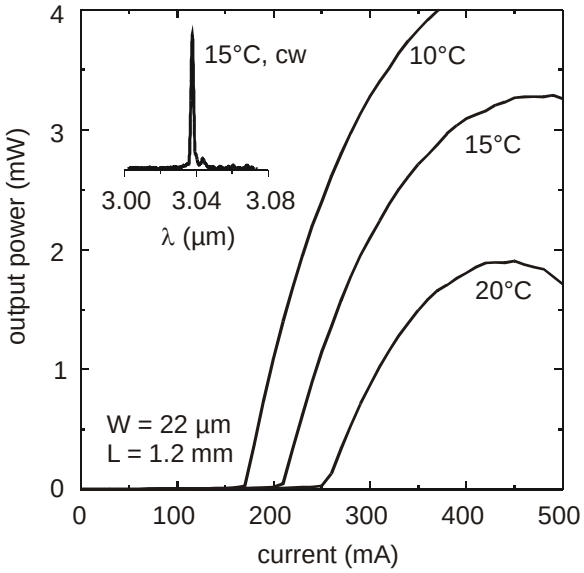

Fig. 2: *Output power against current characteristics for continuous-wave operation of a 1.2 mm device with 22 µm stripe width. Inset: Emission spectrum at 15 °C.*

The devices were processed to ridge waveguide lasers and mounted on copper heat sinks for characterisation. Figure 2 shows output power versus current characteristics of lasers with 3 µm wavelength. For a device with 22 µm stripe width and 1.2 mm cavity length the maximum continuous-wave operation temperature is 20°C. At this temperature the threshold current density is 947 A/cm^2. The threshold current density shows strong temperature dependence: At 0°C we found only 489 A/cm^2. A typical spectrum of these lasers can be seen in the inset of figure 2: In continuous-wave operation at 15°C the emission wavelength of the lasers is 3.04 µm.

Pulsed (200 ns @ 20 kHz) operation was observed up to 40°C for the 3 µm lasers. For this operation mode, an extrapolation of the threshold current density for infinite cavity length shows a low $J_{th,\infty}$ of 232 A/cm^2 (116 A/cm^2 per quantum well).

The wavelength dependence of the threshold current density per quantum well and the characteristic temperature are depicted in figure 3. All lasers have the same stripe width (30 µm) and cavity length (2 mm). For lasers with 2.2 µm wavelength $J_{th,\infty}$ per quantum well is only 56 A/cm^2. With increasing wavelength, this value rises to 172 A/cm^2. Simultaneously the characteristic temperature decreases strongly from very high 140 K to low 30 K. Possible reasons for this behaviour are free carrier absorption, intervalence band absorption and Auger recombination.

In conclusion we presented room temperature GaInAsSb-AlGaAsSb lasers in the wavelength range between 2.2 and 3 µm. Long wavelength emission has been realised by using highly strained GaInAsSb quantum wells. All lasers exhibit continuous-wave operation and show low threshold current densities even at long wavelength.

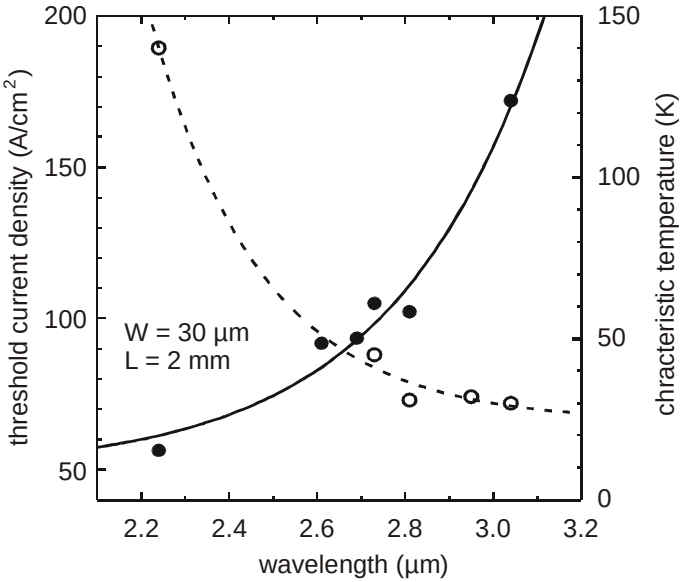

Fig. 3: *Threshold current density per quantum well for infinite cavity length and characteristic temperature against wavelength for pulsed operation.*

supported by BMBF (Materialien für Infrarotkonverter)

InP-based vertical-cavity surface-emitting lasers at 1.55µm emission wavelength with ultra-low series resistance

Christian Lauer[1], Markus Ortsiefer, Robert Shau, Gerhard Böhm, Markus Maute, Fabian Köhler, and Markus-Christian Amann

GaAs-based vertical-cavity surface-emitting lasers (VCSELs) are commercially available for emission wavelengths in the range of 850 nm and with InGaAsN active regions up to 1300 nm. The InP-based VCSEL structure with buried tunnel junction (BTJ) developed by our group as shown in fig. 1a is able to cover the wavelength range from 1.3 µm up to 2 µm. Lasers at 1.55 µm are key components for telecommunication and data transmission systems with link lengths exceeding 1000 m utilizing the damping minimum of standard fused silica fibers. Unfortunately, the modulation frequency of the devices is limited due to a large parasitic capacitance *C* introduced by the contact pads. With the series resistance *R*

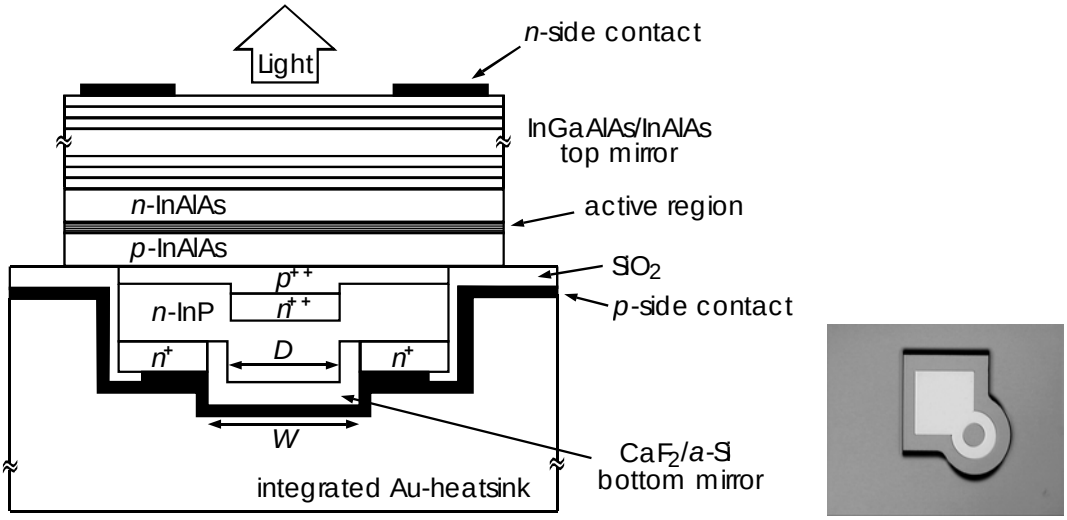

Fig. 1: *(a) Cross-sectional view of the InP-based VCSEL structure. (b) Small contact pad, the circular cutout provides access to the output mirror.*

this leads to a *RC* low-pass filter for the modulated driving signal with large *RC*-product and consequently low cut-off frequency. Typically, *R* is of the order of 100-200 Ω in commercial 1300 nm-VCSELs. The parasitic capacitance can be kept small by the use of large passivation layer thickness and small contact pads (see fig. 1b), but shrinkage is limited by the space needed for soldering of the bond wire.

Current is injected through the ring contact around the insulating dielectric mirror into the thin current spreader layer of regrown *n*-InP (see fig. 1a), flows toward the buried tunnel junction aperture, and through the *n*-doped top mirror. The contribution of the upper epitaxial mirror to the series resistance of the device is reduced to about 1 Ω by the use of short-period superlattices at the interfaces of the λ/4-layers. Therefore, the series resistance mainly consists of the resistance of the thin *n*-InP layer R_{InP} and the tunnel junction R_{BTJ}, approximate values for the lower boundaries can be calculated using the expressions

$$R_{InP} = \frac{4\times10^{15}\,\Omega\mathrm{cm}^{-2}}{2\pi\cdot d\cdot N_D}\cdot\ln\left(\frac{W}{D}\right), \qquad R_{BTJ} = \frac{4}{\pi}\cdot\frac{\rho_{c,BTJ}}{D^2},$$

[1]phone:+49-89-289-12788, fax:+49-89-3206620, email: christian.lauer@wsi.tum.de

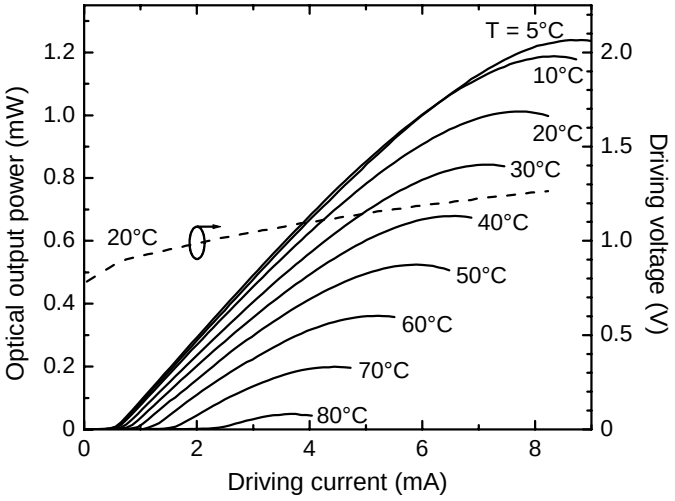

Fig. 2: *L-I characteristics for several heat sink temperatures (solid lines) and V-I curve for room temperature (dashed line) for a device with D = 3.5µm and regrowth thickness of 900 nm.*

with the donor concentration N_D and thickness d of the InP-layer, the diameters of the dielectric Bragg reflector W and the tunnel junction aperture D, and the contact resistivity of the tunnel junction $\rho_{c,BTJ} \approx 2 \times 10^{-6}$ Ωcm^2. The thickness d influences the oscillation phase condition, allowed values at 1.55 µm emission wavelength are 100 nm, 350 nm, 600 nm, etc. Recently we were able to increase the regrowth thickness while retaining good surface quality from the initial 100 nm to up to 1100 nm, significantly reducing the electrical series resistance of the InP spreader layer (54 Ω for d = 100 nm). We fabricated a device with a regrowth thickness d = 900 nm (slightly off the intended 850 nm), doping concentration $N_D = 1.8 \times 10^{18}$ cm^{-3}, D = 3.5 µm, and W = 16 µm. Thus the contributions of the InP layer and the tunnel junction are 6 Ω and 21 Ω, respectively, leading to an anticipated device resistance of only $R_S \approx 28$ Ω. Figure 2 shows *L-I* and *V-I* characteristics and the output spectrum of the device. It exhibits single-mode emission with output powers exceeding 1.2 mW at a heat sink temperature of 5°C, 1 mW at room temperature, and shows laser action up to 80°C. The minimum of the threshold current with 0.53 mA is found at room temperature and indicates a well-designed laser structure. This value corresponds to a threshold current density of about 1600 kA/cm^2 if an outward diffusion of estimated 3 µm in diameter of the carriers in the active region is taken into account. The differential quantum efficiency at threshold reaches 25%. Due to additional voltage drop over layers and interfaces not taken into account the differential series resistance is slightly larger than the anticipated value and amounts to 34 Ω.

Previously fabricated devices of comparable size with a regrowth thickness of 350 nm showed series resistances of over 60 Ω and cw-output powers at room temperature of 0.8 mW. The reduced series resistance in the new device leads to less heat generation inside the device and increased output power, see fig. 3. Together with thicker passivation layers made of BCB the direct modulation bandwidth is also expected to increase.

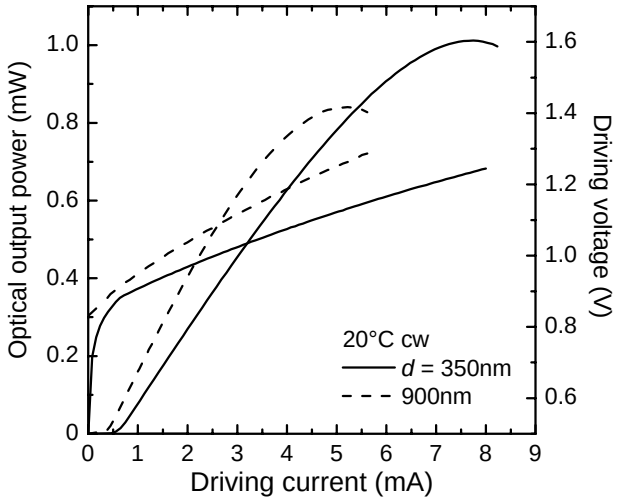

Fig. 3: *Comparison between a device with a regrowth thickness of 900 nm (solid lines) and 350 nm (dashed lines).*

supported by DFG (**STU 139/8-1**, SFB 348 (B15))

Micro-mechanically tunable long wavelength VCSEL

M. Maute[1], F. Riemenschneider[2], G. Böhm, P. Meissner[2], and M.-C. Amann

Widely tunable long-wavelength vertical-cavity surface-emitting lasers (VCSELs) are highly attractive light sources for telecom applications within Dense-Wavelength-Division-Multiplexing (DWDM) systems. Fixed wavelength laser replacement, single transverse-mode operation with high side mode suppression, and high coupling efficiency into an optical fiber are some of the main benefits of those devices. Various monolithic concepts of micro-electro-mechanically tunable VCSELs have been presented to date. Here we investigate a new approach based on a two-chip concept that allows for a separate optimization of the components: The device (see Fig. 1) consists of a "half-VCSEL" and a movable top mirror membrane. The active part of the device is very similar to the design of the long-wavelength VCSEL that has been developed at the WSI during the last few years (see report by C. Lauer) except that the epitaxial front mirror has been omitted. The current confinement in this structure is realized by the use of a buried tunnel junction (BTJ) of a given diameter D and the back reflector is formed by a dielectric mirror. Since the membrane is much bigger in size compared to the half VCSEL a Silicon-submount is used. The micro-mechanically tunable mirror is an MBE-grown $(In_{0.03})GaAs/AlGaAs$-Bragg-mirror of about 24.5 periods leading to a very high theoretical reflectivity of 99.95%. After defining the shape of the membrane and partial removal of the semi-insulating GaAs substrate the additional 3% Indium content in some of the GaAs-layers leads to a stress-gradient and therefore to a rotation-symmetric concave curvature with a radius of about 1 to 7mm. Due to this curvature the necessary assembling step of mirror and active part is rather insensitive to tilt and the variable air-gap is formed without the need for additional spacing elements. Deflection of the membrane, i.e. wavelength tuning, can be achieved by electro-thermal heating of the thin suspension beams by injecting a small current using the via-hole contacts through the substrate (see Fig. 1). A picture of a packaged tunable VCSEL is shown in Fig. 2

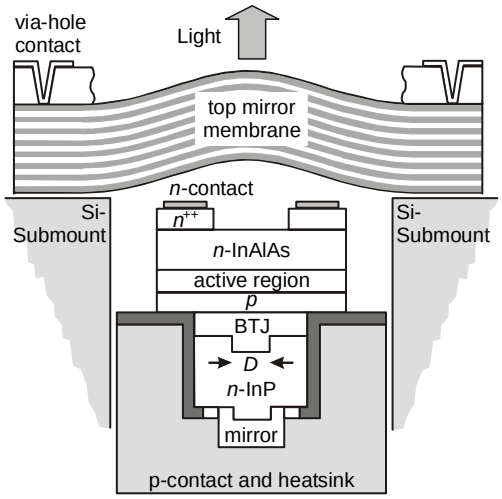

Fig. 1:
Schematic cross section of tunable two-chip VCSEL.

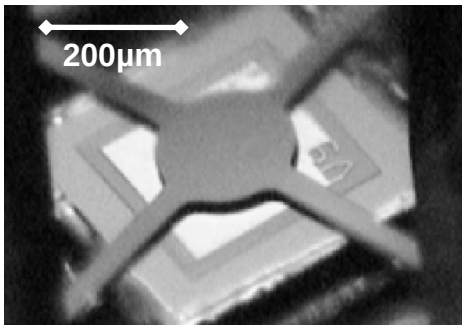

Fig. 2:
Top view of a packaged tunable VCSEL. The round mirror membrane with its four suspension beams can be seen placed above a half VCSEL.

[1]phone:+49-89-289-12786, fax:++49-89-320-6620, email: maute@wsi.tum.de
[2]Institute of Microwave Engineering, Darmstadt University of Technology, 64283 Darmstadt

Devices with a current aperture of D = 7µm and 20µm were investigated showing room temperature operation in cw-mode. A typical light-current-voltage (*L-I-V*) curve at a wavelength of around 1595nm is shown in Fig. 3. As can be seen, the maximum fiber coupled output power is about 80µW at the thermal rollover reached at a current of 8mA. The threshold condition is reached at a current density of 10kA/cm^2 at a voltage of 1.1V. The highest power observed in free space was found to be about 300µW for a 20µm-BTJ device (not shown here). Typical tuning spectra are shown in Fig. 4 revealing a very good side mode suppression ratio (SSR) of up to 49dB and a tuning range of 40nm. Taking a SSR of at least 30dB as the criteria for single mode operation, a record continuous tuning range of 30nm has been achieved for an electrically pumped long wavelength VCSEL.

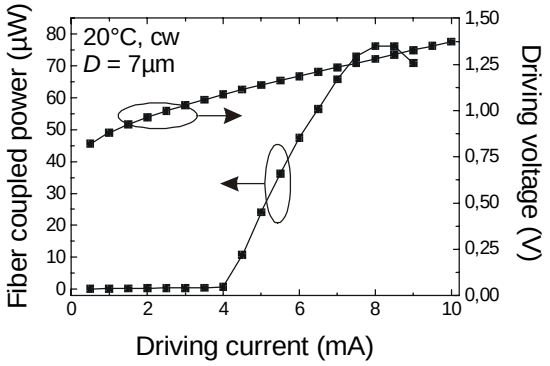

Fig. 3:
Typical L-I-V characteristics for a tunable VCSEL with a 7µm-BTJ at a wavelength of 1595nm.

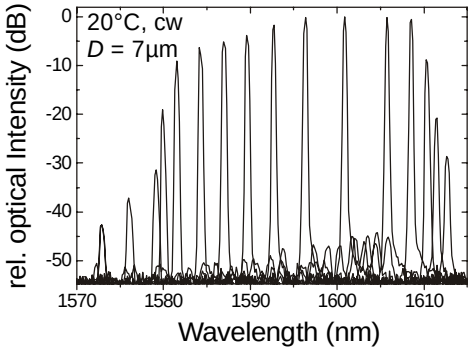

Fig. 4:
Several spectra for different membrane deflection.

While for non-tunable VCSELs single-mode operation can only be observed up to an aperture of D = 4 to 5µm emission in the fundamental mode can be achieved for the tunable device even for a BTJ of 20µm in diameter. This is due to the fact that in a plane-concave cavity the fundamental mode is well defined and can be controlled by the shape of the top mirror. Since the membrane deflection is realized by electro-thermal heating the observed shift of the resonance wavelength is proportional to the dissipated power, i.e. to the square of the tuning current as can be seen in Fig. 5. In conclusion we have shown the largest tuning range for an electrically pumped VCSEL emitting in the 1.5µm wavelength range by applying a two-chip concept. The devices show good side mode suppression and we expect to increase the output power considerably by an optimized adjustment of the resonator geometry.

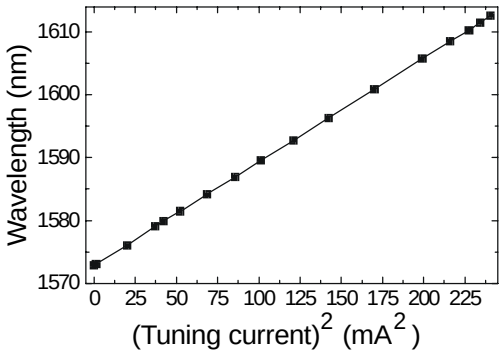

Fig. 5:
Resonance wavelength as a function of tuning current squared.

supported by the Federal Ministry of Education and Research, Germany (BMBF)

Widely tunable twin-guide laser diodes

René Todt[1], Thomas Jacke, and Markus-Christian Amann

Wavelength-tunable laser diodes are receiving much attention in recent years since they are expected to become essential for various telecom applications. In the short run, they are most likely to be used as backups for conventional fixed-wavelength transmitters. However, in the long run they will become enabling key components for future generation optical networks. Besides this, tunable lasers are also highly attractive light sources for fibre Bragg grating based sensor devices and gas sensing applications.

Although there are already several types of monolithically integrated tunable laser diodes available, practically all of them suffer from various shortcomings. For example, a common issue is the device calibration, which is rather time-consuming, since typically three tuning currents are required to set the emission wavelength.

Only recently a novel, so-called sampled or superstructure grating tunable twin-guide ((S)SG-TTG) laser has been proposed. This device requires only two tuning currents and, therefore, very efficient device calibration seems viable. Moreover, with the structure being similar to a DFB laser, high side-mode suppression as well as high output powers are expected.

The device structure is based on the DFB-TTG laser that has been invented several years ago. The aforementioned TTG laser is essentially a DFB laser with transversally integrated tuning diode, which is used to change the effective refractive index and, hence, to tune the emission wavelength.

A schematic drawing of the longitudinal cross-section of an (S)SG-TTG laser is shown in Fig. 1. The tuning region is split into two parts, and the DFB grating is replaced by sampled or superstructure gratings of different periods ($\Lambda_{S1} \neq \Lambda_{S2}$). Each tuning section provides a comb-like reflection spectrum of different peak spacing and, thus, Vernier-effect tuning can be employed to achieve wide tunability.

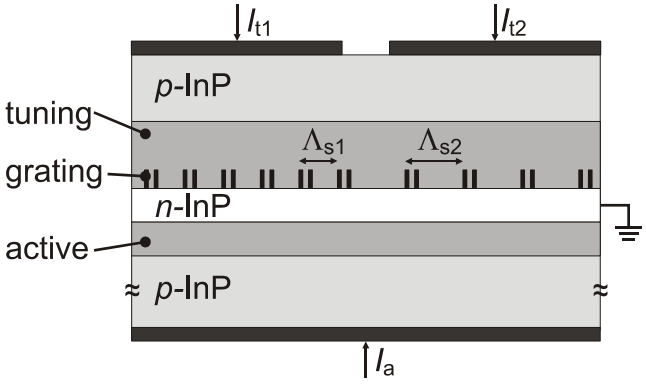

Fig. 1:
Schematic drawing of the longitudinal cross-section of a widely tunable (S)SG-TTG laser diode.

The laser structures are based on the GaInAsP-InP material system and were fabricated in four epitaxial growth steps in a chemical beam epitaxy (CBE) system. The active region consists of an SL-MQW with emission wavelength around 1.55 μm, and the tuning region is formed by a bulk GaInAsP layer (λ_g = 1.34 μm). Sampling and superstructure periods were chosen to obtain reflection peak spacings between 4.8 and 6.2 nm.

[1]phone:+49-89-289-12767, fax:+49-89-320-6620, email: todt@wsi.tum.de

After fabrication, 600 μm long devices have been cleaved. The facets were left uncoated. For 1.3 µm broad devices with sampled gratings, the lasing threshold was reached at a current of 10 mA. Fibre-coupled output powers of as much as 4.5 mW (at active region currents of 100 mA) were observed.

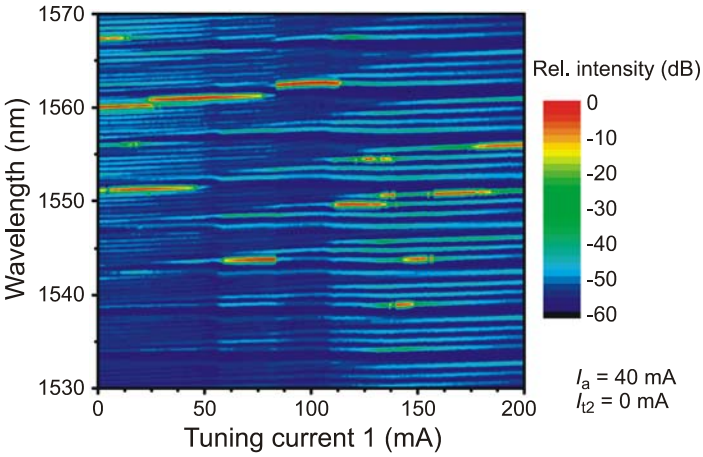

Fig. 2:
Evolution of the optical emission spectrum while tuning only section 1 and leaving section 2 unbiased.
A wavelength range of about 30 nm can be covered by this laser.

Fig. 2 shows the evolution of the emission spectrum while tuning only the front tuning section (I_{t1}). The rear tuning section (I_{t2}) was left unbiased during this measurement. Although one can see some irregular behaviour, especially at low tuning currents, the expected step-like behaviour can be clearly observed at high tuning currents. The irregularities in the tuning behaviour are believed to be caused by interference effects of grating and facet reflections since an AR-coating has not yet been applied.

By using also the rear tuning section, a wavelength range of about 30 nm can be accessed by this device. The side-mode suppression is typically in excess of 27 dB, with best values of around 45 dB.

The optical emission spectrum at a tuning current of 100 mA is shown in Fig. 3. As can be seen, the side mode suppression is not limited by the cavity mode spacing but by the reflections from neighbouring reflection peaks, which is typical for widely tunable lasers.

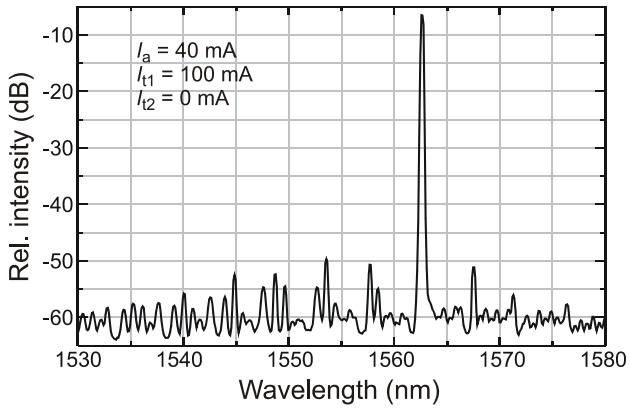

Fig. 3:
Optical emission spectrum at a tuning current of I_{t1} = 100 mA.

In conclusion, we have demonstrated the first widely tunable twin-guide laser diodes. A tuning range of 30 nm has been achieved along with high side-mode suppression and high output-powers.

supported by the EU via the IST-project IST-2000-28244 “NEWTON”

InP-based buried heterostructure lasers with vertically integrated Mach-Zehnder interferometer (VMZ)

Thomas Jacke[1], René Todt, Gerhard Rösel, and M.-C. Amann

Wavelength-agile single-frequency laser diodes have attracted much attention in recent years because of their suitability for wavelength division multiplexing (WDM) applications. The laser type presented here has the advantage of compactness and simplicity: the wavelength is controlled by one current only and the discrete output spectrum exhibits an appropriate mode spacing defined by the resonator length L_{cav}. In contrast to previously realized VMZ-lasers, the active layer and the tuning layer are incorporated in different waveguides leading to a larger tuning range. Similar to other tunable lasers, the performance of realized devices is limited mainly by leakage currents. Therefore, the loss mechanisms occurring at growth interfaces in chemical beam epitaxy (CBE) have been investigated in detail.

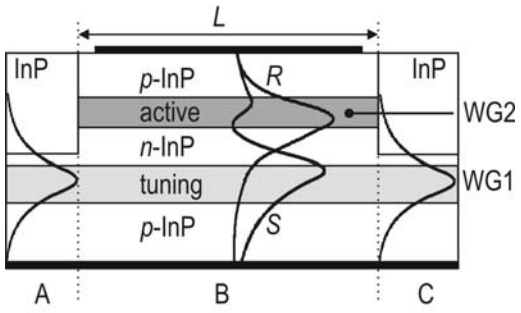

Fig. 1: *Schematic view of the longitudinal section*

A schematic view of the VMZ laser is shown in Fig. 1. In addition to a simple Fabry-Pérot type laser, a twin-waveguide section (length L) with two guided modes is inserted in the resonator. The single-waveguide (section A and C) at the laser's facets provides for laser emission in the transverse fundamental mode. The double waveguide section B represents a Mach-Zehnder interferometer that acts as a wavelength tunable filtering element. The filter has maximal transmission at wavelengths that fulfill the condition for constructive interference of modes R and S at the coupling planes A/B and B/C. This implies the filter's transmission maxima to be located at $\lambda_0 = \Delta n\, L / N$ (N being an integer, the effective refractive index difference of the two modes is Δn). The best selectivity of the filter is obtained for equal mode amplitudes in each interferometer arm (amplitude matching condition).

The tuning is accomplished by injection of carriers in one interferometer arm (tuning layer) enabling a controlled change of Δn. Typically, a maximum refractive index change of -0.04 can be achieved in this way. Calculations using the effective index method show that a maximum wavelength shift of 80nm can be expected with the present structure.

The independent control of the two heterojunction diodes requires three independent contacts to be integrated. Typically for vertically integrated tunable devices, holes are injected transversely by the bottom and top p-contacts, whereas the electron injection has to be provided by the lateral design.

The processing of the devices with lateral *n*-contacts is similar to the tunable twin guide (TTG) laser process. In a first epitaxial step, the InGaAsP double heterostructures are grown by CBE. The definition of the lateral and longitudinal mesa and the interferometer is

[1] phone:+49-89-289-12785, fax:+49-89- 3206620, email: jacke@wsi.tum.de

carried out by plasma etching followed by an embedding overgrowth step with *n*-InP using CBE. The quality of these interfaces has great impact on the laser performance since bad interface quality can significantly increase the leakage currents. This limits the maximum carrier density in the double heterostructures, and, additionally, the generated heating lowers the refractive index change induced by the plasma effect. The two dominant leakage current mechanisms are losses through the forward-biased *pn*-junctions and non-radiative recombination in the low bandgap material. In particular the *pn*-junction loss is very sensitive to the overgrowth step because this junction coincides with the epitaxial interface where impurities, acting as efficient recombination centers, are incorporated.

To study the effect of interface quality on the diode current characteristics, nominally identical *pn*-diodes with different surface treatments have been grown (Fig. 2): The samples with one epitaxial step are quite close to the expected theoretical curve (a), although, the in-situ growth interruption leads to a current increase by a factor of three and the ideality factor increases slightly from 1.1 to 1.2. An optimized cleaning and deoxidation procedure after the regular process has been applied to sample (d) which shows an improvement of two orders of magnitude in the current in comparison to the previous procedure (sample (e)). The higher ideality factor of 1.8 and 2.0 for samples (d) and (e), respectively, evidences the increased recombination rate at the interface.

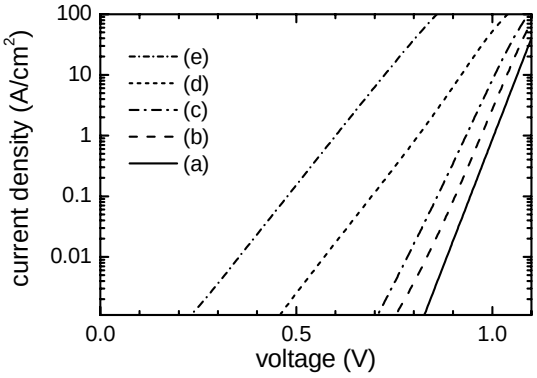

***Fig. 2**: JV-curves of* pn-*diodes with different epitaxial interfaces: (a) calculated drift-diffusion current, (b) one step epitaxy, (c) in situ growth interruption for 20min, (d) processed with optimized surface treatment, (e) non appropriate surface treatment.*

The non radiative recombination current at the mesa edges gives rise to an area-independent contribution to the laser and tuning diode current and is attributed to crystal damage caused by plasma etching. A simple HCl-Dip proved to be insufficient to remove these crystal defects. This leakage current path could be greatly reduced by a HBr:H_2O_2 – based solution removing uniformly about 30nm of the damaged surface material.

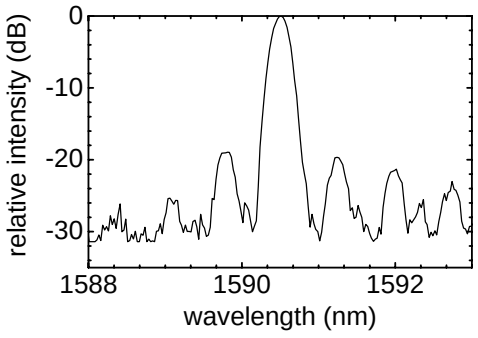

***Fig. 3:** Measured laser spectrum at 300K. The SSR is about 20dB.*

In Fig. 4 the emission laser spectrum of an VMZ-laser is presented. The resonator and interferometer lengths are about 500µm and 450µm, respectively. Besides the filtering effect also the periodicity of the filter function could be observed: By lowering the temperature by about 10K the gain spectrum exhibits a blue-shift of about 5nm. At this lower temperature the laser showed a similar emission spectrum, however, centered at 1560nm. Within the measurement accuracy this is in quite good agreement with the numerical results.

Design and fabrication of InAlAs/InGaAs heterojunction bipolar transistors

Rajendra Singh, Markus Krach[1], Jürgen Freyer, and Gerhard Böhm

InP-based heterojunction bipolar transistors (HBTs) are one of the best candidates for ultra high frequency analog, digital and mixed signal integrated circuits due to their inherent material properties. In order to increase both, the maximum frequency of oscillation f_{max} and the unity gain cutoff frequency f_t, for npn transistors, it is required that the *p*-type dopant concentration in the base be optimized and confined within the base layer. In the present work, the DC electrical performance of InAlAs/InGaAs HBTs having either beryllium (Be) or carbon (C) as *p*-type dopants in the base has been studied.

The $In_{0.52}Al_{0.48}As/In_{0.53}Ga_{0.47}As$ material system has been used for the fabrication of HBTs. The epitaxial layers are grown lattice-matched on semi-insulating InP(100) substrates using MBE technique. The epitaxial layer structure is comprised of a 1000 nm InGaAs:Si subcollector layer doped at 5×10^{19} cm^{-3}, a 700 nm InGaAs:Si collector layer doped at 1×10^{16} cm^{-3}, a 80 nm InGaAs:Be or C base layer doped at 5×10^{19} cm^{-3}, a 100 nm InAlAs:Si emitter layer doped at 5×10^{17} cm^{-3}, a 45 nm InAlAs:Si emitter cap layer doped at 5×10^{19} cm^{-3}, and a 75 nm InGaAs:Si emitter cap layer doped at 5×10^{19} cm^{-3}.

The approach used to fabricate the transistors is a self-aligned triple-mesa etch process. Standard photolithography and wet chemical etchants have been used to fabricate test devices with dimensions ranging from 20×20 μm^2 to 50×50 μm^2. E-beam evaporated Ti/Au layers (20 nm/200 nm) are used for ohmic contacts to the emitter cap, base and subcollector. The individual metal contacts serve as etch masks for the wet chemical etching of the corresponding mesa structures.

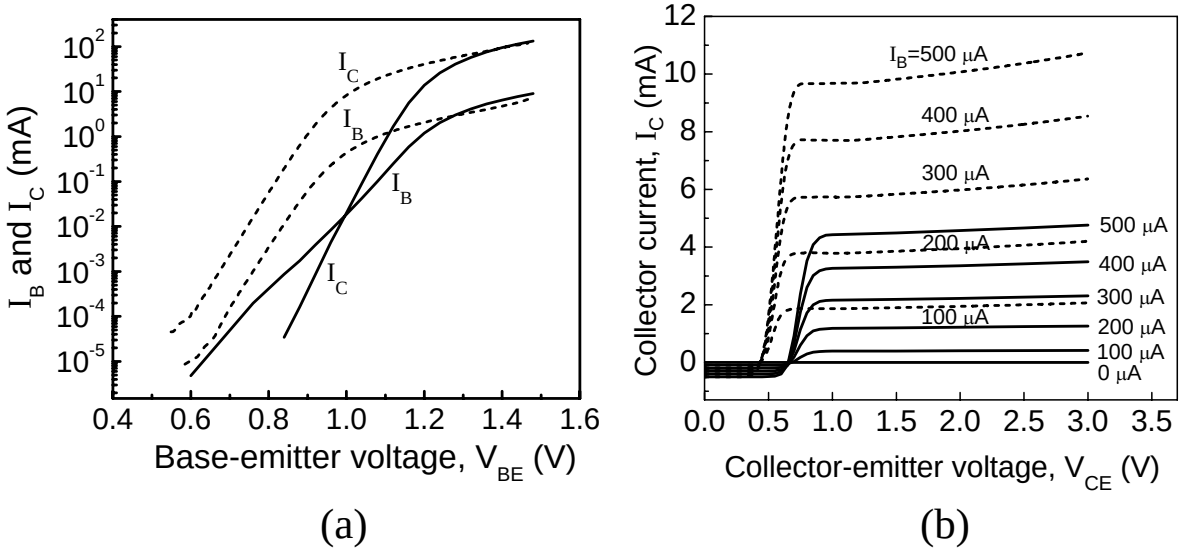

Fig. 1: *(a) Gummel plots and (b) common-emitter output characteristics for Be-doped (solid curves) and C-doped (dash curves) base InAlAs/InGaAs HBTs with emitter dimensions of 50×50 μm^2.*

[1]phone: +49-89-289-12787, fax: +49-89-320 6620, e-mail: markus.krach@wsi.tum.de

The Gummel plots and output characteristics for the HBTs having Be (solid curves) and C (dashed curves) as *p*-type base dopants are shown in Fig. 1a and 1b, respectively. The current gain β, the ideality factor for the base current n_B and the offset voltage for Be-doped HBTs are 15, 2.05 and 0.65 V, respectively, while that for C-doped HBTs are 20, 1.29 and 0.45 V, respectively. Hence, there is an improvement in the overall DC performance of C-doped HBTs in comparison to Be-doped ones. This is due to the better quality of the emitter-base interface since the diffusion coefficient of C is much less than that of Be. The outdiffusion of Be degrades the quality of emitter-base interface and results in dominance of recombination current for base current which is clear from the higher value of ideality factor of the base current. In the present work both types of HBTs have an abrupt emitter-base heterojunction. In our earlier investigations it has been shown that in case of Be-doped base HBTs, the graded emitter-base junction HBTs display much better performance than abrupt junction HBTs. So we conclude that for C-doped graded emitter-base junctions still better HBT performance can be estimated.

To fabricate smaller area transistors having typical dimensions of $2\times10\ \mu m^2$ to $5\times20\ \mu m^2$, it is required to have perpendicular sidewalls when the etching of the different epitaxial layers of an HBT is carried out. The wet chemical etching solutions normally used for fabrication of larger area transistors were not useful for smaller area transistors since substantial lateral etching is observed in the InGaAs layers. Therefore, to obtain perpendicular sidewalls, the etching of InGaAs layers was done using reactive ion etching method using Cl_2/Ar plasma. The etching rate for InGaAs was about 600 nm/min. Using this etching method, desired results were obtained as can be seen from Fig. 2 where an SEM photograph of a test structure is depicted. We also attempted to fabricate a self-aligned base contact after etching through emitter layers (220 nm in thickness) using emitter metal contact (Ti/Pt/Au 20/20/200nm) as mask. The etching of the emitter layers was done using wet chemical solutions. The SEM image of a fabricated self-aligned base contact for smaller area HBTs is shown in Fig. 3.

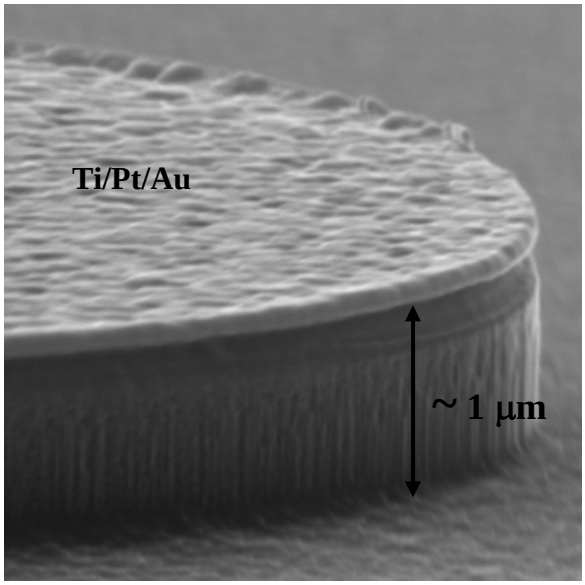

Fig. 2: *Reactive ion etching of InGaAs using Cl_2/Ar plasma.*

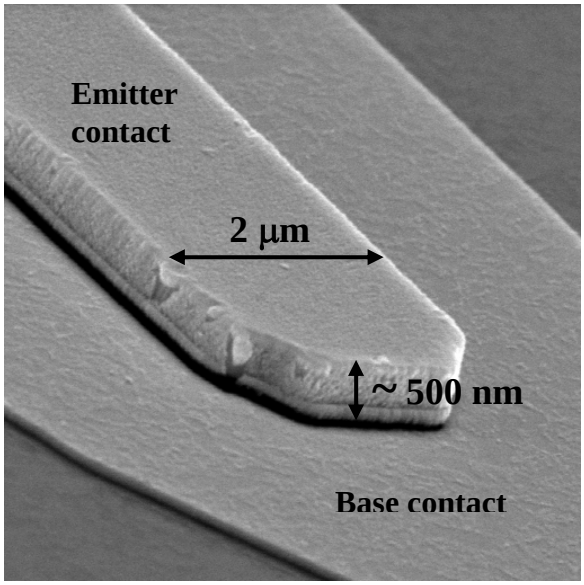

Fig. 3: *Self-aligned deposition of base contact. The ohmic contact used is Ti/Pt/Au.*

Capacitively detected magnetic resonance: an advanced tool for MOS characterization

S. Baldovino [(1)], M. Fanciulli [(1)] T. Graf , M. S. Brandt, and M. Stutzmann

The study of the electrically active defects at the Si/oxide interface is a crucial issue for the evaluation of the reliability and performances of a device. In this work we present the first measurements of capacitavely detected magnetic resonance (CDMR) on a standard Si/SiO_2 MOS structure, leading to the identification of the electrically active defects as a function of the bias voltage i.e. of the energy depth in the Si bandgap.

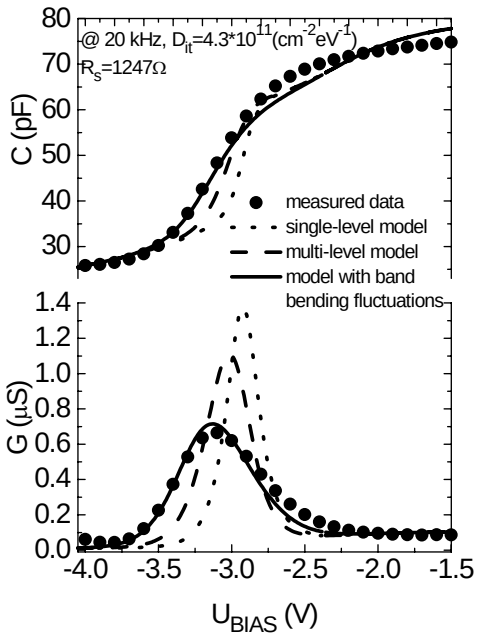

***Figure 1**: Experimental C(V) and G(V) characteristics of the Si/SiO₂ interface studied (dots) and simulations (lines).*

CDMR measurements were performed on an n-type (100)Si/SiO_2 MOS structure. Capacitance versus voltage, C(V), and conductance versus voltage, G(V), curves were taken in dark at room temperature, after inserting the sample in the standard TE_{102} cavity of an X-band electron-spin-resonance spectrometer.

In Figure 1 we report the C(V) and G(V) obtained at 20 kHz. From the analysis of the maximum parallel conductance peak versus frequency at different bias voltages a defect density D_{it} of the order of $1\text{-}3*10^{11}/eVcm^2$ and defects with time constants (time needed by the trap to reach equilibrium exchanging electrons with the silicon) of the order of 10^{-3}-10^{-5} s are observed. To explain the observed C(V) and G(V) characteristics, 3 different models have been studied, all starting from the Shockley-Read-Hall (RDH) theory that describes the generation-recombination of electrons and holes at a single level trap. The first model assumes that all traps have the same energy. The second takes into account that in reality at the Si/SiO_2 interface many trap levels are observed, with energies close enough to form a continuum of levels in the Si bandgap. The third model considers the presence of fixed oxide charges randomly distributed under the gate, leading to band bending fluctuations, with a corresponding time constant dispersion. The results of the simulations obtained with the different models are shown in Figure 1. In CDMR, only paramagnetic defects at the Fermi level can be observed. The capture process depends on the relative spin orientation of the electron in the conduction band and in the trap. Since the Pauli's exclusion principle requires the final state after the capture to be a singlet (S=0), the capture occurs only if the electron-trap pair has initial state S=0. Consequently, for magnetic resonance, a time constant reduction is observed, because the number of singlets increases. In this way, electron spin resonance affects the electrical behaviour of the traps, changing the capacitance and conductance.

In Figure 2 the spectrum obtained monitoring the resonant changes in capacitance and conductance at a fixed bias voltage, at 9.35 GHz, for magnetic field $H \parallel [011]$ is reported;

phone:+49-89-289-12768, fax:+49-89-289-12737, email: silvia.baldovino@wsi.tum.de

Both, capacitance and conductance show the same line shape, with a g-factor of 2.0040±0.0005. From the position of the resonance we can deduce that the traps responding in this range of bias voltage, are silicon dangling bonds at the Si/SiO_2 interface.

The amplitude of the spectra exhibit a characteristic bias voltage dependence, reported in Figure 3, that can be explained by calculating the changes in capacitance and conductance induced by small resonant changes $\Delta\tau$ in the time constant. We assume $\Delta\tau$ to depend on the bias voltage.The result of such simulations is also presented in Figure 3. We also have simulated a change induced by a change of the serial resistance and of a possible shunt due to leaky oxide, but none of these could explain either the magnitude or the voltage dependence observed.

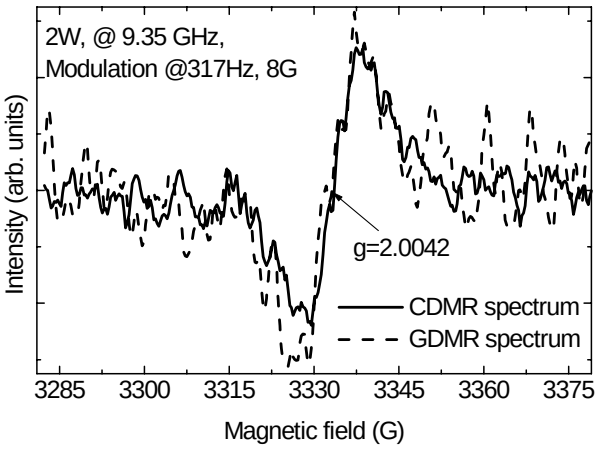

Figure 2: *Spectra obtained monitoring the resonant change in capacitance (CDMR) and conductance (GDMR) at a fixed bias voltage of –3.15V at a fixed test frequency of 20 kHz.*

The analysis of the amplitude of the CDMR spectra allows the quantitative determination of the number of resonant defects. Since electron spin resonance reduces the trapping time constant, the number of trapping events increases, leading to an additional charge ΔQ at the interface traps. The change in charge produces a change in the voltage across the depletion layer, $\Delta U=\Delta Q/C$, and consequently a change in the capacitance that in first approximation will be $\Delta C = \frac{dC}{dU}\Delta U = \frac{1}{C}\frac{dC}{dU}\Delta Q$. Deducing the prefactor $\frac{1}{C}\frac{dC}{dU}$ from the C(V) characteristics, it is possible to determine the charge resonantly stored at the defects site and from this the number of resonant defects. The minimum number of resonant defects that could be detected was found to be 150±100, which proves the high sensitivity of the technique. To obtain the relationship between the density of paramagnetic defects as a function of the energy position in the Si bandgap it is necessary to repeat the same measurement at different test frequencies, since for a given frequency ω only defects with an $\omega\tau \cong 2.47$ can completely follow the applied ac voltage.

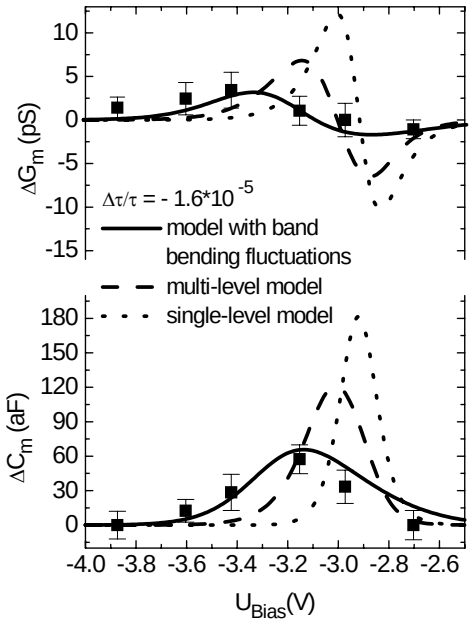

Figure 3: *Voltage dependence of the amplitude of CDMR and GDMR. The dots represent the experimental data taken at 20 kHz, while the lines are the simulations with the different models.*

[1]Laboratorio MDM-INFM, I-20041 Agrate Brianza

Impedance optimisation of millimetre-wave ASV frequency triplers

Markus Krach[1], Jürgen Freyer, and Manfred Claassen

In order to realise local oscillators which deliver sufficient output power at millimetre- and submillimetre-wave frequencies, non-linear varactor diodes are used for multiplying the signal of a fundamental oscillator. The rf-circuit of frequency triplers can be simplified if varactors with symmetric characteristics are applied, since neither idler nor bias circuitry is necessary. The ASV combines the advantages of symmetric devices with the low leakage currents of Schottky diodes enabling nearly pure reactive multiplication also for high amplitudes of the input signal.

The ASV consists of two Schottky diodes with stepwise constant doping profile which are anti-serially connected by an air-bridge. This type of varactor shows a symmetric elastance-voltage characteristic and relatively low conduction currents. A large elastance change and a low series resistance are the main optimisation criteria for a high performance varactor based frequency tripler. The design rules for the individual Schottky diodes are determined by the help of a theoretical model which includes relevant physical effects such as self-biasing and maximum drift velocity of the charge carriers in the modulation zone of the varactor. Earlier results have shown an optimum layer sequence of an ASV for an output frequency of about 230 GHz as follows: the layer structure consists of a GaAs n^+-contact layer doped at $4{\cdot}10^{18}$ cm^{-3}, a GaAs modulation zone which comprises a 300 nm layer doped at $1{\cdot}10^{17}$ cm^{-3}, the width of which is limited by the maximum drift velocity of the electrons, and a 16 nm layer doped at $4{\cdot}10^{18}$ cm^{-3}, and finally a 15 nm undoped $Al_{0.55}Ga_{0.45}As$ layer on top of which a Ti Schottky contact is deposited. The AlGaAs layer enables a further reduction of the convection current across the Schottky barrier. The series resistance of the Schottky diodes is experimentally minimised by the help of large area n^+-contact pads.

Thermal limitations of the entire varactor are determined by a thermal equivalent circuit of the ASV structure on the quartz substrate. Optimisation of the varactor impedance is carried out by a further simulation programme using Fourier analysis. Since the varactor impedance increases with decreasing device diameter, small area devices are preferred for reducing circuit induced losses. However, for small area devices the output power is also small. In order to optimise the de-

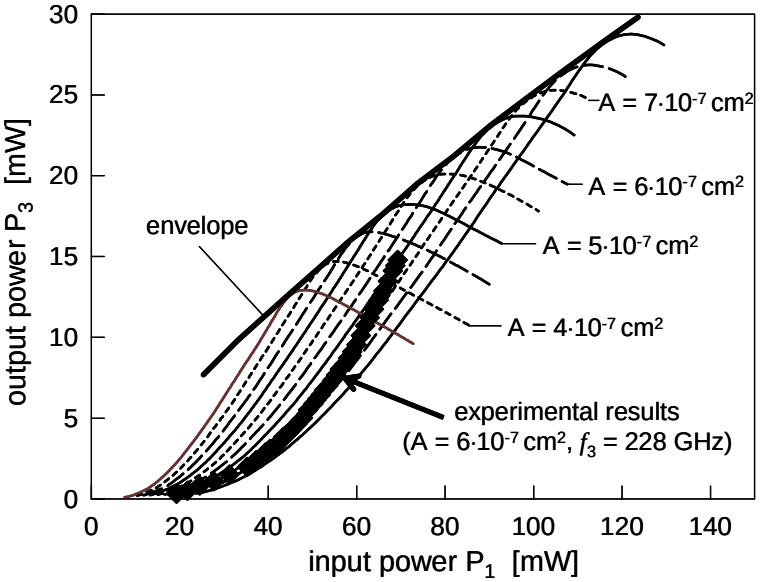

Fig. 1: *Calculated output power P_3 versus input power P_1 of ASVs with different device areas (f_1 = 76 GHz, f_3 = 228 GHz, $R_{CIRCUIT\ LOSS}$ = 0.8 Ω)*

[1]phone : +49-89-289-12787, fax : +49-89-3206620, email : markus.krach@wsi.tum.de

vice area for a given circuit loss resistance, rf output power in dependence of the input power has been computed for different device areas. Thereby Fourier analysis is applied to measured capacitance-voltage and current-voltage characteristics of the individual Schottky diodes. As can be seen from Fig. 1 for a given device area there exists a maximum in the output power in dependence of the input power. The envelope in Fig. 1 represents the maximum output power versus input power with device area as parameter. This correlation is shown once more in Fig. 2 where the resulting optimum input power P_1* (for maximum output power) is plotted versus device area. It can be seen that the optimum input power is well below the thermal limit of the ASV. Additionally the simulated conversion efficiency is plotted versus device area. For a maximum available input power of 100 mW, for example, the optimum device area of an ASV is about $7 \cdot 10^{-7}$ cm^2 from which a conversion efficiency of about 23 % would result (see Fig. 2).

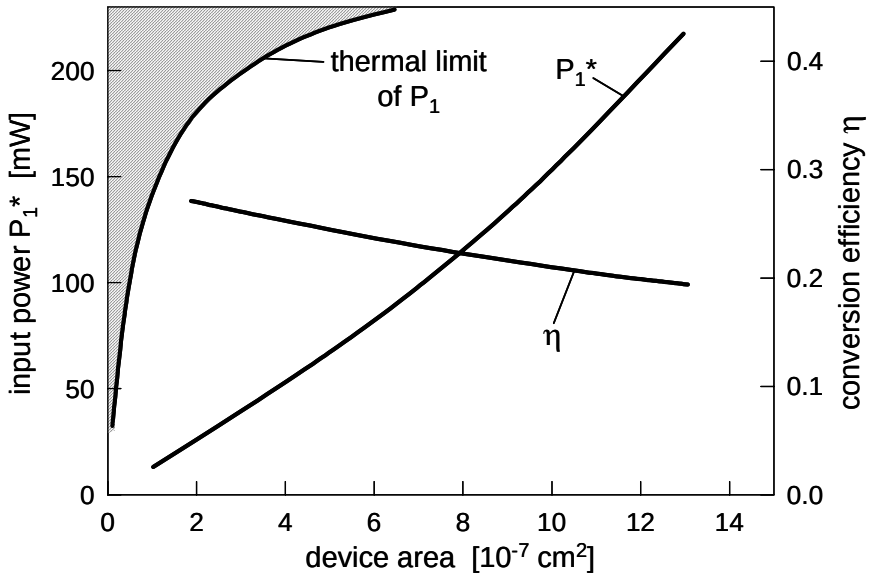

Fig. 2: *Calculated optimum input power P_1* for maximum output power and conversion efficiency of an ASV as a function of the device area (The hatched area shows the thermal limitation of the input power)*

The entire multiplier circuit consisting of the ASV, a low pass filter and the antennas for input and output coupling between microstrip and waveguide is fabricated quasi-monolithically integrated on quartz substrate. This technique enables a combination of the low loss properties of quartz substrates with the high precision and high reproducibility of the monolithic integration. An accurate control of the whole rf-circuit is achieved by the help of commercial modelling software such as HFSS and ADS. A split waveguide mount is used to test the multiplier performance of the ASV tripler circuit. Fine-tuning is realised with backshorts at both, input and output waveguide. The experimental results, carried out with a device area of $6 \cdot 10^{-7}$ cm^2 and a maximum available input power of 70 mW led to 15 mW maximum power output (see Fig. 1) which is in good agreement with the theoretical value of about 17 mW as maximum output power for the given device area. The achieved flange to flange conversion efficiency of 22 % at 228 GHz represents an essential improvement in efficiency as compared to HBV based frequency triplers.

---

supported by DFG (SFB 348)

Prediction of realistic quantum logic gate using the contact block reduction algorithm

Matthias Sabathil[1], Denis Mamluy, and Peter Vogl

In a semiconductor heterostructure a single qubit may be realized by electrons propagating ballistically within two adjacent quantum wires. The $|0\rangle$ and $|1\rangle$ basis states are then represented by an electron fully localized in either one of the wires. Based on this concept single- and two- qubit gates have been proposed [1]. In this work we predict a realistic single qubit switch that operates via gate controlled interference between a pair of quantum wires. The interference is induced by narrow windows in the barrier region between the wires that act as beam splitters, allowing the 0 and 1 states to interfere. Additional gates are needed to control the phase shifts within one of the wires. We propose a concrete solid-state realization of a Mach-Zehnder interferometer (Fig. 1, inset) based on an AlGaAs/GaAs three-dimensional nanostructure [2]. The interference-induced switching can be observed via the ballistic current.

The active region of our quantum logic device is an AlGaAs/GaAs high mobility 2DEG with several top gates that produce the required lateral confinement. The bottom of Fig. 1 shows a cross section through the structure that is grown on an $Al_{0.3}Ga_{0.7}As$ substrate with a 10 nm wide n+ doping ($5\times10^{18}/cm^3$) layer followed by a 30 nm intrinsic buffer layer. The 2DEG is confined within a 10 nm GaAs quantum well followed by another 20 nm $Al_{0.3}Ga_{0.7}As$ buffer. A second n+ doping region of 10 nm width ($1\times10^{18}/cm^3$) accounts for the filling of the quantum well. Finally, there is a Schottky contact at the top of the structure. None of the lateral scales lie below 50 nm. This electrostatic confinement via the gates offers sufficient potential variation in order to steer the device.

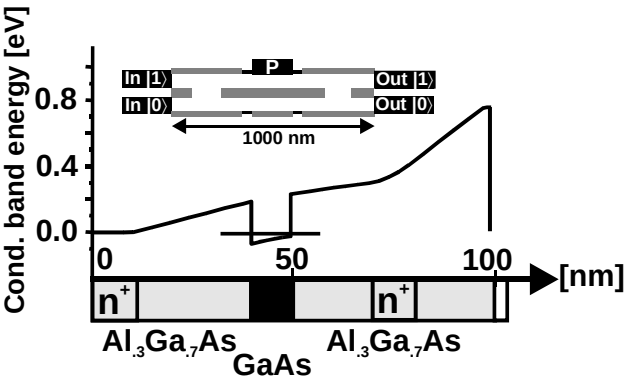

***Fig. 1**: Top inset: Schematic top view of proposed solid-state Mach-Zehnder interferometer. The gray areas are barriers introduced via top gates. The P-gate acts as a phase shifter for the upper channel. The two windows in the middle barrier act as beam splitters for the electrons in the channel. Bottom: Vertical cross section through the structure. Middle: Conduction band profile in eV in growth direction. Details are described in the text.*

The quantum transport through the device has been calculated in two steps. Firstly, the equilibrium potential profile of the three-dimensional structure including the gate electrodes has been calculated self-consistently, using our device simulator nextnano3 [3]. This amounts to solving the 3D single-band Schrödinger equation together with the Poisson equation self-consistently. Secondly, the ballistic transmission through the device is computed with the CBR method [4] which yields the current via the Landauer formula. The results in Fig. 2 show that the current can indeed be switched from a non-inverting to an inverting state. The phase shifting gate P controls the flow from the left leads to the right leads. For a gate voltage of

[1]phone:+49-89-289-12762, fax:+49-89-289-12737, email: sabathil@wsi.tum.de

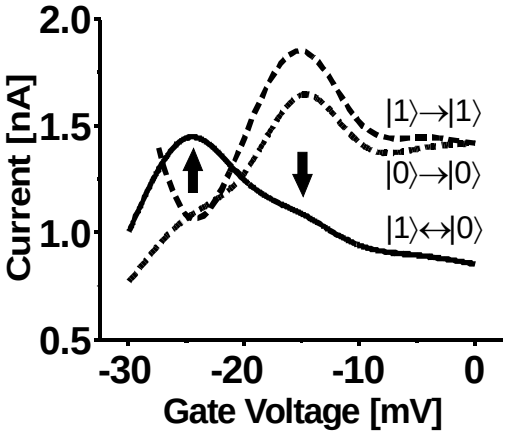

Fig. 2: *Source-drain current through the interferometer as a function of phase-shifting gate voltage. Full line marks the current between the |0⟩ and |1⟩ leads, dashed lines label the current between the |0⟩ to |0⟩ or |1⟩ to |1⟩ leads, respectively. The arrows indicate the voltages of maximal switching.*

-15 mV, Fig. 2 shows a large current to flow between the leads In|1⟩ to Out|1⟩ and In|0⟩ to Out|0⟩, respectively, which corresponds to a current from $0 \rightarrow 0$ and $1 \rightarrow 1$. For a gate voltage of -25 mV, by contrast, the current flows dominantly from $0 \rightarrow 1$ and $1 \rightarrow 0$ which corresponds to an inversion. The efficiency is about 30% for the chosen temperature of 200 mK and an applied source-drain bias of 0.05 mV.

The presented calculations showed that the contact block reduction method (CBR) is a highly efficient scheme to compute the ballistic transmission function through a 3D device using a single band Hamiltonian. We generalized this method to multi-band k.p Hamiltonian systems in order to be able to deal with p-type devices, narrow-band materials, and molecular electronic systems. To demonstrate the efficiency of the CBR method in the multi-band case, we have calculated the transmission through a model 2D 20 by 10 nm SiGe double gate p-MOSFET (see inset of Fig. 3). We used a 4 band k.p Hamiltonian that includes light and heavy hole bands. All biases are set to zero and the channel potential is also set to zero, except for the barrier regions (shown in black in the inset) that are taken to be 0.4 eV. The k.p parameters are used for p-Ge throughout the whole device. Fig. 3 shows the transmission function between source and drain (S-D) as well as between source and Gate (S-G). The results show that the method is converged already when only 10% of all eigenvectors are taken into account. Thus, the efficiency of the CBR method is not limited to one-band models and can be successfully applied to multi-band situations.

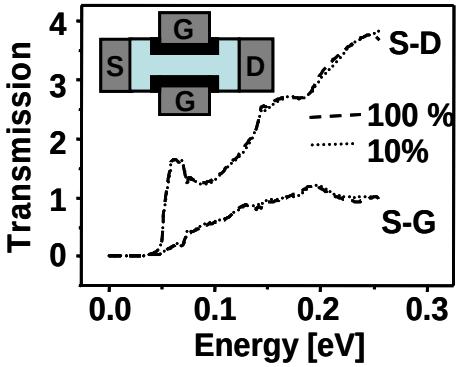

Fig. 3: *Transmission as a function of energy from source to drain (S-D) and source to gate (S-G) of a model double gate SiGe p-MOSFET. The dashed lines show the results for all eigenvectors and the dotted lines show the transmission for a reduced set of only 10% of all eigenvectors.*

[1] A. Bertoni et al., Phys. Rev. Lett. **84**, 5912 (2000)
[2] M.Sabathil et al., Semicond. Sci. Technol. **19**, S137 (2004)
[3] S. Hackenbuchner et al. Physica B **314**, 145 (2002)
[4] D. Mamaluy, M. Sabathil, and P. Vogl, J. Appl. Phys. **93**, 4628 (2003)

supported by the Deutsche Forschungsgemeinschaft (DFG) and the Office of Naval Research (ONR) Contract No. N00014-01-1-0242

3. Research Funding and Collaborations

Many of our research projects have benefited from very fruitful collaborations with external groups either via joint projects, individual collaborations, exchange programs or through direct interaction with visitors. The major external collaborations are based on joint projects which are financially supported by different organizations.

Funded Projects

1. Bundesministerium für Bildung und Forschung (BMBF)

- Kompetenzzentrum Nanoclub Lateral: „Selbstorganisiertes Wachstum auf Si“ (SOWASI, partner: DaimlerChrysler Ulm)
- Kompetenzzentrum Nanop: „Anwendung von Nanostrukturen in der Optoelektronik“
- Kristalline Silizium-Legierungen für Dünnschicht-Solarzellen
- Förderschwerpunkt Elektronenkorrelation und Dissipationsprozesse in Halbleiter-quantenstrukturen: „Vertikale Ultrakurzkanal- und Tunneltransistoren“, „Deterministische Ladungsquelle“
- Förderschwerpunkt MultiTeraNet; “Mikromechanisch abstimmbare VCSEL für den Wellenlängenbereich 1,5 µm
- Förderschwerpunkt neue Materialien; “Materialien für Infrarotkonverter“
- „Netz Erneuerbare Energieforschung: Photon-Management und Bandstruktur-Design für effizientere Solarzellen“

2. Deutsche Forschungsgemeinschaft (DFG)

- Sonderforschungsbereich „Nanometer-Halbleiterbauelemente“ (SFB 348)
- Sonderforschungsbereich „Bioorganische Funktionssysteme auf Festkörpern“ (SFB 563)
- Sonderforschungsbereich „Festkörperbasierte Quanteninformationsverarbeitung“ (SFB 631)
- Schwerpunktprogramm „Quanten-Hall-Systeme“
- Schwerpunktprogramm „Optische Übermittlungsverfahren in der Informationstechnik“
- Forschungskooperation „FORMEDIAN“
- Am 101/6-1: „Transversal integrierte abstimmbare Laserdioden“
- Br 1960/1-3: „Lichtemission von Intrabandübergängen in Si/SiGe-Heterostrukturen“
- Ei 518/1-1: „Heteroepitaxie von Gruppe III-Nitriden auf Diamantsubstraten für optoelektronische und elektronische Anwendungen“
- Ne 524/1-2: „Mikromechanische und elektronische Diamantanwendungen: CVD-Diamant“
- Stu 139/6-3: „Amorphe Suboxide des Siliziums“
- Vo 483/4-3: „Herstellung und Untersuchung epitaktischer Metall-Isolator Resonant-Tunneling-Bauelemente für die Silizium-Nanoelektronik“

3. Bayerische Forschungsstiftung

- Langfristprogramm Neue Werkstoffe
- ForNano: Miniaturisierte Analyseverfahren durch Nanotechnologie in Biochemie, Chemie und Physik

4. European Union

- COLLECT (Collective electronic states in nanostructures: INFM and other partners, Italy)
- DODD's (Doped Diamond Devices and Sensors, partners: Kings College London, Instituut voor Maerial Onderszoek Limburg, Institute of Physics - Acad. of Sciences of the Czech Republic Praha, LEPES, Grenoble, University College London, CEA/LETI Gif sur Yvette, Technion Haifa)
- ESRQC (Electron Spin Resonance Quantum Computing, partner: INFM-MDM, Italy)
- NEWTON (New Widely Tunable Lasers for Optical Networks, partners: IMEC, INTUNE, ADC)

5. DAAD

- Acciones Integradas Hispano-Alemanas – PPP mit Spanien
- PROCOPE – PPP mit Frankreich

6. Office of Naval Research

- N00014-01-1-0242: “Modeling and simulation of semiconductor nanostructures”

7. Industry

- Infineon, München, Germany:
  „Zweidimensionale quantenmechanische Simulation“, „Quantenmechanische MOSFET-Simulation“
- EADS Deutschland GmbH, Ottobrunn, Germany:
  „Sensorik auf der Basis von Halbleitern mit großer Bandlücke“
- Osram Optosemiconductors, Regensburg, Germany:
  „Prozessierung von GaN Leuchtdioden“
- Fujitsu Laboratories of Europe LTD., Hayes Park, UK:
  “Bio-Nanotechnology”
- Rhode & Schwarz, München, Germany:
  „Zero-Bias Schottky-Diodes“

Other collaborations involve:

RWTH Aachen, Arizona State University, Universität Augsburg, MBI Berlin, TU Berlin, Universität Bremen, CALTECH, Cambridge University, Wacker Siltronic Burghausen, University Chicago, Cornell University, TU Darmstadt, TU Delft, Intune Dublin, Universität Duisburg, Universität Erlangen-Nürnberg, FHG IPM Freiburg, Vertilas Garching, WMI Garching, Gayton Photonics (UK), IMEC Gent, Universität Gießen, Universität Göttingen, Universität Graz, TU Hamburg-Harburg, Universität Hamburg, Universität Hannover, TU Ilmenau, FZ Jülich, Universität Kaiserslautern, Universität GH Kassel, Universität Köln, Linköping University, ETH Lausanne, Universität Leoben, Universität Linz, University College London, Université Montpellier 2, LMU München, Infineon München, Rhode & Schwarz München, Siemens München, Bell Labs. Murray Hill, University of Nagoya, Laser Components Olching, University Osaka, EADS Deutschland Ottobrunn, Universität Paderborn, SNS, Pisa, Czech Academy of Sciences Prag, Universität Regensburg, Università Rom II Tor Vergata, UCSB Santa Barbara, CL SENES Sofia, ADC Stockholm, MPI FKF Stuttgart, Universität Stuttgart, University of Tokyo, National Institute of Materials Science Tsukuba, NEC Tsukaba, DaimlerChrysler Ulm, Universität Ulm, Naval Research Laboratory Washington, TU Wien, Kistler Instrumente Winterthur, Nanoplus Würzburg, Universität Würzburg, ETH Zürich, Nortel Zürich.

6. Publications

Electronics and sensors based on pyroelectric AlGaN/GaN heterostructures, Part A: Polarization and pyroelectronics
O. Ambacher, M. Eickhoff, A. Link, M. Hermann, M. Stutzmann, F. Bernardini, V. Fiorentini, Y. Smorchkova, J. Speck, U. Mishra, W. Schaff, V. Tilak, and L. F. Eastmann
phys. stat. sol. (c) **0**, 1878-1907 (2003) **(review article)**

Investigation of point defects at the high-k oxides/Si (100) interface by electrically detected magnetic resonance
S. Baldovino, S. Nokhrin, G. Scarel, M. Fanciulli, T. Graf, and M. S. Brandt
J. of Non-Crystalline Solids **322**, 168 (2003)

Group III-nitrides and their heterostructures: growth, characterization, and applications
Collection of review articles from the Priority Programme SPP 1032 (German Research Foundation), ed. by Friedhelm Bechstedt, Bruno K. Meyer, and Martin Stutzmann
phys. stat. sol. (c) **0** (2003)

Rabi-flopping of the ground state excition in a single self-assembled quantum dot
E. Beham, A. Zrenner, F. Findeis, M. Bichler, and G. Abstreiter
phys. stat. sol. (b) **238**, 366-369 (2003)

Coherent and incoherent properties of single quantum dot photodiodes
E. Beham, A. Zrenner, S. Stufler, F. Findeis, M. Bichler, and G. Abstreiter
Physica E **16**, 59-67 (2003)

Circular photogalvanic effect at inter-band excitation in semiconductor quantum wells
V. V. Bel`kov, S. D. Ganichev, P. Schneider, C. Back, M. Oestreich, J. Rudolph, D. Hagele, L. E. Golub, W. Wegscheider, and W. Prettl
sol. stat. com. **128**, 283-286 (2003)

Spin-photocurrent in p-SiGe quantum wells under terahertz laser irradiation
V. V. Bel`kov, S. D. Ganichev, P. Schneider, D. Schowalter, U. Roessler, W. Prettl, E. L. Ivchenko, R. Neumann, K. Brunner, and G. Abstreiter
J. of Superconductivity **16**, 415-418 (2003)

Tunable single and dual mode operation of an external cavity quantum-dot injection laser
A. Biebersdorf, C. Lingk, M. De Giorgi, J. Feldmann, J. Sacher, M. Arzberger, C. Ulbrich, G. Böhm, M.-C. Amann, and G. Abstreiter
J. Phys. D: Appl. Phys. **36**, 1-3 (2003)

nextnano³ - Software für neuartige Nano Devices
S. Birner
TUM Mitteilungen 2 - 03/04, TU Munich, 36 (2003)

Phase coherent transport in two coupled quantum dots
R. H. Blick, A. K. Huttel, A. W. Holleitner, E. M. Hohberger, H. Qin, I. Kirschbaum, J. Weber, W. Wegscheider, M. Bichler, K. Eberl, and J. P. Kotthaus
Physica E **16**, 76-82 (2003)

InP-based VCSEL technology covering the wavelength range from 1.3 to 2.0 µm
G. Böhm, M. Ortsiefer, R. Shau, J. Rosskopf, C. Lauer, M. Maute, F. Köhler, F. Mederer, R. Meyer, and M.-C. Amann
J. Cryst. Growth **251**, 748-753 (2003)

Nonradiative relaxation times in diagonal transition Si/SiGe quantum cascade structures
I. Bormann, K. Brunner, S. Hackenbuchner, G. Abstreiter, S. Schmult, and W. Wegscheider
Appl. Phys. Lett. **83**, 5371-5373 (2003)

Intraband photoresponse of SiGe quantum dot/quantum well multilayers
D. Bougeard, K. Brunner, and G. Abstreiter
Physica E **16**, 609-613 (2003)

DX behaviour of Si donors in AlGaN alloys
M. S. Brandt, R. Zeisel, S. T. B. Gönnenwein, M. W. Bayerl, and M. Stutzmann
phys. stat. sol. (b) **235**, 13-19 (2003)

Silicon- and germanium-based sheet polymers and Zintl phases
M. S. Brandt, G. Vogg, and M. Stutzmann
in: Silicon Chemistry - From the Atom to Extended Systems, ed. by P. Jutzi and U. Schubert Wiley-VCH, Weinheim (2003), p. 194

Metamorphosis of the quantum Hall ferromagnet at $\nu = 2/5$
M. Chen, W. W. Kang, and W. Wegscheider
Phys. Rev. Lett. **91**, 116804 (2003)

Resonant raman scattering of double wall carbon nanotubes prepared by chemical vapor deposition method
L. J. Ci, Z. P. Zhou, X. Q. Yan, D. F. Liu, H. J. Yuan, L. Song, Y. Gao, X. J. Wang, L. F. Liu, W. Y. Zhou, G. Wang, S. S. Xie, and P. H. Tan
J. of Appl. Phys. **94**, 5715-5719 (2003)

Electronics and sensors based on pyroelectric AlGaN/GaN heterostructures, Part. B: Sensor applications
M. Eickhoff, J. Schalwig, G. Steinhoff, O. Weidemann, L. Görgens, R. Neuberger, M. Hermann, B. Baur, G. Müller, O. Ambacher, and M. Stutzmann
phys. stat. sol. (c) **0**, 1908-1918 (2003)

Laser-crystallized microcrystalline SiGe alloys for thin film solar cells
C. Eisele, M. Berger, M. Nerding, H. P. Strunk, C. E. Nebel, and M. Stutzmann
Thin Solid Films **427**, 176-180 (2003)

Ultrafast coherent and incoherent dynamics of intersubband excitations in semiconductor quantum wells
T. Elsässer, R. A. Kaindl, F. Eickemeyer, K. Reimann, M. Woerner, R. Hey, Ch. Miesner, K. Brunner, and G. Abstreiter
in: Proceedings of SPIE **4992** (2003), p. 154-164

Anisotropic high-mobility quantum Hall transport: two-dimensional electrons subject to few millikelvins and misoriented substrates
F. Ertl, O. Jaeger, R. A. Deutschmann, M. Bichler, G. Abstreiter, E. Schuberth, C. Probst, and W. Wegscheider
in: Physics of Semiconductors 2002, Institute of Physics Conference Series **171**, ed. by A. R. Long and J. H. Davies, Institute of Physics Publishing Bristol (2003), p. **E2.2**

Systematic reduction of the permanent exciton dipole for charged excitons in individual self-assembled InGaAs quantum dots
J. J. Finley, M. Sabathil, R. Oulton, A. I. Tartakovskii, D. J. Mowbray, M. S. Skolnick, S. Liew, M. Migliorato, M. Hopkinson, and P. Vogl
in: Physica E, Proc. 11th International Conference on Modulated Semiconductor Structures, ed. by Y. Arakawa, H. Ohno, K. Hirakawa, and M. Tanaka, **21** (2003), p. 199-203

Singlet-triplet transition tuned by asymmetric gate voltages in a quantum ring
A. Fuhrer, T. Ihn, K. Ensslin, W. Wegscheider, and M. Bichler
Phys. Rev. Lett. **91**, 206802 (2003)

Spin-galvanic effect due to optical spin orientation in n-type GaAs quantum well structures
S. D. Ganichev, P. Schneider, V. V. Bel`kov, E. L. Ivchenko, S. A. Tarasenko, W. Wegscheider, D. Weiss, D. Schuh, B. N. Murdin, P. J. Phillips, C. R. Pidgeon, D. G. Clarke, M. Merrick, P. Murzyn, E. V. Beregulin, and W. Prettl
Phys. Rev. B **68**, 081302 (2003)

Resonant inversion of the circular photogalvanic effect in n-doped quantum wells
S. D. Ganichev, V. V. Bel`kov, P. Schneider, E. L. Ivchenko, S. A. Tarasenko, W. Wegscheider, D. Weiss, D. Schuh, E. V. Beregulin, and W. Prettl
Phys. Rev. B **68**, 035319 (2003)

Fabrication of in-plane gate transistors on hydrogenated diamond surfaces
J. A. Garrido, C. E. Nebel, R. Todt, G. Rösel, M.-C. Amann, M. Stutzmann, E. Snidero, and P. Bergonzo
Appl. Phys. Lett. **82**, 988-990 (2003)

Novel in-plane gate devices on hydrogenated diamond surfaces
J. A. Garrido, C. E. Nebel, R. Todt, M.-C. Amann, O. A. Williams, R. Jackman, M. Nesládek, and M. Stutzmann
phys. stat. sol. (a) **199**, 56-63 (2003)

Spin wave resonance in $Ga_{1-x}Mn_xAs$
S. T. B. Gönnenwein, T. Graf, T. Wassner, M. S. Brandt, M. Stutzmann, J. B. Philipp, R. Gross, M. Krieger, K. Zürn, P. Ziemann, A. Koeder, S. Frank, W. Schoch, and A. Waag
Appl. Phys. Lett. **82**, 730-732 (2003)

Ferromagnetic resonance in $Ga_{1-x}Mn_xAs$
S. T. B. Goennenwein, T. Graf, T. Wassner, M. S. Brandt, M. Stutzmann, A. Koeder, S. Frank, W. Schoch, and A. Waag
J. of Superconductivity **16**, 75 (2003)

Spin resonance investigations of Mn^{2+} in wurtzite GaN and AlN films
T. Graf, M. Gjukic, M. Hermann, M. S. Brandt, and M. Stutzmann
Phys. Rev. B **67**, 165215 (2003)

Growth and characterization of GaN:Mn epitaxial films
T. Graf, M. Gjukic, M. Hermann, M. S. Brandt, M. Stutzmann, L. Görgens, J. B. Philipp, and O. Ambacher
J. Appl. Phys. **93**, 9697-9702 (2003)

Charge transfer at the Mn acceptor level in GaN
T. Graf, M. Gjukic, L. Görgens, O. Ambacher, M. S. Brandt, and M. Stutzmann
J. of Superconductivity **16**, 83 (2003)

Hyperfine interactions at dangling bonds in amorphous germanium
T. Graf, T. Ishikawa, K. M. Itoh, E. E. Haller, M. Stutzmann, and M. S. Brandt
Phys. Rev. B **68**, 205208 (2003)

Prospects of carrier-mediated ferromagnetism in GaN
T. Graf, S. T. B. Goennenwein, and M. S. Brandt
phys. stat. sol. (b) **239**, 277 (2003)

Electrically detected magnetic resonance and its application to diamond
T. Graf, M. S. Brandt, C. R. Miskys, J. A. Garrido, M. Hermann, O. Ambacher, M. Eickhoff, C. E. Nebel, S. Koizumi, and M. Stutzmann,
ext. Abstract for the 54th DeBeers Diamond Conference, Cambridge, UK (2003)

Continuous wave GaInAsSb/AlGaAsSb type-I double quantum well lasers for 2.96 µm wavelength
M. Grau, C. Lin, O. Dier, and M.-C. Amann
Electron. Lett. **39**, 1816-1817 (2003)

Room temperature cw GaInAsSb-AlGaAsSb laser diodes for 3µm wavelength range
M. Grau, C. Lin, O. Dier, and M.-C. Amann
in: 87th OSA Annual Meeting 2003, Tucson/USA (October 2003)

Momentum resolved tunnel spectroscopy of integer quantum Hall edges: A tool for measuring edge electrostatics
M. Huber, M. Grayson, M. Rother, W. Biberacher, W. Wegscheider, M. Bichler, and G. Abstreiter
in: ICPS-26 Proceedings, Institute of Physics Conference Series Number **171**, ed. by A. R. Long and J. H. Davies (2003), p. M2.3

Ultrafast formation of many-particle interactions in a photoexcited electron-hole plasma
R. Huber, F. Tauser, A. Brodschelm, M. Bichler, G. Abstreiter, and A. Leitenstorfer
Proc. of SPIE **4992** (2003) p. 130-137

Marvellous things in marvellous rings: energy spectrum, spins and persistent currents
T. Ihn, A. Fuhrer, T. Heinzel, K. Ensslin, W. Wegscheider, and M. Bichler
Physica E **16**, 83-89 (2003)

Photoluminescence of Er^{3+} implanted amorphous hydrogenated silicon suboxides
A. Janotta, M. Schmidt, R. Janssen, M. Stutzmann, and Ch. Buchal
Phys. Rev. B **68**, 165207-17 (2003)

Kondo effect in a few-electron quantum ring
U. F. Keyser, C. Fühner, S. Borck, R. J. Haug, M. Bichler, G. Abstreiter, and W. Wegscheider
Phys. Rev. Lett. **90**, 196601-1 (2003)

Aharonov-Bohm effect of a quantum ring in the Kondo regime
U. F. Keyser, C. Fuhner, R. J. Haug, W. Wegscheider, M. Bichler, and G. Abstreiter
phys. stat. sol. (b) **238**, 331-334 (2003)

Carrier concentration and lattice constant of GaMnAs
A. Koeder, S. Frank, W. Schoch, V. Avrutin, W. Limmer, K. Thonke, S. Brotzmann, H. Bracht, S. T. B. Goennenwein, T. Graf, T. Wassner, M. Brandt, M. Stutzmann, M. Krieger, K. Zürn, P. Ziemann, and A. Waag
ext. abstract for the 12th Euro-MBE Workshop, Bad Hofgastein, Austria (2003)

Local structure of Ge/Si nanostructures: uniqueness of XAFS spectroscopy
A.V. Kolobov, H. Oyanagi, A. Frenkel, I. Robinson, J. Cross, S. Wei, K. Brunner G. Abstreiter, Y. Maeda, A. Shklyaev, M. Ichikawa, S. Yamasaki, and K. Tanaka
Nuclear Instruments & Methods **199**, 174-178 (2003)

High performance millimetre wave tripler by optimisation of varactor and circuit matching
M. Krach, J. Freyer, and M. Claassen
in: Proc. of 3rd ESA Workshop on Millimetre Wave Technology and Applications, Espoo, Finland (2003), p. 143-147

An integrated ASV frequency tripler for millimetre-wave applications
M. Krach, J. Freyer, and M. Claassen
in: Proc. of 33rd EuMC, Munich, Germany (2003), p. 1279-1281

Impedance optimisation of millimetre-wave ASV frequency triplers
M. Krach and J. Freyer
in: Proc. of 27th WOCSDICE 2003, Fürigen, Switzerland (2003), p. 121-122

Ferromagnet-semiconductor hybrid structures: Hall devices and tunnel junctions
S. Kreuzer, A. Rahm, J. Biberger, R. Pulwey, J. Raabe, D. Schuh, W. Wegscheider, and D. Weiss
Physica E **16**, 137-146 (2003)

Wavelength selective charge storage in self-assembled InGaAs/GaAs quantum dots
M. Kroutvar, Y. Ducommun, J. J. Finley, M. Bichler, G. Abstreiter, and A. Zrenner
Appl. Phys. Lett. **83**, 443-445 (2003)

Wavelength selective data storage in InGaAs-GaAs quantum dots
M. Kroutvar, A. Zrenner, Y. Ducommun, J. J. Finley, and G. Abstreiter
phys. stat. sol. (b) **238**, 345-348 (2003)

Demonstration of methane spectroscopy using a vertical-cavity surface-emitting laser at 1.68 µm with up to 5 MHz repition rate
M. Lackner, G. Totschnig, F. Winter, M. Ortsiefer, and M.-C. Amann
Meas. Sci. Technol. **14**, 101-106 (2003)

Electrically pumped room temperature cw-VCSELs with emission wavelength of 2 µm
C. Lauer, M. Ortsiefer, R. Shau, J. Rosskopf, G. Böhm, M. Maute, F. Köhler, and M.-C. Amann
Electron. Lett. **39**, 57-58 (2003)

Size and density estimation of self-assembled InAs quantum dots on GaAs(001) substrate through the analysis of RHEED patterns
J. W. Lee, D. Schuh, M. Bichler, and G. Abstreiter
phys. stat. sol. (c) **0**, 1121-1124 (2003)

Hydrosilylation of crystalline silicon (111) and hydrogenated amorphous silicon surfaces: A comparative x-ray photoelectron spectroscopy study
A. Lehner, G. Steinhoff, M. S. Brandt, M. Eickhoff, and M. Stutzmann
J. Appl. Phys. **94**, 2289-2294 (2003)

Hydrosilylation of silicon surfaces: crystalline versus amorphous
A. Lehner, G. Steinhoff, M. S. Brandt, M. Eickhoff, and M. Stutzmann
in: Mat. Res. Soc. Symp. Proc. **762** (2003), p. A10.5.1-A10.5.5

Photoconductivity and spin-dependent photoconductivity of hydrosilylated (111) silicon surfaces
A. Lehner, F. Kohl, S. A. Franzke, T. Graf, M. S. Brandt, and M. Stutzmann
Appl. Phys. Lett. **82**, 565 (2003)

Transport properties of 2DEGs in AlGaN/GaN heterostructures: spin splitting and occupation of higher subbands
A. Link, T. Graf, O. Ambacher, A. Jimenez, E. Calleja, Y. Smorchkova, J. Speck, U. Mishra, and M. Stutzmann
phys. stat. sol. (b) **234**, 805 (2002)

Transport properties of two-dimensional electron gases induced by spontaneous and piezoelectric polarization in AlGaN/GaN heterostructures
A. Link, T. Graf, R. Dimitrov, O. Ambacher, M. Stutzmann, Y. Smorchkova, U. Mishra, and J. Speck
phys. stat. sol. (b) **228,** 603 (2001)

Resonant spin-orbit interactions and phonon spin relaxation rates in superlattices
J. A. Majewski and P. Vogl
in: Physics of Semiconductors 2002, ed. by. A. R. Long and J. H. Davies, Institute of Physics Publ., Bristol (2003), p. P305

Efficient method for the calculation of ballistic quantum transport
D. Mamaluy, M. Sabathil, and P. Vogl
J. Appl. Phys. **93,** 4628 (2003)

Freestanding GaN-substrates and devices
C. R. Miskys, M. K. Kelly, O. Ambacher, and M. Stutzmann
phys. stat. sol. (c) **0**, 1627-1650 (2003)

AlN/diamond heterojunction diodes
C. R. Miskys, J. A. Garrido, C. E. Nebel, M. Hermann, O. Ambacher, M. Eickhoff, and M. Stutzmann
Appl. Phys. Lett. **82**, 290 (2003)

Carrier dynamics in short wavelength self-assembled InAs/$Al_{0.6}Ga_{0.4}$As quantum dots with indirect barriers
A. F. G. Monte, J. J. Finley, A. D. Ashmore, A. M. Fox, D. J. Mowbray, M. S. Skolnick, and M. Hopkinson
J. Appl. Phys. **93**, 3524 (2003)

Carrier dynamics in red-emitting self-organised InAs-AlGaAs quantum dots with indirect barriers
A. F. G. Monte, J. J. Finley, A. D. Ashmore, A. M. Fox, M. S. Skolnick, D. J. Mowbray, and M. Hopkins
Physica E **17**, 109-110 (2003)

Effects of charge accumulation on the photocurrent and photoluminescence characteristics of self-assembled InAs/GaAs quantum dots
A. F. G. Monte, J. J. Finley, I. Itskevitch, M. S. Skolnick, D. J. Mowbray, and M. Hopkins
Physica E **17**, 37-39 (2003)

Non-linear effects on the power dependent photocurrent of self-assembled InAs/GaAs quantum dots
A. F. G. Monte, J. J. Finley, D. M. Whittaker, I. Itskevitch, D. J. Mowbray, M. S. Skolnick, F. V. Sales, and M. Hopkins
Microelectronics Journal **34**, 667-669 (2003)

Time-resolved measurements and spatial photoluminescence distribution in InAs/AlGaAs quantum dots
A. F. G. Monte, F. V. de Sales, J. J. Finley, A. M. Fox, S. W. da Silva, P. C. Morais, M. S. Skolnick, and M. Hopkins
Microelectronics Journal **34,** 747-749 (2003)

AlN/Diamond np-junctions
C. E. Nebel, C. R. Miskys, J. A. Garrido, M. Hermann, O. Ambacher, M. Eickhoff, and M. Stutzmann
Diam. Relat. Mater. **12**, (1873 (2003)

Silicon-on-insulator based thin-film resistor for chemical and biological sensor applications
M. G. Nikolaides, S. Rauschenbach, S. Luber, K. Buchholz, M. Tornow, G. Abstreiter, and A. R. Bausch
Chem. Phys. Chem. **4**, 1104-1106 (2003)

Single mode 1.55 µm VCSELs with low threshold and high output power
M. Ortsiefer, M. Fürfanger, J. Rosskopf, G. Böhm, F. Köhler, C. Lauer, M. Maute, W. Hofmann, and M.-C. Amann
Electron. Lett. **39**, 1731-1732 (2003)

InP-based VCSELs in the 1.4 to 2 µm wavelength range for optical communication and absorption spectroscopy
M. Ortsiefer, R. Shau, J. Rosskopf, M. Fürfanger, and M.-C. Amann
in: The 16th Annual Meeting of the IEEE Lasers & Electro-Optics Society, (LEOS), Tucson, USA, WD4 (October 2003)

Continuum transitions and phonon coupling in single self-assembled Stranski-Krastanow quantum dots
R. Oulton, J. J. Finley, A. I. Tartakovskii, D. J. Mowbray, M. S. Skolnick, M. Hopkinson, A. Vasanelli, R. Ferreira, and G. Bastard
Phys. Rev. B **68**, 235301 (2003)

Structural and doping effects in the half-metallic double perovskite A_2CrWO_6 (A=Sr, Ba and Ca)
J. B. Philipp, P. Majewski, L. Alff, A. Erb, R. Gross, T. Graf, M. S. Brandt, J. Simon, T. Walther, W. Mader, D. Topwal, and D. D. Sarma
Phys. Rev. B **68**, 144431 (2003)

Metastable phase in the quantum hall ferromagnet
V. Piazza, V. Pellegrini, F. Beltram, and W. Wegscheider
Sol. State Commun. **127**, 163-168 (2003)

Microscopic description of nanostructures grown on (N11) surfaces
M. Povolotskyi, J. Gleize, A. Di Carlo, P. Lugli, S. Birner, and P. Vogl
J. Comput. Electronics **2**, 275 (2003)

Excessive counterion condensation on immobilized ssDNA in solutions of high ionic strength
U. Rant, K. Arinaga, T. Fujiwara, S. Fujita, M. Tornow, N. Yokoyama, and G. Abstreiter
Biophysical Journal **85**, 3858-3864 (2003)

Scribing into hydrogenated diamond surfaces using atomic force microscopy
B. Rezek, C. Sauerer, J. A. Garrido, C. E. Nebel, M. Stutzmann, E. Snidero, and P. Bergonzo
Appl. Phys. Lett. **82**, 3336-3338 (2003)

Fermi level on hydrogen terminated diamond surfaces
B. Rezek, C. Sauerer, C. E. Nebel, M. Stutzmann, J. Ristein, L. Ley, E. Sindero, and P. Bergonzo
Appl. Phys. Lett. **82**, 2266-2268 (2003)

A new concept for tunable long wavelength VCSELs
F. Riemenschneider, I. Sagnes, G. Böhm, H. Halbritter, M. Maute, C. Symonds, M.-C. Amann, and P. Meissner
Optics Com. **222**, 341-350 (2003)

Micro-electro-mechanically tunable two-chip vertical cavity surface emitting laser for long wavelengths
F. Riemenschneider, I. Sagnes, G. Böhm, H. Halbritter, M. Maute, C. Symonds, M.-C. Amann, and P. Meissner
in: 53rd Electronics Components and Technology Conference (ECTC), New Orleans, USA (May 2003)

Micro-electro-mechanically tunable two-chip vertical cavity surfaceemitting laser for long wavelengths
F. Riemenschneider, I. Sagnes, G. Böhm, H. Halbritter, M. Maute, C. Symonds, M.-C. Amann, and P. Meissner
in: European Conference on Lasers and Electro-Optics (CLEO), Munich, Germany (June 2003)

Lateral index-guiding in InP-based laser diodes by oxidized AlAsSb layers
G. Rösel, R. Todt, M. Grau, and M.-C. Amann
in: Proc. of 27th WOCSDICE 2003, Fürigen, Switzerland (2003), p. 69-70

Optimization of type-II heterostructures for the tuning region in tunable laser diodes
G. Rösel, F. Köhler, R. Meyer, and M.-C. Amann
Semicond. Sci. Technol. **18**, 325-329 (2003)

Combined atomic force microscope and electron-beam lithography used for the fabrication of variable-coupling quantum dots
M. C. Rogge, C. Fühner, U. F. Keyser, R. J. Haug, M. Bichler, G. Abstreiter, and W. Wegscheider
Appl. Phys. Lett. **83**, 1163-1165 (2003)

Theory of vertical and lateral Stark shifts of excitons in quantum dots
M. Sabathil, S. Hackenbuchner, S. Birner, J. A. Majewski, P. Vogl, and J. J. Finley
phys. stat. sol. **0,** 1181-1184 (2003)

Efficient computational method for ballistic currents and application to single quantum dots
M. Sabathil, S. Birner, D. Mamaluy, and P. Vogl
J. Comput. Electronics **2**, 269 (2003)

Low-loss GaInAs-based waveguides for high-performance 5.5 mu m InP-based quantum cascade lasers
G. Scarpa, N. Ulbrich, G. Böhm, G. Abstreiter, and M.-C. Amann
IEEE Proceedings-Optoelectronics **150** (2003), p. 284-287

A novel approach for improved heat management in InP-based quantum cascade lasers
G. Scarpa, J. Freyer, A. Wieczorek, and M.-C. Amann
in: Proc. of 14th Indium Phosphide and Related Materials Conference, Stockholm, Sweden, (2003), p. 554-557

Non-equilibrium electronic distribution within one period of InP-based quantum cascade lasers
G. Scarpa, N. Ulbrich, G. Abstreiter, M.-C. Amann, M. Manenti, F. Compagnone, A. Di Carlo, and P. Lugli
in: Proc. of 13th International Conference on Nonequilibrium Carrier Dynamcis in Semiconductors, Modena, Italy (28.7.-1.8.2003)

Magnetization of a two-dimensional electron gas with a second filled subband
M. R. Schaapman, U. Zeitler, P. C. M. Christianen, J. C. Maan, D. Reuter, A. D. Wieck, D. Schuh, and M. Bichler
Phys. Rev. B **68,** 193308 (2003)

Field-effect-induced midinfrared electroluminescence of a quantum-wire-cascade structure by remote δ-doping
S. Schmult, I. Keck, T. Herrle, Werner Wegscheider, M. Bichler, D. Schuh, and G. Abstreiter
Appl. Phys. Lett. **83**, 1909-1911 (2003)

Spin-sensitive bleaching and spin relaxation in QWs
P. Schneider, S. D. Ganichev, J. Kainz, U. Rossler, W. Wegscheider, D. Weiss, W. Prettl, V. V. Bel`kov, L. E. Golub, and D. Schuh
phys. stat. sol. (b) **238**, 533-536 (2003)

Quantitative measurement of the influence of growth interruptions on the Sb distribution of GaSb/GaAs quantum wells by transmission electron microscopy
M. Schowalter, A. Rosenauer, D. Gerthsen, M. Grau and M.-C. Amann
Appl. Phys. Lett. **83**, 3123-3125 (2003)

Optical probing of a fractionally charged quasihole in an incompressible liquid
C. Schuller, K. B. Broocks, P. Schroter, C. Heyn, D. Heitmann, M. Bichler, W. Wegscheider, T. Chakraborty, and V. M. Apalkov
Phys. Rev. Lett. **91**, 116403 (2003)

Two-photon magnetoabsorption of the 2P excitons in GaN
Ch. Schweitzer, D. Fröhlich, K. Reimann, O. Ambacher, and M. Stutzmann
in: Proc. of the 26th Int. Conf. on the Physics of Semiconductors, Edinburgh 2002, ed. by A. R. Long and J. H. Davies, Bristol: IOP (2003), p. C4.4-1-7

Linewidth of InP-based 1.55µm VCSELs with buried tunnel junction
R. Shau, H. Halbritter, F. Riemenschneider, M. Ortsiefer, J. Rosskopf, G. Böhm, M. Maute, P. Meissner, and M.-C. Amann
Electron. Lett. **39**, 1728-1729 (2003)

Fabrication of InAlAs/InGaAs hetero-junction bipolar transistors using a self-aligned process
R. Singh, J. Freyer, G. Böhm, and M. Krach
in: Proc. of 27th WOCSDICE 2003, Fürigen, Switzerland (2003), p. 97-98

Exciton quenching in Pt/GaN Schottky diodes with Ga- and N-face polarity
S. Shokovets, D. Fuhrmann, R. Goldhahn, G. Gobsch, O. Ambacher, M. Hermann, U. Karrer, and M. Eickhoff
Appl. Phys. Lett. **82**, 1712 (2003)

pH response of GaN surfaces and its application for pH-sensitive field-effect transistors
G. Steinhoff, M. Hermann, W. J. Schaff, L. F. Eastman, M. Stutzmann, and M. Eickhoff
Appl. Phys. Lett. **83**, 177-179 (2003)

$Al_xGa_{1-x}N$ – A new material system for biosensors
G. Steinhoff, O. Purrucker, M. Tanaka, M. Stutzmann, and M. Eickhoff
Adv. Funct. Mater. **13**, 841-846 (2003)

Strain analysis of a quantum-wire system produced by cleaved edge overgrowth using grazing incidence x-ray diffraction
M. Sztucki, T. U. Schulli, T. H. Metzger, V. Chamard, R. Schuster, and D. Schuh
Appl. Phys. Lett. **83**, 872-874 (2003)

Raman characterization of strain and composition in small-sized self-assembled Si/Ge dots
P. H. Tan, K. Brunner, D. Bougeard, and G. Abstreiter
Phys. Rev. B **68**, 125302 (2003)

Femtosecond buildup of screening and collective effects in photoexcited GaAs: How bare charges get dressed
F. Tauser, R. Huber, A. Brodschelm, M. Bichler, G. Abstreiter, and A. Leitenstorfer
in: Physics of Semiconductors 2002, Institute of Physics Conference Series **171**, eds.: A. R. Long and J. H. Davies, Institute of Physics Publishing, Bristol and Philadelphia (2003), p. 93-100

1.8 µm vertical-cavity surface-emitting laser absorption measurements of HCl, H_20 and CH_4
G. Totschnig, M. Lackner, R. Shau, M. Ortsiefer, J. Rosskopf, M.-C. Amann, and F. Winter
Meas. Sci. Technol **14**, 472-478 (2003)

Non-perturbative solution for Bloch electrons in constant magnetic fields
A. Trellakis
Phys. Rev. Letters **91**, 056405-1 (2003)

Midinfrared intraband electroluminescence from AllnAs quantum dots
N. Ulbrich, J. Bauer, G. Scarpa, R. Boy, D. Schuh, G. Abstreiter, S. Schmult, and W. Wegscheider
Appl. Phys. Lett. **83**, 1530-1532 (2003)

Kelvin probe spectroscopy of a two-dimensional electron gas below 300 mK
T. Vancura, S. Kicin, T. Ihn, K. Ensslin, M. Bichler, and W. Wegscheider
Appl. Phys. Lett. **83**, 2602-2604 (2003)

Mid-infrared electroluminescence from device with changeable electron-hole distance
Y. B. Vasilyev, V. A. Solov`ev, B. Y. Meltser, A. N. Semenov, S. V. Ivanov, P. S. Kop`ev, N. Ulbrich, G. Abstreiter, and M. C. Amann
Electr. Lett. **39**, 108-110 (2003)

Electrically tunable mid-infrared electroluminescence from graded cascade structures
Yu. B. Vasilyev, V. A. Solov`ev, B. Ya. Meltser, A. N. Semenov, S. V. Ivanov, P. S. Kop`ev, N. Ulbrich, G. Abstreiter, M.-C. Amann, S. Schmult, and W. Wegscheider
Appl. Phys. Lett. **83**, 3015-3017 (2003)

Kinetics of the topotactic formation of siloxene
G. Vogg, M. S. Brandt, and M. Stutzmann
Chem. Mater. **15**, 910-915 (2003)

Oxidation states of Si and Ge sheet polymers
G. Vogg, M. S. Brandt, and M. Stutzmann
in: N. Auner and J. Weis, Organosilicon Chemistry **V**, Weinheim: Wiley-VCH (2003), p. 789-796

Self-similar optical absorption spectra in high magnetic fields
P. Vogl and C. Strahberger
in: Physics of Semiconductors 2002, ed. by A. R. Long and J. H. Davies, Institute of Physics Publ., Bristol (2003), p. E1.3

Influence of surface oxides on hydrogen-sensitive Pd:GaN Schottky diodes
O. Weidemann, M. Hermann, G. Steinhoff, H. Wingbrandt, A. Lloyd-Spetz, M. Stutzmann, and M. Eickhoff
Appl. Phys. Lett. **83**, 773-775 (2003)

Photoreflectance studies of N- and Ga-face AlGaN/GaN heterostructures confining a polarisation induced 2DEG
A. T. Winzer, R. Goldhahn, C. Buchheim, O. Ambacher, A. Link, M. Stutzmann, Y. Smorchkova, U. K. Mishra, and J. S. Speck
phys. stat. sol. (b) **240**, 380-383 (2003)

Chaos and open orbits in hole-antidot arrays with non-isotropic Fermi surface
M. Zitzlsperger, R. Onderka, M. Suhrke, U. Rossler, D. Weiss, W. Wegscheider, M. Bichler, R. Winkler, Y. Hiryama, and K. Muraki
Europhys. Lett. **61**, 382-388 (2003)

7. Invited Talks

Gerhard Abstreiter

1. *Control of charge and spin in novel semiconductor nano-devices*
   Seminar, University Modena, Italy (28.1.2003)

2. *Semiconductor nanodevices*
   Forum Innovations from Eastern Europe (Bayern Innovativ)
   "Nanoanalytics – Nanoelectronics" Munich, Germany (22.5.2003)

3. 3 Lectures on *"Electronic excitations in semiconductors"*
   International School of Physics "Enrico Fermi" on "The Electron Liquid Model in Condensed Matter Physics", Varenna, Italy (31.7.2003 and 1.8.2003)

4. Lecture on *"Spins in reduced dimensions: primarily quantum dots"*
   Spintech II School on "Semiconductor Spintronics and Quantum Information Technology", Brügge, Belgium (8.8.2003)

5. *Control of charge and coherent excitations of single dot photodiodes*
   Third Stig Landgvist Conference on Advancing Frontiers of Condensed Matter Physics: "Fundamental Interactions and Excitations in Confined Systems", Trieste, Italy (14.8.2003)

6. *Few electrons in semiconductor nanostructures*
   Conference on "Electrical and Mechanical Properties of Nanowires", Venice, Italy (19.8.2003)

7. *Control of charge and spin in novel semiconductor nano-devices*
   Seminar, MPI für Quantenoptik, Garching, Germany (18.11.2003) and
   Seminar, Infineon Corporate Research, Munich, Germany (19.11.2003)

8. *From two-dimensional to one-and zero-dimensional electron systems*
   Fowler Symposium, IBM Research Center, Yorktown Heights, USA (10.11.2003)

9. *Single dot spectroscopy: basis for precise control of individual charges, spins, and photons*
   Conference on "Solid State Quantum Information Processing, Amsterdam, The Netherlands (18.12.2003)

Markus-Christian Amann

1. *Long-wavelength LP-based VCSELs*
   ECOC 2003, Rimini, Italy (21.-25.9.2003)

2. *InP-based VCSELs for 1,3-2 µm wavelength range*
   OSA Annual Meeting, Tucson, USA (05.-9.10.2003)

3. *Wavelength-tunable laser diodes for optical communications*
   16th Annual Meeting of the IEEE Lasers & Optics Society, Tucson, USA (26.-30.10.2003)

Evelin Beham

1. *Single quantum dot photodiode a two-level system with electric contacts*
   DPG-Frühjahrstagung Dresden, Germany (27.3.2003)

Martin S. Brandt

1. *Spinabhängiger Transport: Elektrischer Nachweis magnetischer Resonanz*
   Seminar, Universität Regensburg, Germany (23.1.2003)

2. *Herausforderungen neuerer Schichtsysteme*
   Seminar, Universität Kiel, Germany (8.7.2003)

Martin Eickhoff

1. *GaN based chemical sensors*
   Kolloquium am Zentrum für Mikro- und Nanotechnologien, Technische Universität Ilmenau, Germany (15.1.2003)

2. *Chemical sensing with GaN-based devices*
   Seminar, Universidad Polytechnica de Madrid, Instituto de Sistemas Optoelectronicos y Microtecnologia, Spain (8.5.2003)

3. *Why nitrides need oxides*
   12th European Workshop on Heterostructure Technology, San Rafael, Segovia, Spain (14.10.2003)

4. *GaN field effect chemical sensors*
   204th Annual Meeting of the Electrochemical Society, Orlando, Fl, USA (16.10.2003)

5. *GaN field effect devices for chemical sensing*
   Kolloquium zur Halbleitertechnologie und Messtechnik, Fraunhofer Institut für Integrierte Systeme und Bauelementtechnologie, Erlangen, Germany (24.11.2003)

Frank Ertl

1. *Resonant tunneling between parallel 1D quantum wires and adjoining 2D electron reservoirs*
   Seminar, Universität Regensburg, Germany (26.5.2003)

Jonathan Finley

1. *Probing many body wavefunctions in individual InGaAs quantum dots*
   MSS11 Conference, Nara, Japan (16.7. 2003)

José Antonio Garrido

1. *Novel devices on H-induced surface conductive diamond*
   Surface and Bulk Defects in CVD Diamond Films, VIII, Diepenbeek-Hasselt, Belgium (26.-28.2.2003)

2. *Surface electronics on H-terminated diamond*
   Seminar, Ruhr-Universität Bochum, Germany (26.6.2003)

3. *AlN&Diamond heterojunctions*
   Diamond 2003, Salzburg, Austria (7.-12.9.2003)

Sebastian Gönnenwein

1. *GaMnAs: magnons, magnetic resonance, and hydrogen in a ferromagnetic semiconductor*
   Seminar, Universität Ulm, Germany (20.5.2003)

Tobias Graf

1. *Elektronspinresonanz in ZnO:Mn*
   Seminar, Walther-Meissner-Institut, Garching, Germany (15.4.2003)

2. *Electrically detected magnetic resonance and its application to diamond*
   54th DeBeers Diamond Conference, Cambridge, England (7.-9.7.2003)

3. *Mn^{2+} and Mn^{3+} gap states in GaN and AlN*
   International Conference on Defects in Semiconductors, Aarhus, Denmark (28.7.-1.8.2003)

4. *Electron spin resonance of phosphorus in n-type diamond*
   Diamond 2003, Salzburg, Austria (7.-12.9.2003)

Markus Grau

1. *GaSb-basierte Typ-I-Laserdioden für den Wellenlängenbereich ab 2 µm*
   Seminar, Fraunhofer Institut für Angewandte Festkörperphysik, Freiburg, Germany (17.9.2003)

Matthew Grayson

1. *Introducing the bent quantum well*
   Seminar, Forschungszentrum Karlsruhe (FZK), Karlsruhe, Germany (30.4.2003)

2. *Novel crystal growth methods for quantum Hall effect devices: (110) GaAs*
   Seminar, Institute of Industrial Science, University of Tokyo, Japan (22.7.2003)

3. Lecture on *"Electronic correlations at the edge of a quantum Hall liquid"*
   International School of Physics "Enrico Fermi" on "The Electron Liquid Model in Condensed Matter Physics", Varenna, Italy (7.8.2003)

4. *Quantum Hall edges as one-dimensional systems*
   Conference on "Electrical and Mechanical Properties of Nanowires", Venice, Italy (17.8.2003)

5. *Momentum resolved tunnel spectroscopy of quantum Hall effect edges*
   Seminar, Columbia University, New York, USA (23.9.2003)

6. *Momentum resolved tunnel spectroscopy of quantum Hall effect edges*
   Seminar, City College of New York, New York, USA (24.9.2003)

7. *Corner quantum wells: quantum Hall physics in a two-dimensional electron system bent by 90 degrees*
   Seminar, University of Maryland, College Park, Maryland, USA (25.9.2003)

8. *Corner quantum wells: quantum Hall physics in a two-dimensional electron system bent by 90 degrees*
   Seminar, Princeton University, Princeton, New Jersey, USA (29.09.2003)

9. *Momentum resolved tunnel spectroscopy of quantum Hall effect edges*
   Seminar, Massachusetts Institute of Technology, Boston, Massachusetts, USA (30.9.2003)

10. *Momentum resolved tunnel spectroscopy of quantum Hall effect edges*
    Seminar, Yale University, New Haven, Connecticut, USA (1.10.2003)

11. *Momentum resolved tunnel spectroscopy of quantum Hall effect edges*
    Seminar, Harvard University, Cambridge, Massachusetts, USA (2.10.2003)

12. *Corner quantum wells: quantum Hall physics in a two-dimensional electron system bent by 90 degrees*
Seminar, Boston University, Boston, Massachusetts, USA (3.10.2003)

Jacek A. Majewski

1. *Spin decoherence in semiconductor heterostructures*
Seminar, Warsaw University, Poland (28.3.2003)

2. *Concepts and realizations of nitride heterostructure devices: pyroelectronics*
Seminar, Center of High Pressure Research, UNIPRESS, Warsaw, Poland (9.4.2003)

3. *Ab-initio methods in materials science: applications and new developments*
Kolloquium, Leopold Infeld Colloqium, Warsaw University, Poland (22.5.2003)

4. *Spin decoherence in semiconductor heterostructures*
Seminar, Universität Göttingen, Germany (19.6.2003)

Dieter Schuh

1. *Molecular beam epitaxy on (110)-oriented GaAs surfaces*
Seminar, Universität Duisburg, Germany (15.1.2003)

2. *Molecular beam epitaxy on (110)-oriented GaAs surfaces: growth and novel devices*
Seminar, MPI Stuttgart, held in Ringberg, Germany (13.10.2003)

Martin Stutzmann

1. *a-Si:H as a bio-substrate: recent results*
2nd aSiNet Workshop, Lisbon, Portugal (19.2.2003)

2. *Structural and electronic properties of diamond/AlGaN heterostructures*
Surface and Bulk Defects in CVD Diamond Films, VIII, Diepenbeek-Hasselt, Belgium (26.2.2003)

3. *GaN:Mn – Prospects for a ferromagnetic semiconductor?*
Seminar, K.U. Leuven, Belgium (28.2.2003)

4. *The role of oxides for III-nitride sensors*
DPG Frühjahrstagung Dresden, Germany (27.3.2003)

5. *Novel heterostructures based on III-nitrides*
MRS Spring Meeting, San Francisco, USA (23.4.2003)

6. *Biosensorik mit Gruppe III-Nitriden*
Physikalisches Kolloquium, Otto-von-Guericke-Universität Magdeburg, Germany (13.5.2003)

7. *Nitridische Halbleiter für die Sensorik*
WE-Heraeus-Ferienkurs für Physik, Magdeburg, Germany (15.9.2003)

8. *Two-dimensional charge carrier systems for chemical sensors: GaN/AlGaN and diamond*
IEEE Sensors 2003, Toronto, Canada (24.10.2003)

9. *Moderne Halbleiterphysik*
Lüscher Lectures, Akademie für Lehrerfortbildung und Personalbildung, Dillingen, Germany (29.10.2003)

Marc Tornow

1. *Controlled release of immobilized DNA into electrolyte solution*
Internal Workshop of the Center of Nanoscience (CeNS), Kloster Seeon, Germany (28.-30.9.2003)

2. *Sensing and manipulating (bio-)molecular coatings on functional substrates*
Seminar of the Department of Materials and Interfaces, Weizmann Institut of Science Rehovot, Israel (31.12.2003)

Peter Vogl

1. *The physics of SiGe devices: How to make a mess work,* American Physical Society March Meeting, Austin, USA (1.-7.3.2003)

2. *nextnano3 - a state-of-the-art simulation tool for 3D quantum devices,* Workshop "Growth, electronic and optical properties of low-dimensional semiconductor quantum structures", Schloss Ringberg, Tegernsee bei München, Germany (12.-15.2.2003)

3. *Magnetische Effekte ohne Magnetfelder - Spintronik in Halbleitern,* Kolloquium, Universität Oldenburg, Germany (28.4.2003)

9. Selected Topics of Semiconductor Physics and Technology

Since1997, all doctoral theses are published in the series: Selected Topics of Semiconductor Physics and Technology, eds.: G. Abstreiter, M.-C. Amann, M. Stutzmann, and P. Vogl. The following volumes appeared so far in this series:

Vol. 1
Cornelia Engel
Si/SiGe basierende Phototransistoren
131 Seiten
ISBN 3-932749-01-4

Vol. 2
Peter Schittenhelm
Selbst-Organisation und Selbst-Ordnung in Si/SiGe-Heterostrukturen
151 Seiten
ISBN 3-932749-02-2

Vol. 3
Andreas Nutsch
Selektive Epitaxie von (GaIn)(AsP) Schichtstrukturen
129 Seiten
ISBN 3-932749-03-0

Vol. 4
Peter Baumgartner
Optische und elektronische Eigenschaften lasergeschriebener GaAs-Nanostrukturen
180 Seiten
ISBN 3-932749-04-9

Vol. 5
Walter Franz Rieger
Untersuchung der elektronischen und strukturellen Eigenschaften von GaNAlN und deren Legierungen
158 Seiten
ISBN 3-932749-05-7

Vol. 6
Markus Hauser
Oberflächenemittierende Laserdioden mit Mehrfachepitaxie
148 Seiten
ISBN 3-932749-06-5

Vol. 7
Markus Sexl
Verspannte und gitterrelaxierte In(GaAl)As Heterostrukturen
144 Seiten
ISBN 3-932749-07-3

Vol. 8
Christian Obermüller
Photolumineszenszspektroskopie mit optischen Nahfeldmethoden an GaAs-Nanostrukturen
140 Seiten
ISBN 3-932749-08-1

Vol. 9
Edilson Silveira
Inelastische Lichtstreuung an niedrig-dimensionalen Halbleiterstrukturen
104 Seiten
ISBN 3-932749-09-X

Vol. 10
Eberhard Christian Rohrer
Photoleitungs-Spektroskopie von Diamant
153 Seiten
ISBN 3-932749-10-03

Vol. 11
Thomas Wimbauer
Magnetische Resonanz-Untersuchungen an modernen Halbleitermaterialien
125 Seiten
ISBN 3-932749-11-1

Vol. 12
Herbert Verhoeven
Thermische Eigenschaften von CVD-Diamantschichten
154 Seiten
ISBN 3-932749-12-X

Vol. 13
Hans-Christoph Ostendorf
Trennung von Volumen- und Oberflächenrekombination in Silizium
128 Seiten
ISBN 3-932749-13-8

Vol. 14
Martin Städele
Dichtefunktionaltheorie mit exaktem Austausch für Halbleiter
202 Seiten
ISBN 3-932749-14-6

Vol. 15
Helmut Angerer
Herstellung von Gruppe III-Nitriden mit Molekularstrahlepitaxie
144 Seiten
ISBN 3-932749-15-4

Vol. 16
Wolfgang Heller
Spektroskopie einzelner Quantenpunkte in magnetischen und elektrischen Feldern
128 Seiten
ISBN 3-932749-16-2

Vol. 17
Molela Moukara
Pseudopotentiale mit exaktem Austausch
117 Seiten
ISBN 3-932749-17-0

Vol. 18
Ralph Oberhuber
Elektronische Struktur und Transport in verspannten Halbleiterschichtsystemen
110 Seiten
ISBN 3-932749-18-9

Vol. 19
Reiner Pech
High-Energy Boron-Implantation into Different Silicon Substrates
158 Seiten
ISBN 3-932749-19-7

Vol. 20
Christoph Martin Engelhardt
Zyklotronresonanz zweidimensionaler Ladungsträgersysteme in Halbleitern, Effekte der Elektron-Elektron-Wechselwirkung und Lokalisierung
317 Seiten
ISBN 3-932749-20-0

Vol. 21
Eduard Neufeld
Erbium-dotierte Si/SiGe-Lichtemitter und -Wellenleiter
136 Seiten
ISBN 3-932749-21-9

Vol. 22
Gert Schedelbeck
Optische Eigenschaften von Halbleiternanostrukturen hergestellt durch Überwachsen von Spaltflächen
154 Seiten
ISBN 3-932749-22-7

Vol. 23
Jürgen Zimmer
Optoelektronisches Verhalten von Dünnschichtbauelementen aus amorphem und mikrokristallinem Silizium
171 Seiten
ISBN 3-932749-23-5

Vol. 24
Berthold Schmidt
Leistungsoptimierung abstimmbarer InGaAsP/InP Halbleiterlaser
85 Seiten
ISBN 3-932749-24-3

Vol. 25
Jianhong Zhu
Ordering of self-assembled Ge and SiGe nanostructures on vicinal Si surfaces
120 Seiten
ISBN 3-932749-25-1

Vol. 26
Gerhard Groos
Herstellung und Charakterisierung von Silizium-Nanostrukturen
168 Seiten
ISBN 3-932749-26-X

Vol. 27
Uwe Hansen
Theorie der Reaktionskinetik an Festkörperoberflächen
119 Seiten
ISBN 3-932749-27-8

Vol. 28
Roman Dimitrov
Herstellung und Charakterisierung von AlGaN/GaN-Transistoren
196 Seiten
ISBN 3-932749-28-6

Vol. 29
Martin Eickhoff
Piezowiderstandsmechanismen in Halbleitern mit großer Bandlücke
151 Seiten
ISBN 3-932749-29-4

Vol. 30
Nikolai Wieser
Ramanspektroskopie an Gruppe III-Nitriden
161 Seiten
ISBN 3-932749-30-8

Vol. 31
Rainer Janssen
Strukturelle und elektronische Eigenschaften amorpher Silizium-Suboxide
275 Seiten
ISBN 3-932749-31-6

Vol. 32
Martin W. Bayerl
Magnetic resonance investigations of group III-nitrides
155 Seiten
ISBN 3-932749-32-4

Vol. 33
Martin Rother
Elektronische Eigenschaften von Halbleiternanostrukturen hergestellt durch Überwachsen von Spaltflächen
196 Seiten
ISBN 3-932749-33-2

Vol. 34
Frank Findeis
Optical spectroscopy on single self-assembled quantum dots
156 Seiten
ISBN 3-932749-34-0

Vol. 35
Markus Ortsiefer
Langwellige Vertikalresonator-Laser-dioden im Materialsystem InGaAlAs/InP
152 Seiten
ISBN 3-932749-35-9

Vol. 36
Roland Zeisel
Optoelectronic properties of defects in diamond and AlGaN alloys
140 Seiten
ISBN 3-932749-36-7

Vol. 37
Liwen Chu
Inter- und Intraband Spektroskopie an selbstorganisierten In(Ga)As/GaAs Quantenpunkten
124 Seiten
ISBN 3-932749-37-5

Vol. 38
Christian Alexander Miesner
Intra-Valenzbandspektroskopie an SiGe-Nanostrukturen in Si
100 Seiten
ISBN 3-932749-38-3

Vol. 39
Szabolcs Kátai
Investigation of the nucleation process of chemical vapour deposited diamond films
178 Seiten
ISBN 3-932749-39-1

Vol. 40
Markus Arzberger
Wachstum, Eigenschaften und Anwendungen selbstorganisierter InAs-Quantenpunkte
236 Seiten
ISBN 3-932749-40-5

Vol. 41
Markus Oliver Markmann
Optische Eigenschaften von Erbium in $Si/Si_{1-x}C_x$, $Si/Si_{1-x}Ge_x$ und Si/SiO_x Heterostrukturen
182 Seiten
ISBN 3-932749-41-3

Vol. 42
Rainer Alexander Deutschmann
Two dimensional electron systems in atomically precise periodic potential
210 Seiten
ISBN 3-932749-42-1

Vol. 43
Uwe Karrer
Schottky-Dioden auf Galliumnitrid: Eigenschaften und Anwendungen in der Sensorik
182 Seiten
ISBN 3-932749-43-X

Vol. 44
Günther Anton Johann Vogg
Epitaxial thin films of Si and Ge based Zintl phases and sheet polymers
169 Seiten
ISBN 3-932749-44-8

Vol. 45
Christian Strahberger
Vertikaler Transport und extreme Magnetfelder in Halbleitern
167 Seiten
ISBN 3-932749-45-6

Vol. 46
Jan Schalwig
Feldeffekt-Gassensoren und ihre Anwendung in Abgas-nachbehandlungssystemen
125 Seiten
ISBN 3-932749-46-4

Vol. 47
Christopher Eisele
Novel absorber structures for Si-based thin film solar cells
126 Seiten
ISBN 3-932749-47-2

Vol. 48
Stefan Hackenbuchner
Elektronische Struktur von Halbleiter-Nanobauelementen im thermodynamischen Nichtgleichgewicht
213 Seiten
ISBN 3-932749-48-0

Vol. 49
Andreas Sticht
Herstellung und Charakterisierung von dünnen Silizium/Siliziumoxid-Schichtsystemen
166 Seiten
ISBN 3-932749-49-9

Vol. 50
Giuseppe Scarpa
Design and fabrication of Quantum Cascade Lasers
193 Seiten
ISBN 3-932749-50-2

Vol. 51
Jörg Frankenberger
Optische Untersuchungen an zweidimensionalen Ladungsträgersystemen
158 Seiten
ISBN 3-932749-51-0

Vol. 52
Doris Heinrich
Wavelength selective optically induced charge storage in self-assembled semiconductor quantum dots
144 Seiten
ISBN 3-932749-52-9

Vol. 53
Nicolaus Ulbrich
Entwurf und Charakterisierung von Quanten-Kaskadenlasern und Quantenpunktkaskaden
133 Seiten
ISBN 3-932749-53-7

Vol. 54
Lutz Carsten Görgens
Analyse stickstoffhaltiger III-V Halbleiter-Heterosysteme mit hochenergetischen schweren Ionen
116 Seiten
ISBN 3-932749-54-5

Vol. 55
Andreas Janotta
Doping, light-induced modification and biocompatibility of amorphous silicon suboxides
180 Seiten
ISBN 3-932749-55-3

Vol. 56
Sebastian Tobias Benedikt Gönnenwein
Two-dimensional electron gases and ferromagnetic semiconductors: materials for spintronics
198 Seiten
ISBN 3-932749-56-1

Vol. 57
Evelin Beham
Photostromspektroskopie an einzelnen Quantenpunkten
186 Seiten
ISBN 3-932749-57-X

Vol. 58
Po-Wen Chiu
Towards carbon nanotube-based molecular electronics
116 Seiten
ISBN 3-932749-58-8

Vol. 59
Tobias Graf
Spin-spin interactions of localized electronic states in semiconductors
194 Seiten
ISBN 3-932749-59-6

Vol. 60
Stefan Klein
Microcrystalline silicon prepared by hot wire CVD: preparation and characterisation of material and solar cells
157 Seiten
ISBN 3-932749-60-X